Research Studies:

M_w 6.0 South Napa Earthquake of August 24, 2014

2 New Streams and Springs After the 2014 M6.0 Napa Earthquake

Chi-Yuen Wang and Michael Manga

Introduction

At least nine streams and several springs, which were dry or had little flow before the 2014 M6.0 South Napa earthquake, started to flow after the earthquake. At the same time, a USGS stream gauge on Sonoma Creek registered a coseismic increase in discharge. Public interest in the increased flow was heightened by a state of extreme drought in California.

It has been known for millennia that earthquakes can induce a variety of hydrological responses. Several hypotheses have been proposed to explain increased discharge, including that responses are caused by poroelastic deformation, changes in permeability, the release of deep hydrothermal fluids, or that water is released from soils. Such streamflow increases are more than curiosities because understanding their origin can provide unique insight into the interactions between hydrogeologic and tectonic processes at spatial and temporal scales that are otherwise difficult to study. In addition, such understanding may have implications for underground waste repositories, hydrocarbon production, water supplies, and subsurface transport of heat and solutes.

Following the earthquake we repeatedly surveyed the new flows, collected water samples and carried out laboratory measurements. In Wang and Manga (2015) we report the results of the survey, the origin of the new water, and the amount of water released by the earthquake.

Data

For this study we monitored seven new streams and one spring free of human interference such as dams upstream, and three major perennial streams in the foothills (Figure 2.2.1). We measured discharge (Figure 2.2.2) and water temperature, and collected water samples for stable isotope and geochemical analysis.

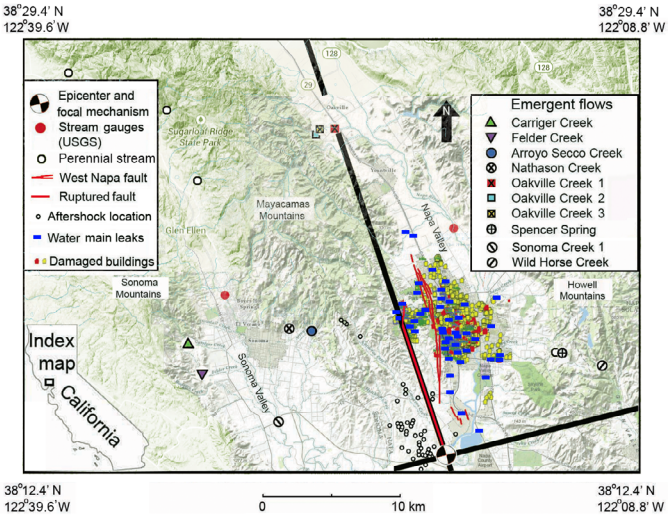

Figure 2.2.1 Locations of sampling sites of new streams and springs, the USGS gauges, and the Napa earthquake.

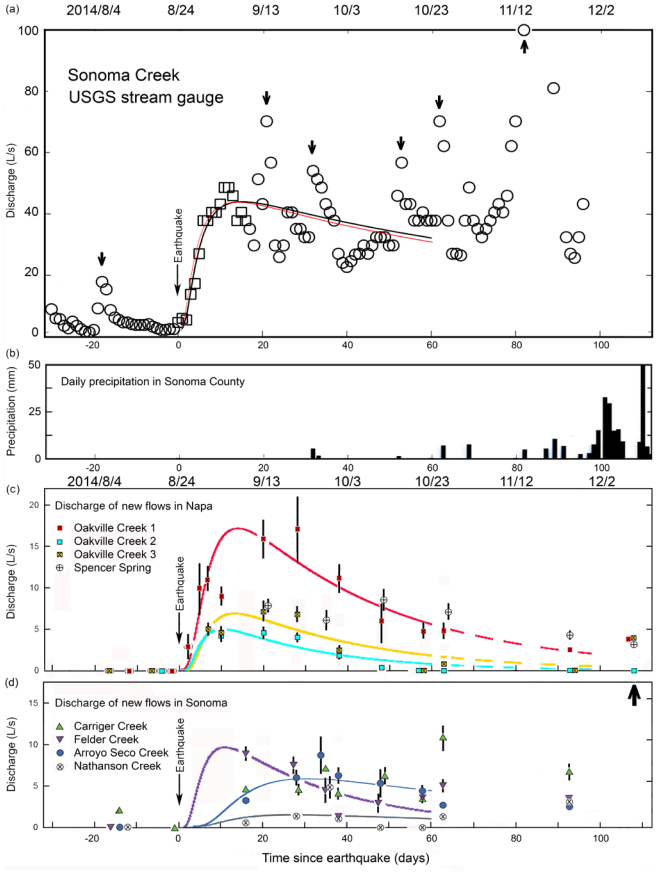

Figure 2.2.2 a) Sonoma Creek data and best fit groundwater flow model, see Wang and Manga (2015) for details about the model. b) Precipitation data. Discharge and best fit models for studied new streams in c) Napa and d) Sonoma

In addition, a USGS stream gauge on Sonoma Creek recorded a coseismic increase of discharge, showing increased groundwater flow throughout the basin after the earthquake.

Results

The combination of the earthquake and drought assured that most new flows were not mixed with pre-existing surface waters and thus allowed unambiguous determination of their composition. We found that the new flows were meteoric in origin and likely groundwater in nearby mountains released by the earthquake.

If the new flows were caused by static poroelastic strain, no new flows would have appeared in the dilatational quadrants. However, Spencer Spring is located in a dilatational quadrant, and the Oakville Creeks are all located near the boundary between dilatational and compressional regimes (Figure 2.2.1) where the volumetric strain is nearly zero. Thus the prediction of the hypothesis of static poroelastic strain is not consistent with observations. Instead, increased discharge is induced by dynamic stresses.

Stable isotope measurements show that the water did not originate from soils (Figure 2.2.3), and geochemical measurements show that the new water is not from hydrothermal systems. The water thus originates from groundwater and the location and the composition of the new flows require that the water originated from the mountains adjacent to Napa and Sonoma Valleys. Taken together, these observations can be explained by increases in permeability produced by the passage of seismic waves.

We also simulated the flows by solving the groundwater flow equations (Figure 2.2.2) and estimate the total amount of new water to be ~106 m^3, about 1/40 of the annual water use in the Napa-Sonoma area. Since drainage of groundwater from pores and fractures would make the shallow crust more compressible, our model predicts a post-seismic decrease of seismic velocity in the shallow crust, as documented by Taira (2014).

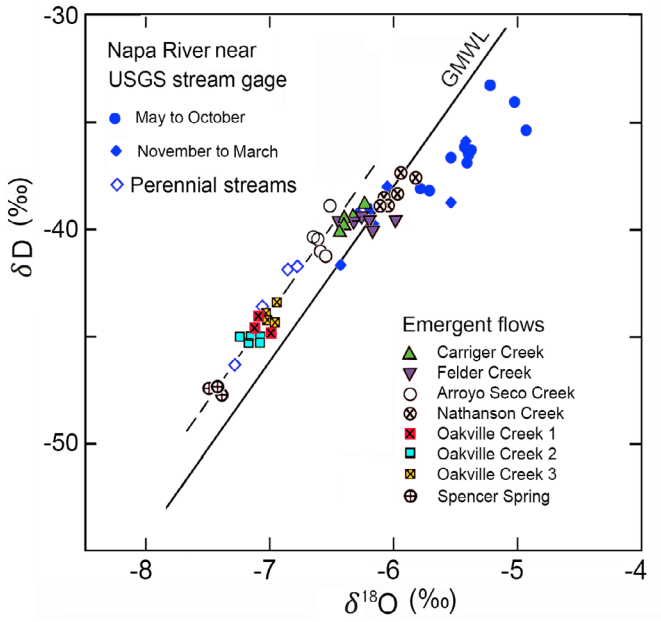

Figure 2.2.3 Stable isotope data for studied new streams and springs along with the global meteoric water line (GMWL) and other regional waters.

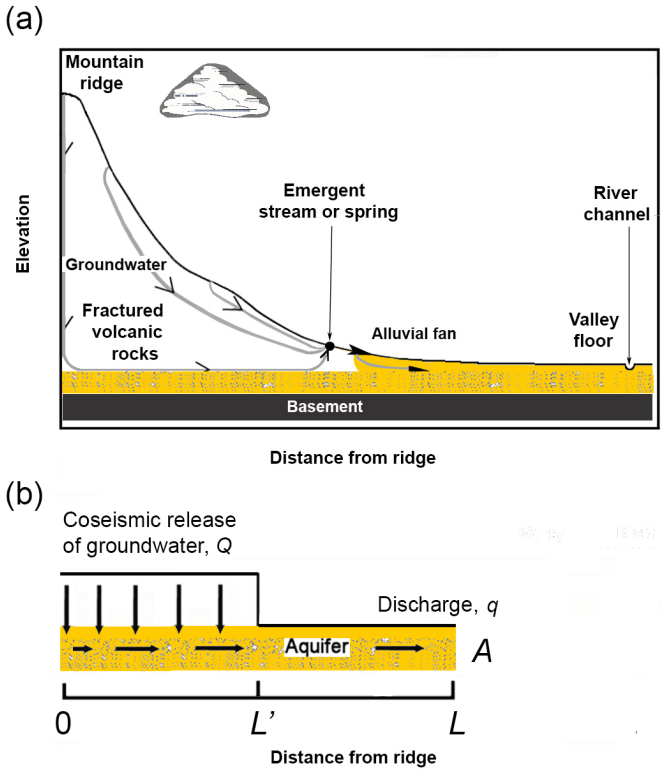

Figure 2.2.4 a) Conceptual model and b) geometry of the model applied to the data.

Acknowledgements

This work was supported by NSF grant EAR1463997.

References

Wang, C.-Y., and M. Manga, 2015, New streams and springs after the M6 South Napa earthquake, Nature Communications 6:7597 doi: 10.1038/ncomms8597

Taira, T., 2014, Monitoring seismic velocity changes associated with the 2014 Mw6.0 South Napa earthquake, Abstract, 2014 Fall Annual Meeting, American Geophysical Union, S33F-4921.

2 Three-Dimensional Finite Difference Simulation of Ground Motions from the August 24, 2014 South Napa Earthquake

Arthur Rodgers(LLNL and BSL), Douglas S. Dreger (BSL) and Arben Pitarka (LLNL)

Introduction

The M_w6.0 August 24, 2014 South Napa earthquake is the largest seismic event in the San Francisco Bay Area since the 1989 M_W6.9 Loma Prieta earthquake (*Brocher et al.*, 2015). This recent event was recorded by more numerous and modern instruments, including sensors operated and archived by the Northern California Earthquake Data Center operated by BSL.

We performed three-dimensional (3D) anelastic ground motion simulations of the South Napa earthquake to investigate the performance of different finite rupture models and the effects of 3D structure on the observed wavefield. We considered rupture models reported by *Dreger et al.* (2015), *Ji et al.*, (2015), *Wei et al.* (2015) and *Melgar et al.* (2015). We used the SW4 anelastic finite difference code developed at Lawrence Livermore National Laboratory (*Petersson and Sjogreen*, 2013) and distributed by the Computational Infrastructure for Geodynamics. This code can compute the seismic response for fully 3D sub-surface models, including surface topography and linear anelasticity. We use the 3D geologic/seismic model of the San Francisco Bay Area developed by the United States Geological Survey (*Aagaard et al.*, 2008, 2010). Evaluation of earlier versions of this model indicated that the structure can reproduce the main features of observed waveforms from moderate earthquakes (*Rodgers et al.*, 2008; *Kim et al.*, 2010). Simulations were performed for a domain covering local distances (< 25 km) and resolution providing simulated ground motions valid to 1 Hz.

Simulation Results and Waveform Comparisons

The waveforms for the South Napa earthquake show significant variability due to rupture details, path and site effects. We started by computing the response at local distance seismic stations (strong motion and broadband) for the rupture model developed by *Dreger et al.* (2015). This model shows that the rupture propagated from the hypocenter (11 km depth) up dip and to the north. Consequently directivity to the north sent seismic energy into the sedimentary structure underlying the Napa Valley.

We have compared waveforms for four reported finite rupture models and synthetics based on the 1D and 3D models. We generally find that 3D effects on the waveforms are significant, especially for sites in sedimentary basins or whose paths interact with basins or other material heterogeneity. Figure 2.2.1 shows a snapshot of the ground velocity as the rupture evolves (color coded with the ShakeMap scheme). Also shown are comparisons of the observed and synthetic waveforms at the two stations (NC.N016 in Napa Valley and NC.NSP across the Sonoma Valley). Synthetics were computed for the 1D (GIL7, *Stidham et al.*, 1999) and 3D models. Note that the 3D model clearly fits the amplitudes and late arriving scattered surface waves.

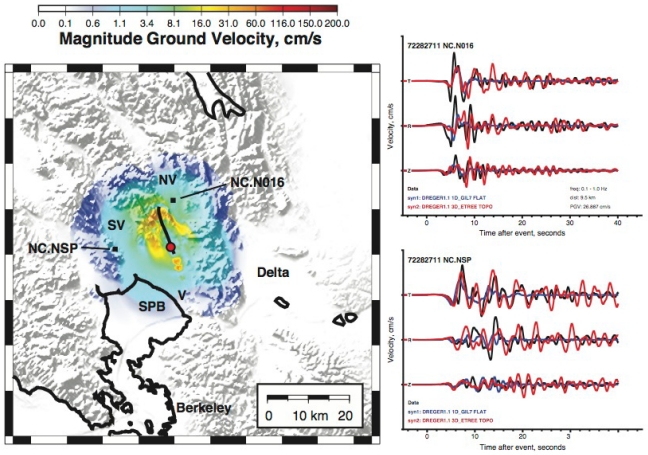

Figure 2.2.1: Left) Snapshot of the ground motion from the South Napa earthquake, with the magnitude of ground velocity (cm s^{-1}, scaled with color scale). The event initiated at the epicenter (red circle) and ruptured along the fault (thick black line). Squares mark the locations of two seismic stations from which the waveforms on the right is showing. Place names are Napa Valley (NV), Sonoma Valley (SV), Vallejo (V), and San Pablo Bay (SPB). Right) Three-component seismograms for the event contrast the observed (black) ground motions with those computed with a 3D model and topography (red) and for a 1D model (blue).

Response Spectra

In order to evaluate the ground motion parameters of interest for engineering seismology, we computed the RotD50 spectral responses of the data and synthetics. We then formed the natural logarithmic ratio of data/synthetic as a function of period. This ratio measures the bias such that for values of 0, the synthetic predicts exactly the response spectrum at that period and positive/negative bias indicates that the data is larger/smaller than the data is at that period.

Figure 2.2.2 shows the response spectral bias for three of the rupture models considered for 1D (left) and 3D structural models (right), based on 24 local distance stations (< 25 km). The response spectra are generally biased high for the 1D model compared to the 3D model. This is most likely due to the relatively high near-surface wave speeds of the 1D model (1500 ms^{-1}) compared to the lower wave speeds of the 3D models (~ 400 ms^{-1}). Note that the scatter in the response spectral bias is lower for the 3D model, suggesting that 3D wave propagation effects are properly accounted for in the USGS 3D model.

Conclusions and Recommendations

This study indicates that 3D seismic simulations on high-performance computers using the reported rupture models and the USGS 3D geologic/seismic model of the San Francisco Bay Area can accurately model observed ground motions.

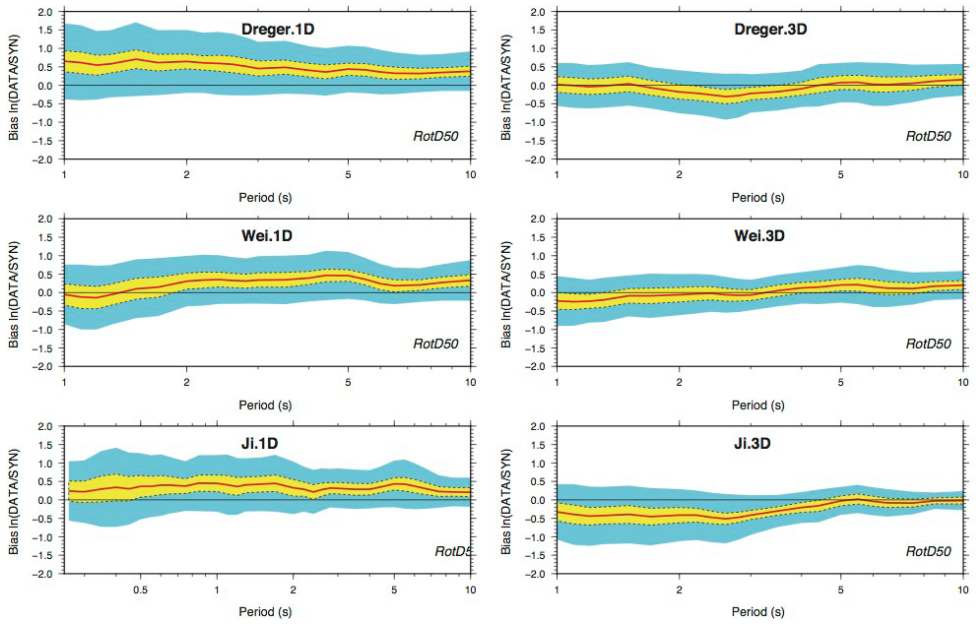

Figure 2.2.2: Rotd50 bias (logarithm of data/synthetic) for three rupture models for 1D (left) and 3D (right) structural models. The average (red line) and spread are based on 24 local distance stations.

Clearly the model can be improved and simulations performed at higher frequency. Model improvements could be obtained by waveform-based adjoint tomography using moderate earthquakes that have already been recorded. Advances in computing and access to more powerful computers will enable higher frequency simulations.

Acknowledgements

Funding for this effort was provided by the LLNL, Laboratory Directed Research and Development Office under project ER-14-001. Simulations were performed on the Cab Linux cluster operated by Livermore Computing. Waveform data were obtained from the Northern California Earthquake Data Center (NCEDC). This work was performed under the auspices of the U.S. Department of Energy by LLNL under contract DE-AC52-07NA27344. This is LLNL contribution LLNL-TR-673182.

References

Aagaard, B. T., R. W. Graves, A. J. Rodgers, T. M. Brocher, R. W. Simpson, D. Dreger, N. A. Petersson, S. C. Larsen, S. Ma and R. C. Jachens (2010), Ground-Motion Modeling of Hayward Fault Scenario Earthquakes, Part II: Simulation of Long-Period and Broadband Ground Motions, *Bull. Seismol. Soc. Am.*, 100, 2945-2977, doi: 10.1785/0120090379.

Aagaard, B. T., T. M. Brocher, D. Dolenc, D. Dreger, R. W. Graves, S. Harmsen, S. Hartzell, S. C. Larsen, K. McCandless, S. Nilsson, N. A. Petersson, A. J. Rodgers, B. Sjogreen, M. L. Zoback (2008), Ground-motion modeling of the 1906 San Francisco earthquake, part II: Ground-motion estimates for the 1906 earthquake and scenario events, *Bull. Seismol. Soc. Am.*, 98, 1012-1046, doi: 10.1785/0120060410.

Brocher, T. and 22 other (2015), The MW 6.0 24 August 2014 South Napa earthquake, *Seismo. Res. Lett.*, 86, 309-326, doi: 10.1785/0220150004.

Dreger, D. S., H.-H. Huang, A. Rodgers, T. Taira and K. Wooddell (2015), Kinematic Finite-Source Model for the August 24, 2014 South Napa, CA Earthquake from Joint Inversion of Seismic, GPS and InSAR Data, *Seismo. Res. Lett.*, 86, doi: 10.1785/0220140244.

Ji, C., R. Archuleta and C. Twardzik (2015), Rupture history of 2014 MW 6.0 South Napa earthquake inferred from near fault strong motion data and its impact to the practice of strong motion prediction, *Geophys. Res. Lett.*, 42, 2149–2156. doi: 10.1002/2015GL063335.

Kim, A., D. S. Dreger and S. Larsen (2010), Moderate Earthquake Ground-Motion Validation in the San Francisco Bay Area, *Bull. Seismol. Soc. Am.*, 100, 819-825.

Melgar, D. J. Geng, B. W. Crowell, J. E. Haase, Y. Bock, W. C. Hammond and R. M. Allen (2015), Seismogeodesy of the 2015 MW 6.1 Napa earthquake, California: Rapid response and modeling of the fast rupture on a dipping strike-slip fault, *J. Geophys. Res. Solid Earth*, 120, doi: 10.1002/2015JB011921.

Petersson, N. A. and B. Sjogreen (2013), User's guide to SW4, version 1.0, *Lawrence Livermore National Laboratory technical report*, LLNL-SM-642292.

Rodgers, A., N. A. Petersson, S. Nilsson, B. Sjogreen, K. McCandless (2008), Broadband waveform modeling of moderate earthquakes in the San Francisco Bay Area and preliminary assessment of the USGS 3D seismic velocity model, *Bull. Seismol. Soc. Am.*, 98, 969-988,, doi: 10.1785/0120060407.

Stidham, C., M. Antolik, D. Dreger, S. Larsen, and B. Romanowicz (1999), Three-dimensional structure influences on the strong motion wavefield of the 1989 Loma Prieta earthquake, *Bull. Seismol. Soc. Am.*, 89, 1184–1202.

3D Geologic and Seismic Velocity Models of the San Francisco Bay Region (2014), *United States Geologic Survey*. http://earthquake.usgs.gov/data/3dgeologic/, (website) accessed on April, 2014.

Wei, S., S. Barbot, R. Graves, J. L. Lienkaemper, T. Weng, K. Hudnut, Y. Fu and D. V. Helmberger (2015), The 2014 MW 6.1 South Napa earthquake: A unilateral rupture with shallow asperity and rapid afterslip, *Seismo. Res. Lett.*, 86, 344-354, doi: 10.1785/0220140210.

3 G-larmS: Real-time GPS for Earthquake Early Warning and the 2014 M_w 6.0 South Napa Earthquake

Ronni Grapenthin, Ingrid A. Johanson, Richard M. Allen, and Mario Aranha

Introduction

Earthquake early warning (EEW) exploits the differential propagation velocities of seismic body waves. By detecting the less destructive P-wave rapidly in real time, a warning is issued before the damaging S-wave arrives (*Allen and Kanamori,* 2003). Rapid estimation of magnitudes for large events from seismic data alone is known to fail as empirical frequency/amplitude-magnitude relationships saturate and instruments may not resolve the full dynamic range of the event in the near field (*Hoshiba et al.,* 2011). Over the last three years, we have developed G-larmS (The Geodetic Alarm System) to analyze GPS time series in real-time and estimate co-seismic offsets and finite fault models when triggered by a seismic alarm with the intention of rapidly providing magnitude updates for large earthquakes in Northern California.

Here we report a major update integrated into the system over the last year as well as its performance during the 2014 M_w 6.0 South Napa earthquake in California. The work presented here is a continuation of Grapenthin et al. (2013a,b, 2014a).

Data Processing

The data processing remains similar the previous strategy: Using data from 62 GPS stations (BARD, PBO, USGS) in Northern California, we generate real-time position estimates operationally for a fully triangulated network of 170+ station pairs (Figure 2.3.1). G-larmS analyzes the positioning time series, and determines static offsets and pre-event quality parameters. In case of an earthquake alarm, broadcast through CISN ShakeAlert, G-larmS derives and broadcasts finite fault and magnitude information through least-squares inversion of the static offsets for slip (*Grapenthin et al., 2014a).*

Parallelization of the Inversion

The inversion of surface displacements for slip on a fault is a problem that is non-linear in location and orientation of the fault, but linear for slip on the interface. To reduce the computational needs / necessary time to find a full solution we previously made the assumption that any detected earthquake ruptures parallel to the San Andreas Fault (SAF) (*Grapenthin et al.,* 2014a). Over the last year we made progress toward softening this constraint. To date, we are able to solve for slip on a number of pre-defined fault geometries in parallel. In the Bay Area, G-larmS currently tests three cases and picks the best model: SAF-parallel, SAF-conjugate and a Mt. Diablo-like thrust fault. This covers the majority of fault regimes; additional geometries can easily be added. A full search over the entire parameter space, or a Markov-Chain-Monte-Carlo method remain unrealistic to perform in real-time on a second-to-second basis.

2014 M_w 6.0 South Napa Earthquake

On August 24, 2014, G-larmS detected the M_w 6.0 South Napa earthquake in real time. In Grapenthin et al. (2014b) we report that G-larmS provided the first distributed slip model and magnitude estimate ~24 s after the event. Code optimizations reduced this in a simulated real-time environment to 14 s; ~8 s are S-wave travel time from the hypocenter to the nearest station, ~6 s are data latency. G-larmS' real-time and simulated real-time magnitudes capture the event well with M_w ~5.8 to 5.9 (Figure 2.3.1) and a reasonable first order slip model. However, the estimated static real-time offsets are overestimates for most stations when compared to post-processed results.

We investigated how the magnitude for the main shock compares to magnitude estimates for the small aftershocks, which did not induce measurable surface displacements. Figure 2.3.2 shows the results as the spread of magnitude estimates over the first 60 solutions for the real-time (151878) and replay (REPLAY) events and some of the aftershocks (M_w 2.2-3.9, ShakeAlert IDs 15184-15210). Clearly, the M_w 6.0, observed at a distance of 23 km is at the lower limit of resolution of the current rtGPS network for the region as some of the noise-based magnitude estimates reach, but rarely exceed the same event size. Even so, based on the respective level of misfit given in the lower panel of Figure 2.3.2, which is much larger for aftershocks with a suggested magnitude ≤ M_w 5.8, Grapenthin et al. (2014b) are comfortable suggesting that solutions for the M_w 6.0 Napa earthquake are real and not solely based on noise in the network.

Acknowledgements

This work is supported through the Gordon and Betty Moore Foundation, and CISN partners. We use data provided by the Plate Boundary Observatory operated by UNAVCO for EarthScope and supported by NSF (No. EAR-0350028 and EAR-0732947).

References

Allen, R. M., and H. Kanamori (2003), The Potential for Earthquake Early Warning in Southern California, *Science*, *300*(5620), 786–789, doi:10.1126/science.1080912.

Grapenthin, R. et al. (2013), G-larmS - Integrating Real-Time GPS into Earthquake Early Warning I: Implementation, *BSL Annual Report 2012-2013, 70-71, 2013a.*

Grapenthin, R. et al. (2013), G-larmS - Integrating Real-Time GPS into Earthquake Early Warning II: Testing, BSL Annual Report 2012-2013, 72-73, 2013b.

Grapenthin, R. et al. (2014), Operational Real-time GPS-enhanced Earthquake Early Warning, J. Geoph. Res., 119, doi:10.1002/2014JB011400, 2014a.

Grapenthin, R. et al. (2014), The 2014 Mw 6.0 Napa earthquake, California: Observations from real-time GPS-enhanced earthquake

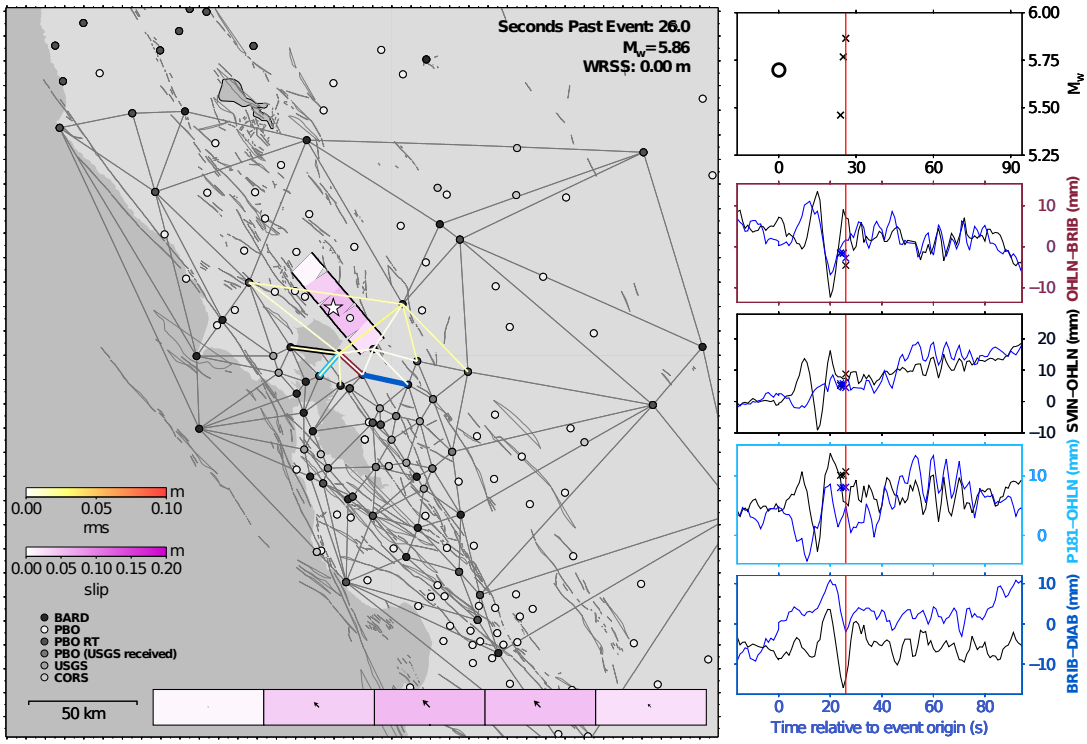

Figure 2.3.1: Real-time solution produced 26 s after the event origin time of the 2014 M_w 6.0 South Napa earthquake (first solution was at 24 s, event location given by black star). Left Panel: Model at 26 s after the event. White to yellow colored baselines indicate model misfit. Projection of vertical fault is shown in map view. Pink colors indicate slip amplitude. N-S (left to right) fault cross section is at the bottom of the panel: vectors give rake (right lateral) normalized to maximum rake of the final solution. Right Panels: Top panel shows time series of GPS-based magnitude, black circle shows initial ShakeAlert magnitude; bottom four panels show north (blue) and east (black) displacement time series for bold, colored baselines in middle panel. Crosses mark offsets derived along these baselines (time shift between GPS solutions and offsets is due to 6 s data acquisition and processing latency) (from Grapenthin et al. (2014b)).

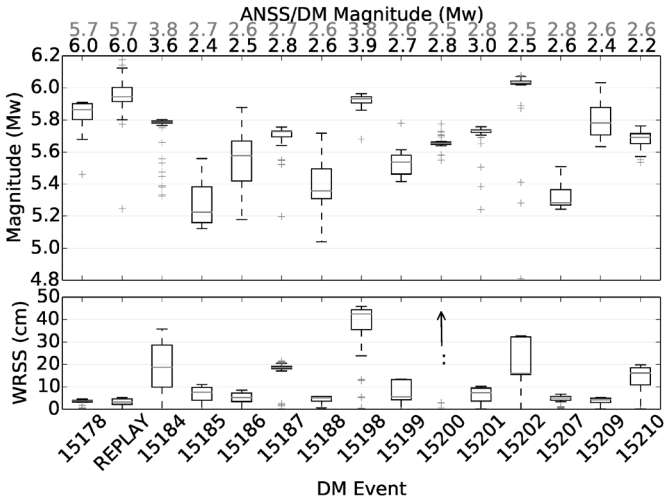

Figure 2.3.2: G-larmS results for M_w 6.0 main shock processed in real-time (15178) and replayed (REPLAY), and 13 aftershocks identified by ShakeAlert ID. Each box includes the first 60 results G-larmS produced for each event. Upper panel shows range of inferred magnitudes. Lower panel shows misfit of slip model (weighted residual sum of squares). Line in each box is median, boxes extend from 25th to 75th percentile, whiskers cover 1.5 times interquartile range, outliers are plotted individually. Vertical arrow in WRSS panel for event 15200 indicates that misfit is large (median ~140 cm). ANSS (black) and ShakeAlert (grey) magnitudes for each event are given on the upper horizontal axis (from Grapenthin et al. (2014b)).

early warning, Geophys. Res. Lett., 41, doi:10.1002/2014GL061923., 2014b.

Hoshiba, M., et al. (2011), Outline of the 2011 off the Pacific coast of Tohoku Earthquake (Mw 9.0) - Earthquake Early Warning and observed seismic intensity, Earth Planets Space, 63(7), 547–551, doi:10.5047/eps.2011.05.031.

4 Ambient Noise-Based Monitoring of Seismic Velocity Changes Associated with the 2014 M_w 6.0 South Napa Earthquake

Taka'aki Taira, Florent Brenguier (Université Joseph Fourier), Qingkai Kong

Introduction

The 24 August 2014 Mw 6.0 South Napa earthquake is the largest earthquake in the San Francisco Bay Area, California since the 1989 Mw 6.9 Loma Prieta earthquake. Inversions of seismic and geodetic data reveal a notable up-dip and northwest rupture directivity toward to the city of Napa. Here we explore temporal variations in seismic velocities associated with the 2014 South Napa earthquake through ambient noise cross-correlation analysis.

Data and Analysis

To estimate seismic velocity changes in and around the South Napa rupture area, we explore temporal properties of Green's functions (GFs) through cross-correlation analysis of ambient seismic noise wavefields (*Brenguier et al.*, 2008). Our analysis makes use of continuous seismic recordings from a set of 12 sites surrounding the rupture area of the 2014 South Napa mainshock. Noise cross-correlation functions (NCFs) are computed through MSNoise software (*Lecocq et al.*, 2014).

We use continuous recordings for a 57-month period (September 2010 through May 2015) spanning the 2014 South Napa earthquake. Our procedure of estimating NCFs is similar to that of Brenguier et al. (2008). First, seismic data were bandpassed between 0.08 and 2.0 Hz and they were decimated to 20 Hz. We applied a one-bit normalization and the waveforms were then whitened in a frequency range of 0.1–0.9 Hz. The resulting seismic data were cut into 30 minute-long-data. NCFs were computed for all possible pairs of stations and channels (*e.g.*, ZZ, ZN, ZE) for a lapse time between -120 and +120 s. Daily NCFs were obtained by stacking 30-min NCFs, and they were then stacked with a sliding window of five days with a one day step.

The velocity changes were estimated through a time-delay (dt) measurement between stacked and reference NCFs. The reference NCFs were determined as average NCFs during September 2010 through July 2014. A moving-window cross-spectral approach was applied to measure a relative time delay over lapse time (t). Assuming a homogeneous seismic velocity change, relative velocity change (dv/v) can be expressed as dv/v = -dt/t (*Brenguier et al.*, 2008; *Wegler et al.* 2009). We estimated dv/v for all possible pairs of stations and channels by fitting a slope (*i.e.*, dt/t) along the delay time measurement for the coda wave parts on NCFs ranging from -60 s to -20 s and +20 s to +60 s. The dv/v time series was computed by averaging dv/v over station and channel pairs.

Results

The dv/v time history, with a stack of five days, reveals a velocity reduction of about 0.08 % following the 2014 South Napa earthquake (Figure 2.4.1a). There is the long-term variation in dv/v before the South Napa mainshock. We regard this variation as apparent dv/v changes that might be due to seasonal variations of the noise source. We also explored a preseismic velocity change from the dv/v time history for a stack of five days (Figure 2.4.1b). There is no detectable dv/v change above noise preceding the South Napa earthquake.

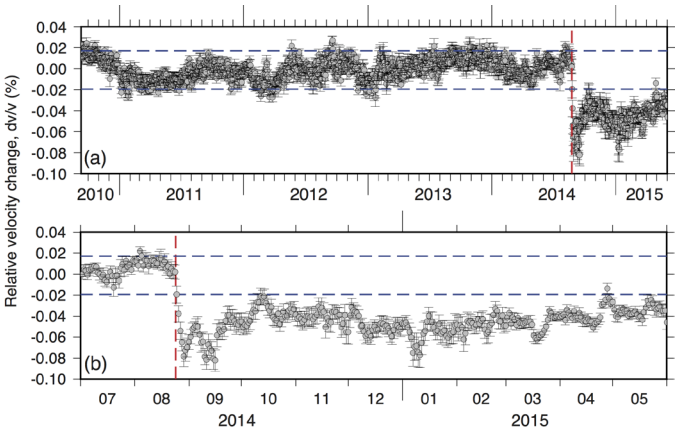

Figure 2.4.1: Time history of relative velocity change (dv/v) with two sigma standard deviations for stacks of five days in the time interval (a) September 2010 through May 2015 and (b) July 2014 through May 2015. Note that the dv/v was plotted at the end of the time window for stacking GFs. The red dashed line is the occurrence time of the 2014 Mw 6.0 South Napa earthquake. Blue dashed lines indicate the 95th percentile range of dv/v distribution obtained from data collected prior to the South Napa earthquake.

We determined the coseismic dv/v for individual pairs of stations by computing the median dv/v and variance in the first 50–75 days of the post-South Napa earthquake period with a stack of 50 days. We only consider the pairs of stations where the 95th percentile range of dv/v is less than 0.1% in a one-year period before the South Napa earthquake for further analysis (Figure 2.4.2). Following Hobiger et al. (2012), we assumed that a velocity change obtained for a pair of stations is a mean of the local velocity change beneath the two stations, and obtained the coseismic dv/v at each station (hereafter referred as the station dv/v) by using a linear least-squares inversion. Repeated inversions were performed for the 495 subsets that were obtained from the pairs of stations using 8 stations (*i.e.*, deleting 4 stations from the total 12 stations). The median and 95 percent confidence interval (dv/v95) was then determined from the distribution of the station dv/v at each site. The six sites with dv/v95 less than 0.1% were used for discussion. Among those six sites, the largest median station dv/v (-0.098%) was found at station NHC that is the closest site (~3.7 km) to the hypocenter of the 2014 South Napa earthquake.

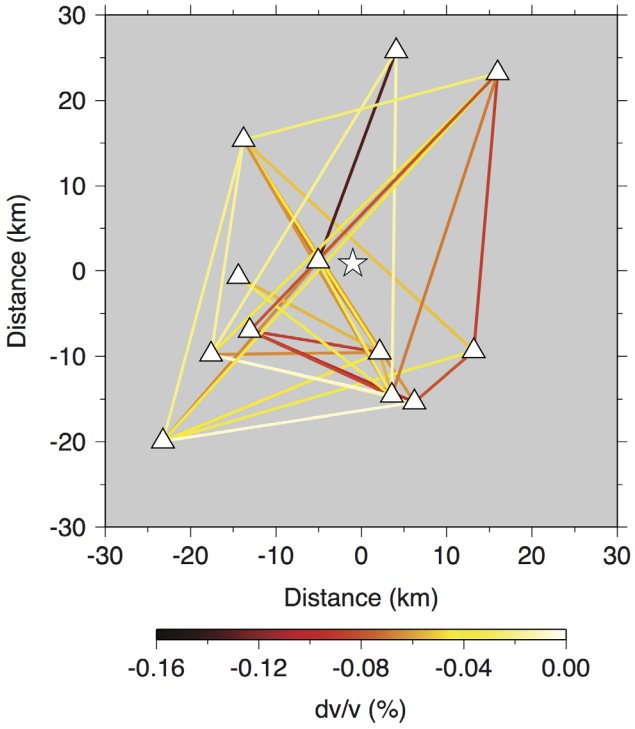

Figure 2.4.2: dv/v measurements for pairs of stations. The white star is the epicenter of the 2014 South Napa earthquake. Values of dv/v are represented by the color code in the bottom of this figure.

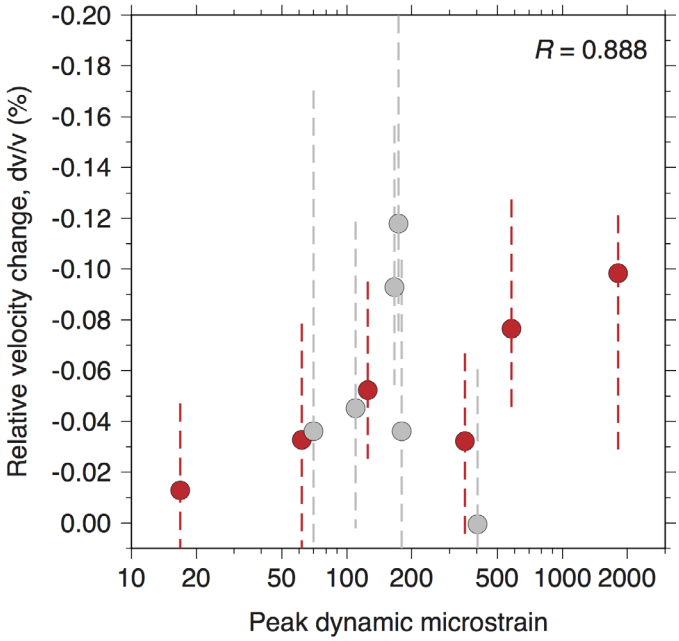

Figure 2.4.3: Median station dv/v as a function of peak dynamic strain. Dashed lines indicate the 95th percentile range (dv/v95) of station dv/v obtained through the Jackknife test. Red and gray circles indicate stations with dv/v95 < 0.1% and dv/v95 >= 0.1%, respectively. The correlation coefficient (R) is determined from the six sites with dv/v95 < 0.1%.

Discussion

The time history of dv/v with a stack of five days reveals a marked decrease of dv/v immediately after the South Napa earthquake. Although we were not able to constrain the depth of the velocity change, they likely occurred within the seismogenic depth (< ~10 km). We made use of the peak ground velocity (PGV) measurement to estimate the effect of dynamic stress changes imparted by the South Napa earthquake. A strong ground shaking will create new fractures leading to a decrease of seismic velocity. The dynamic peak strain was estimated by dividing PGV by the local shear wave velocity. The level of the station dv/v appears to be correlated with the dynamic peak strain (Figure 2.4.3). Using the six stations having dv/v95 less than 0.1%, the correlation coefficient (R) between the median station dv/v and the dynamic peak strain is 0.888, which satisfies the t-test statistic for significance above 95% level (R = 0.811). We conclude that the coseismic velocity change is most likely due to new fractures created by the dynamic stress change from the South Napa earthquake.

Conclusion

Ambient noise-based monitoring seismic velocity reveals a coseismic velocity reduction of ~0.08% following the 2014 M_w 6.0 South Napa earthquake. The spatial variability of velocity change is correlated with the map of the dynamic peak strain estimate. We propose that the dynamic stress from the South Napa mainshock created new fractures leading to this coseismic velocity reduction.

Acknowledgements

We thank A. T. Roger for helping to extract shear-wave velocity models at individual seismic stations, R. Bürgmann, M. Floyd, G. Funning, C.-Y. Wang, and M. Manga for discussion about postseismic deformation and groundwater data. Waveform data, metadata, and earthquake catalogs for this study were accessed through the Northern California Earthquake Data Center (NCEDC) (NCEDC, 2014). This study was supported by the France-Berkeley Fund 2014-0051 and the National Science Foundation EAR-1053211.

References

Brenguier, F., Campillo, M., Hadziioannou, C., Shapiro, N. M., Nadeau, R. M., Larose, E. (2008), Postseismic Relaxation Along the San Andreas Fault at Parkfield from Continuous Seismological Observations, *Science*, 321, 1478–1481, doi:10.1126/science.1160943.

Hobiger, M., Wegler, U., Shiomi, K., Nakahara, H. (2012), Coseismic and postseismic elastic wave velocity variations caused by the 2008 Iwate-Miyagi Nairiku earthquake, Japan, *J. Geophys. Res.*, 117(B9), B09313, doi:10.1029/2012JB009402.

Lecocq, T., Caudron, C., Brenguier, F. (2014), MSNoise, a Python Package for Monitoring Seismic Velocity Changes Using Ambient Seismic Noise, *Seismol. Res. Lett.*, 85(3), 715–726, doi:10.1785/0220130073.

NCEDC, Northern California Earthquake Data Center (2014) UC Berkeley. Seismol. Lab. Dataset, doi:10.7932/NCEDC.

Wegler, U., Nakahara, H., Sens-Schönfelder, C., Korn, M., Shiomi, K. (2009), Sudden drop of seismic velocity after the 2004 Mw 6.6 mid-Niigata earthquake, Japan, observed with Passive Image Interferometry, *J. Geophys. Res.*, 114(B6), B06305, doi:10.1029/2008JB005869,.

5 Annual Performance Update for the ElarmS Earthquake Early Warning System (June 1, 2014 – June 1, 2015).

Angela I. Chung, Ivan Henson, Richard M. Allen, Margaret Hellweg, Doug Neuhauser

Introduction

The ElarmS earthquake early warning system has been providing real-time alerts for earthquakes within California since 2007 (*Allen*, 2007). Though originally developed for use in California, the system is now also being tested along the Western US, in Israel, Turkey, and Chile. In 2014, ElarmS was updated significantly to ElarmS version 2 (ElarmS-2 or E2) (*Kuyuk et al.*, 2014).

Here, we review the performance of E2 in California for the past year (2014-06-01 through 2015-06-01), demonstrating the system's ability to rapidly and accurately characterize earthquakes.

Earthquake Detections

Overall, E2 performance has been excellent. Over the past year (2014-06-01 through 2015-06-01), the E2 system successfully detected all but two of the significant earthquakes (magnitude greater than M4) that occurred within California. Of the 25 events that were detected, the most notable was the M6.0 South Napa earthquake that struck on August 24, 2014. The first alert for this event was sent in 5.1 seconds with an initial magnitude estimate of M5.7. This alert provided approximately 5 seconds of warning to people in Berkeley, and 8 seconds of warning to those in San Francisco. The magnitude estimate increased to the final value of M6.0 within 15 seconds of the initial alert.

One of the four events of magnitude greater than M4 that were not detected by E2 was a M4.4 earthquake that occurred within 30 seconds of the M6.0 South Napa mainshock. Because the smaller earthquake began very close in time to the arrival of S-waves from the Napa earthquake, it failed to register as a distinct event. The other three missed events occurred in regions with sparse station coverage. The E2 system is capable of detecting earthquakes as small as M2. However, even moderate-sized events can be missed if they occur in remote areas with poor station coverage. E2 requires triggers from at least 4 stations in order to alert from an event, which can be problematic if there are not enough stations nearby.

On May 30, 2015 an extraordinarily deep (678km) M7.8 teleseism in Japan generated 7 false event detections within a minute (5 greater than M4, shown in Figure 2.5.1). This large number of false alerts was due to the simultaneous arrival of the P-waves from Japan at stations throughout California. Though E2 uses a teleseismic filter to prevent alerts due to distant earthquakes, because of the unusual nature of the Japan earthquake, the filter did not successfully prevent an alert from being disseminated. The E2 team is exploring ways to improve the teleseismic filter. In addition to the aforementioned false events due to the teleseism, 2 other false alerts were created by a computer reboot and restart of E2. Upon restart, E2 was able to receive triggers before checking which stations were active.

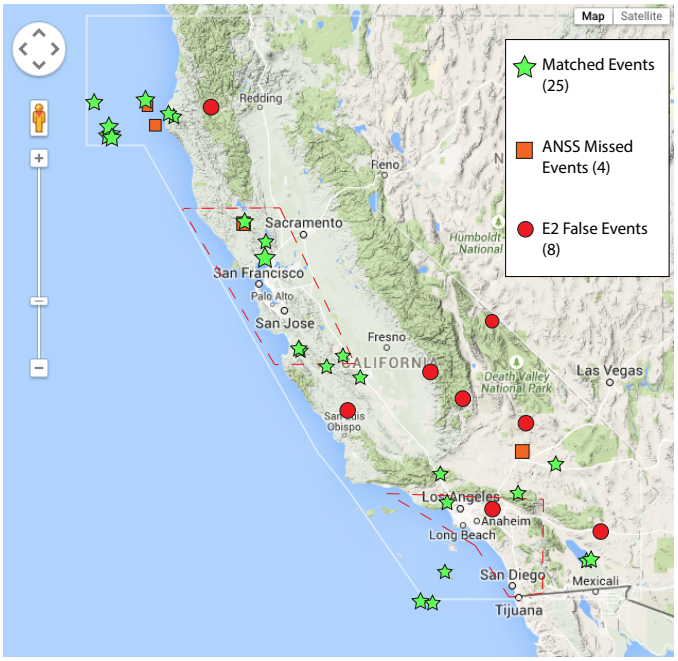

Figure 2.5.1 Map showing ElarmS performance from 2014-06-01 through 2015-06-01 for events greater than M4. Events detected by E2 and listed in the ANSS catalog are "Matched Events" (green stars). Events listed in the ANSS catalog but not detected by E2 are "ANSS Missed Events" (orange squares). Events that generated an alarm by E2, but which were not associated with local events are "E2 False Events" (red circles). Dashed lines depict Bay Area and Los Angeles regions. White line is the California boundary. Figure from E2 Review Tool, modified for publication.

This allowed E2 to form events using stations that were very far apart because the nearby stations had not yet registered as being active. This problem has since been remedied by forcing E2 to upon startup wait until it receives the first information regarding which stations are active before it forms events. The eighth false event created by E2 was triggered by an earthquake in the Mammoth region. A cluster of stations in this region are usually treated as a single station by E2, however one station was missing from this list, which caused the event to have a very poor location estimate (>100 km error). This problem has since been remedied.

Magnitude and Location Estimates

It can be difficult to accurately locate and estimate the magnitude of an earthquake that occurs outside of a seismic network due to the lack of good azimuthal coverage. This difficulty can be clearly seen by examining the magnitude and location estimates by E2 over the past year. The mean initial magnitude estimate error by E2 for all events greater than M4 that were detected during that time is 0.14 magnitude units, with a standard deviation of 0.56 magnitude units. The mean final magnitude

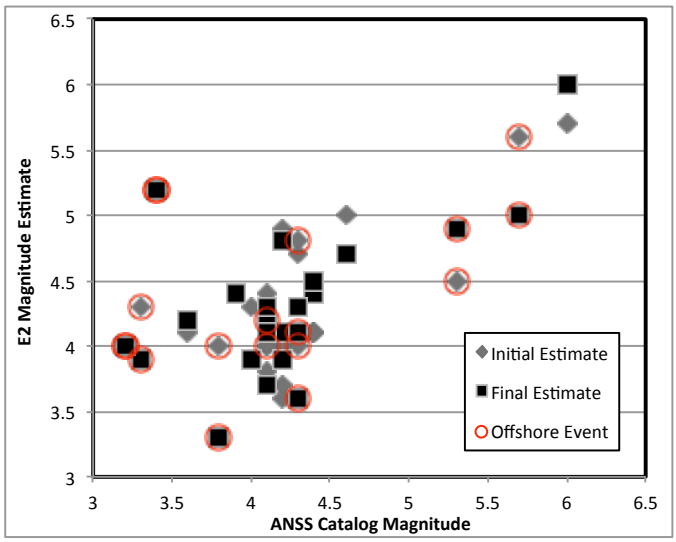

Figure 2.5.2 Comparison of E2 estimated magnitudes for events greater than M4 and ANSS Catalog listed magnitudes. Estimates for offshore events are circled in red.

estimate error for all events is 0.07, with a standard deviation of 0.53. If all events that are offshore California are excluded, the mean initial and final magnitude estimates are reduced to -0.03 and 0.06, respectively, with standard deviations of 0.39 and 0.29.

Similarly, initial E2 location estimates for all M>4 events have a mean location error of 29.03 km and a standard deviation of 32.45 km. However, for only those events onshore within California, the mean location error and standard deviation are 7.30 km and 7.13 km, respectively. The final E2 location estimates for all events have a mean error of 25.20 km and a standard deviation of 27.61 km; Events within onshore California have a final mean error of 9.26 km with a standard deviation of 11.22 km.

	M>4 (California)	M>4 (Bay Area)	M>4 (Los Angeles)
Matched Events	25	6	1
ANSS Missed Events	4	1	0
False Events	8	0	1

Table 2.5.1 E2 performance statistics for events greater than M4 during the time period 2014-06-01 through 2015-06-01. Statisics for all of California are in the left column, those for only the Bay Area region are in the center column, and those for the Los Angeles region are in the right column. Bay Area and Los Angeles regions depicted by dashed line in Figure 2.5.1.

Recent Updates

Over the past year, the following updates have been implemented:

- *California-specific code has been replaced with a configurable code that allows E2 to be easily adapted to other locations, such as Israel, Turkey, and Chile.*
- *Improved logging of information from the event associator process to make reviewing the values of alert criteria variables easier for both alerted events and events that failed one or more of the alert criteria.*
- *Added data packet latency measurements and ability to log directly to the E2 waveform processing and event association programs.*

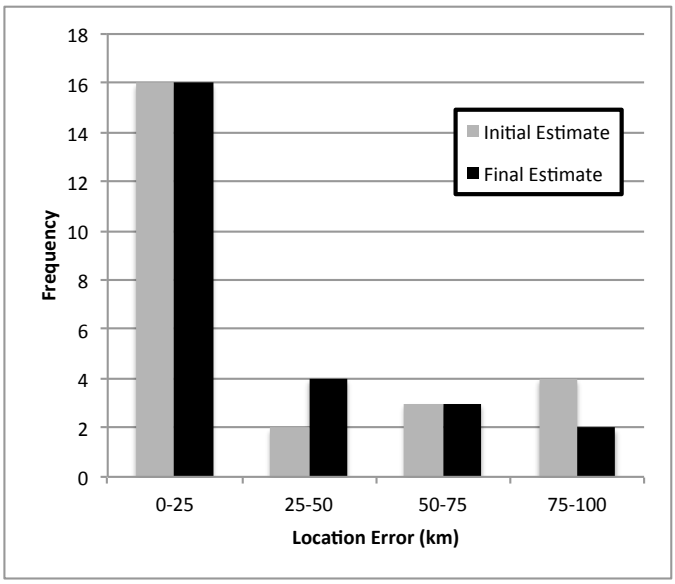

Figure 2.5.3 Histogram showing location errors of E2 locations from initial alert (grey) and from the last alert update (black) for E2 events greater than M4. One event with initial location error > 100km was an offshore earthquake; the other was an event in California near to Nevada.

Future Work

In order to improve the speed and accuracy of detections, we are currently exploring new methodologies to quickly evaluate incoming triggers from individual stations. Rapidly determining whether or not a trigger at a given station is due to a local earthquake or some other source could dramatically increase the confidence in individual triggers. This may help E2 to accurately distinguish local from distant earthquakes and may also allow the E2 system to generate alerts for an earthquake using fewer than the 4 stations currently required.

Acknowledgements

This project is possible thanks to the collaborative efforts of many people working at the CISN operating institutions: UC Berkeley, Caltech, USGS Menlo Park and USGS Pasadena. This work is funded by USGS/NEHERP awards G09AC00259 and G12AC20348, and by the Gordon and Betty Moore Foundation through Grant GBMF3024 to UC Berkeley.

References

Kuyuk, H. S., R. M. Allen, H. Brown, M. Hellweg, I. Henson, and D. Neuhauser, Designing a Network-Based Earthquake Early Warning Algorithm for California: ElarmS-2, BSSA, 104, No. 1, 2014.

Allen, R. M., The ElarmS earthquake early warning methodology and application across California, Earthquake Early Warning, P. Gasparini (Editor), Springer, Milan, Italy, 21–43, 2007.

6 Earthquake Early Warning Performance in the M6.0 South Napa earthquake: ElarmS and ShakeAlert

Richard Allen, Margaret Hellweg, Ivan Henson, Doug Neuhauser, Jennifer Strauss.

Introduction

UC Berkeley is operating two earthquake early warning algorithms. ElarmS is a point-source seismic algorithm that contributes data to the West Coast ShakeAlert demonstration system (see Research Section 2.5). GlarmS, in contrast, is an algorithm that uses geodetic data from Global Navigation Satellite System (GNSS) receivers to rapidly estimate a finite fault for larger earthquakes as they occur and thus provide more robust estimates of their magnitudes (see Research Section 2.3). It is currently operating in testing mode. Both algorithms were running during the August 24, 2014 M6.0 South Napa earthquake and produced excellent results. The performance of GlarmS in the South Napa quake is described in Research Section 2.3. The performance of the West Coast ShakeAlert system was defined by the ElarmS processing.

ElarmS Performance in the M6.0 South Napa Earthquake

The August 24, 2014 South Napa earthquake took place at 03:20:44.4 PDT at a depth of about 10 km. Its P-wave arrived at the nearest station NC.NHC, 6.5 km from the epicenter 1.8s later. Triggers at the next nearest three stations, NC.NGVB, NC.NTO and BK.CVS followed within 2.1s of the first trigger (Figure 2.6.1). Their epicentral distances range between 10 and 21.6 km. Data from these four stations contributed to ElarmS' first alert which was sent to the Decision Module of the ShakeAlert system 5.1s after the rupture started, with a magnitude of 5.7. The latencies of the data from the four stations contributing to the first alert ranged from 0.27 to 2.62 s, resulting in an overall delay of 1.2 s. In fact, data from the closest station was the last to arrive. Had there been no telemetry delay, the blind zone would have been smaller and the city of Napa could have received an alert about one second before the arrival of the first S-waves. Overall the magnitude estimate and event location were stable from the initial alert onwards. Recent improvements to the configuration of ElarmS and the requirements on earthquake early warning station density and data feeds now allow very rapid reporting of earthquake parameters for ShakeAlert.

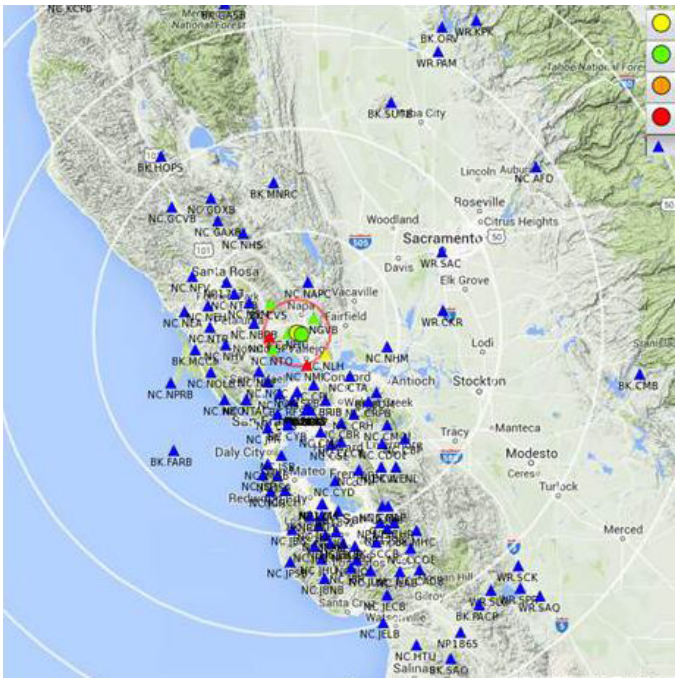

Figure 2.6.1 ElarmS performance in the M6 South Napa earthquake. The first alert was delivered 5.1s after the earthquake rupture began, when data from the four nearest stations, NC.NHC, NC.NGVB, NC. NTO and BK.CVS, had been processed.

Figure 2.6.2 Warning times for UCB ShakeAlert partners for the M6 South Napa earthquake.

Using EEW Alerts

UC Berkeley has been working with local organizations and institutions to develop applications for ShakeAlert. In particular, our Earthquake Research Affiliates (ERA) partner, BART, has implemented plans to slow and stop trains when the EEW system declares an earthquake. Although no trains were running at the time of the South Napa earthquake early Sunday morning, the ShakeAlert warning triggered BART's response applications, and any operating trains would have been slowed. Other ERA partners (See Section 3.46), including the UC Berkeley police, the San Francisco Department of Emergency Management and Google received 5, 9 and 20 s of warning (Figure 2.6.2).

Perspectives

The M6.0 South Napa earthquake was an exciting validation of the West Coast ShakeAlert demonstration earthquake early warning system, and the contributions ElarmS and GlarmS are making to it. It also highlighted both the need to upgrade seismic stations to provide data as quickly as possible, and the improvements that such upgrades can make toward increasing warning times.

Acknowledgements

This project is possible thanks to the collaborative efforts of many people working at the CISN operating institutions: UC Berkeley, Caltech, USGS Menlo Park and USGS Pasadena. This work is funded by USGS/NEHERP awards G09AC00259 and G12AC20348, and by the Gordon and Betty Moore Foundation through Grant GBMF3024 to UC Berkeley.

7 Tectonics of the South Napa Earthquake

Kathryn Materna, Mong-Han Huang, Diego Melgar, Ingrid Johanson, Chris Johnson, Sierra Boyd, Kathryn Woodell, Taka'aki Taira, Douglas Dreger, Richard Allen, Mike Floyd, Gareth Funning

Introduction

The M_w 6.0 South Napa earthquake, on August 24, 2014, was the strongest earthquake to hit the Bay Area in 25 years. It occurred in an area with good seismic and geodetic coverage, producing a wealth of data. In the wake of the earthquake, scientists at the BSL contributed to many efforts to understand the tectonics and source behavior of this earthquake. We utilized primarily seismometers, continuous GPS, survey GPS, and InSAR. The following is a summary of the BSL's research findings regarding the tectonic and seismic behavior of the South Napa earthquake.

InSAR and Continuous GPS

One of the major projects of the BSL after the South Napa earthquake was a joint seismic-GPS-InSAR inversion for the earthquake's source parameters (*Dreger et al.*, 2015). The seismic network and the continuous GPS network used in the inversion are part of the Berkeley Digital Siesmic Network and the Plate Boundary Observatory respectively.

The two InSAR acquisitions used in the inversion were an ascending track from COSMO SkyMed between July 26 and August 27, and a descending track from the same satellite between June 19 and September 3. With InSAR, there is always the concern that the deformation represented in an interferogram contains both co-seismic and post-seismic signal that cannot be distinguished individually. However, in the case of the InSAR of the South Napa earthquake, it appears that the post-seismic deformation signal in each of the interferograms is small. The total moment of the earthquake as calculated from each interferogram is not significantly larger than the seismic moment of the South Napa earthquake when calculated from seismic data.

The results of the joint inversion in Dreger et al. show a quickly propagating rupture that begins at a hypocenter 11 kilometers deep. In their preferred model of the source parameters, the rupture propagated to the northwest and up toward the surface, showing a pattern that directed energy toward the town of Napa. The rupture propagation speed was 85% of the shear wave speed of the rocks, meaning that the propagation was very fast. In their model, the average slip on the rupture plane was 0.23 meters, and the maximum slip was 1.15 meters. They also found that the surface rupture is 1.8 kilometers west of the previously mapped surface trace of the West Napa Fault, suggesting that the fault may have a complicated near-surface structure.

High-Rate GPS

Another major effort of the BSL was to utilize high-rate GPS for studying the source parameters of the earthquake. The South Napa earthquake, at M_w 6.0, in fact pushes the boundary of what we can study with this technique; most studies that use high-rate GPS are concerned with much larger events. Melgar et al. (2015) used high-rate (1-5 Hz) data from the stations shown in Figure 2.7.1 to invert for source parameters of the South Napa earthquake. Treating the GPS data in the same way that seismic data has been used traditionally (Figure 2.7.2), Melgar et al. found that the GPS data could be used to produce a static slip inversion, a map of peak ground displacement, and a centroid moment tensor. Furthermore, the GPS data could be used to produce these quantities in near real-time. They demonstrated that the GPS-only calculations compared well with seismic inversions and moment tensor calculations, and that joint GPS-seismic inversions have the potential to be more accurate than either GPS or seismic alone.

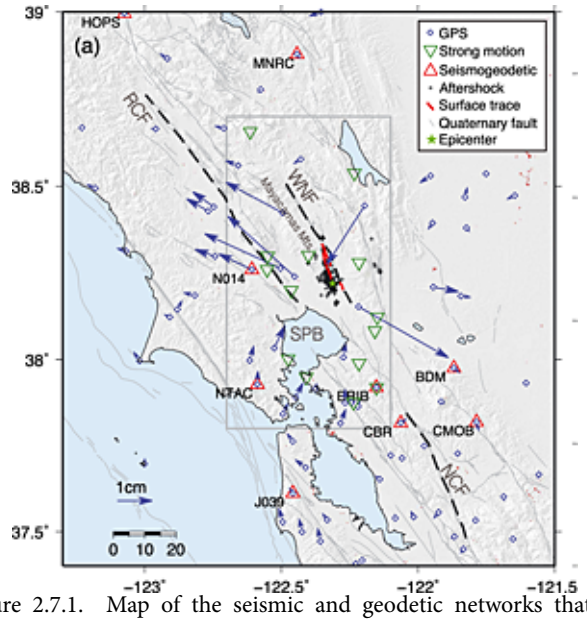

Figure 2.7.1. Map of the seismic and geodetic networks that recorded the South Napa earthquake. Blue circles and arrows show the coseismic displacements of continuous GPS stations in the Plate Boundary Observatory and the Bay Area Regional Deformation networks. Green triangles show strong motion seismometers. Red circles show co-located seismometers and high-rate GPS receivers. The surface trace of the West Napa Fault is shown in red. Map is from Melgar et al., 2015.

The results of their combined high-rate GPS and seismic calculations showed that the South Napa earthquake ruptured with a strong directivity pattern; this is generally consistent with the InSAR/GPS/seismic inversion from Dreger et al. and with other seismic inversions. The results also show that the surface rupture appears to cut through a layer of soft sediments in Napa Valley. Based on these results, it seems likely that the shallow parts of the fault include a so-called "flower structure," indicating that different earthquakes break to the surface through different shallow-branching strands of the fault.

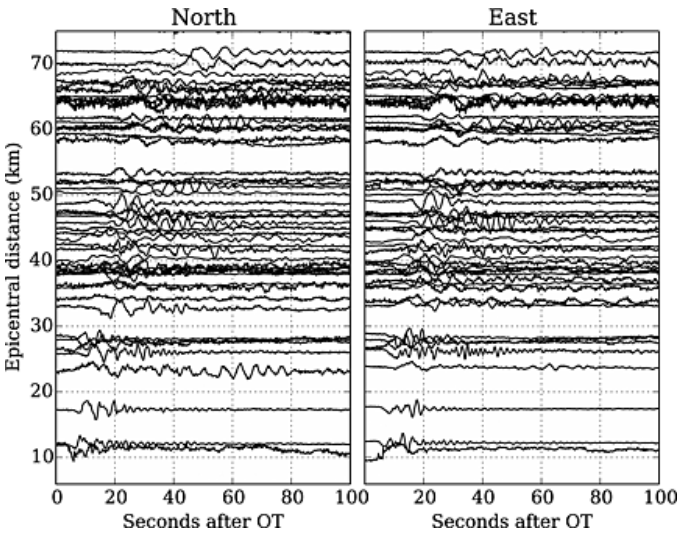

Figure 2.7.2. High-rate GPS time series showing the first arrival of seismic waves from the South Napa earthquake. From Melgar et al., 2015.

Survey GPS

In the days after the earthquake, scientists at the BSL also helped in the rapid deployment of about 13 near-field campaign GPS sites in Napa and Sonoma Counties. Through coordination with colleagues at UC Riverside, MIT, and the USGS, all 13 sites were re-occupied within the first 15 hours after the earthquake. The BSL helped collect the data and keep the stations running for more than two weeks after the earthquake in order to measure aftershocks and post-seismic deformation.

The results from this campaign contributed to our understanding of the South Napa earthquake in important ways. Compared to the continuous GPS measurements, the survey provided higher spatial density. The closest continuous station was about 15 kilometers from the rupture, while all 13 survey sites were within 20 kilometers of the epicenter. Compared to InSAR, the GPS data began at an earlier time, allowing better separation between coseismic and post-seismic offsets.

The co-seismic displacements from the GPS survey show that at the stations closest to the fault, approximately two kilometers away, the maximum offset was more than 20 centimeters. This decayed to about 2 centimeters of co-seismic offset at distances of 15-20 kilometers from the epicenter. The data from this campaign also showed that for most sites, the post-seismic deformation decayed to very small rates within two weeks.

Acknowledgements

For the work described in this summary, the BSL gratefully acknowledges all of the co-authors and colleagues who contributed to the papers and abstracts shown below. Each of these represents a large collaborative effort between many separate people, institutions, and research groups.

References

Dreger, D., Huang, M.H., Rogers, A., Taira, T., and Woodell, K., 2015, Kinematic Finite-Source Model for the 24 August 2014 South Napa, California, Earthquake from Joint Inversion of Seismic, GPS, and InSAR data: *Seismological Research Letters,* 86(2A), p. 327-334.

Melgar, D., Geng, J., Crowell, B., Haase, J., Bock, Y., Hammond, W., and Allen, R., 2015, Seismogeodesy of the 2014 M6.1 Napa Earthquake, California: Rapid response and modeling of fast rupture on a dipping strike-slip fault: Journal of Geophysical Research Solid Earth, 120, DOI: 10.1002/2015JB011921.

Floyd, M., G. Funning, J. Svarc, T. Herring, I. Johanson, J. Swiatlowski, K. Materna, C. Johnson, O. S. Boyd, J. Sutton, and E. Phillips (2014), Surface deformation before, during, and after the 2014 South Napa, California earthquake from a spatially dense network of survey and continuous GPS sites, Abstract S33F-4904, presented at 2014 Fall Meeting, AGU, San Francisco, Calif., 15-19 Dec., 2014.

Research Studies:
Planetary and Mineral Physics

University of California
Berkeley
Seismological Laboratory

9 Synchrotron X-rays Record Residual Stress Preserved in Quartz from the San Andreas Fault Observatory at Depth

Rudy Wenk

Introduction

As part of on-going studies to characterize fault gouge (*Janssen et al.* 2012) and enigmatic pseudotachylites (*Wenk et al.* 2000, 2011) and link microstructural features to seismic events, we have been investigating samples from the SAFOD drill core retrieved from a depth of over 2.7 km, in the vicinity of the currently active San Andreas Fault near Parkfield. In this study Rudy Wenk with colleagues from the Berkeley Advanced Light Source used synchrotron X-rays to document lattice distortions in cataclastic quartz that can be attributed to seismic events. Results were reported in a recent issue of Geology (*Chen et al.* 2015) and raised a lot of interest, including headlines in DOE reports.

Methods

A thin section of the rock was prepared and under a petrographic microscope with crossed polarizers it shows fractured quartz grains with fractures partially filled by calcite veins (Figure 2.9.1A). A polychromatic X-ray beam (5 – 24 keV) of synchrotron X-rays at beamline 12.3.2 of the Advanced Light Source was focused to ~1 × 1 μmm^2 and Laue diffraction images (Figure 2.9.2) were recorded in reflection mode (Figure 2.9.2). Laue microdiffraction has been developed by materials scientists to characterize texture, strain and stress on a sub-grain level (e.g., *Ice et al.,* 2011). Residual stress – i.e. stress that is still preserved in the crystal on a microscopic scale after macroscopic deformation has seized - has been investigated in metals for a long time, documenting lattice distortions with diffraction evidence (e.g., *Noyan and Cohen,* 1987). Here we present a first application of this powerful technique to investigate residual stress in quartz from an active earthquake zone. From the Laue image we obtain information about the crystal orientation at a 1 mm spot, as well as the preserved stress state. Four scans were performed. Step size was 4 mm. Exposure time at each position was 1 s. Results from one scan are shown in Figure 2.9.1B,C. For comparison, a scan was also performed on a thin section of a synthetic quartz crystal prepared and analyzed using the same methodology as for the SAFOD sample. All diffraction patterns (~40000) were analyzed automatically by the local software package XMAS. The difference between the observed reflection positions and the ones calculated based on the assumption of an unstrained lattice are used to calculate the deviatoric strain tensor ε'. The magnitude of the deviatoric strain tensor can be expressed as a scalar by the "equivalent strain" which is defined as:

$$\varepsilon_{eq}' = \frac{2}{3}\sqrt{\frac{(\varepsilon'_{11}-\varepsilon'_{22})^2+(\varepsilon'_{22}-\varepsilon'_{33})^2+(\varepsilon'_{33}-\varepsilon'_{11})^2+6(\varepsilon'^2_{12}+\varepsilon'^2_{13}+\varepsilon'^2_{23})}{2}}$$

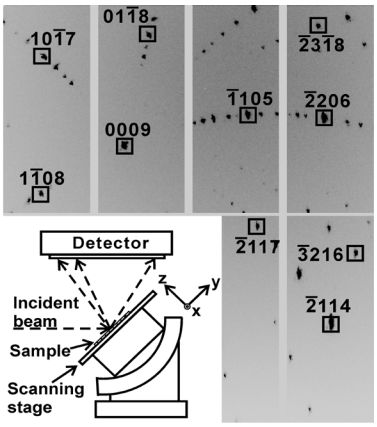

Figure 2.9.2. Laue diffraction image of quartz crystal from the SAFOD gouge zone investigated in this study. The sample is placed at 45° relative to the incoming beam.

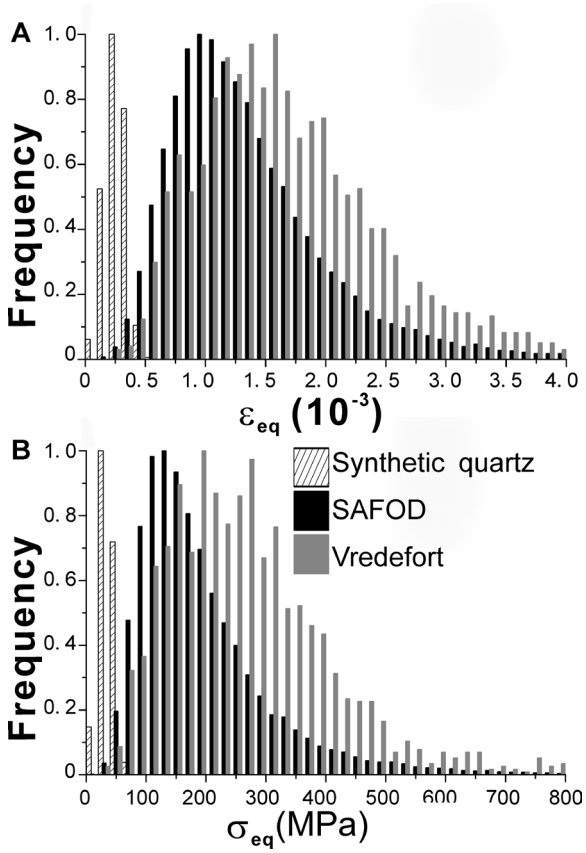

Figure 2.9.3. Distribution histograms for equivalent strains (A, in 10^{-3}) and equivalent stress (B, in MPa). The equivalent strain and stress distributions of a strain-free synthetic quartz, is compared with the average over four scans from SAFOD fault gouge and quartz from the Vredefort meteor impact crater.

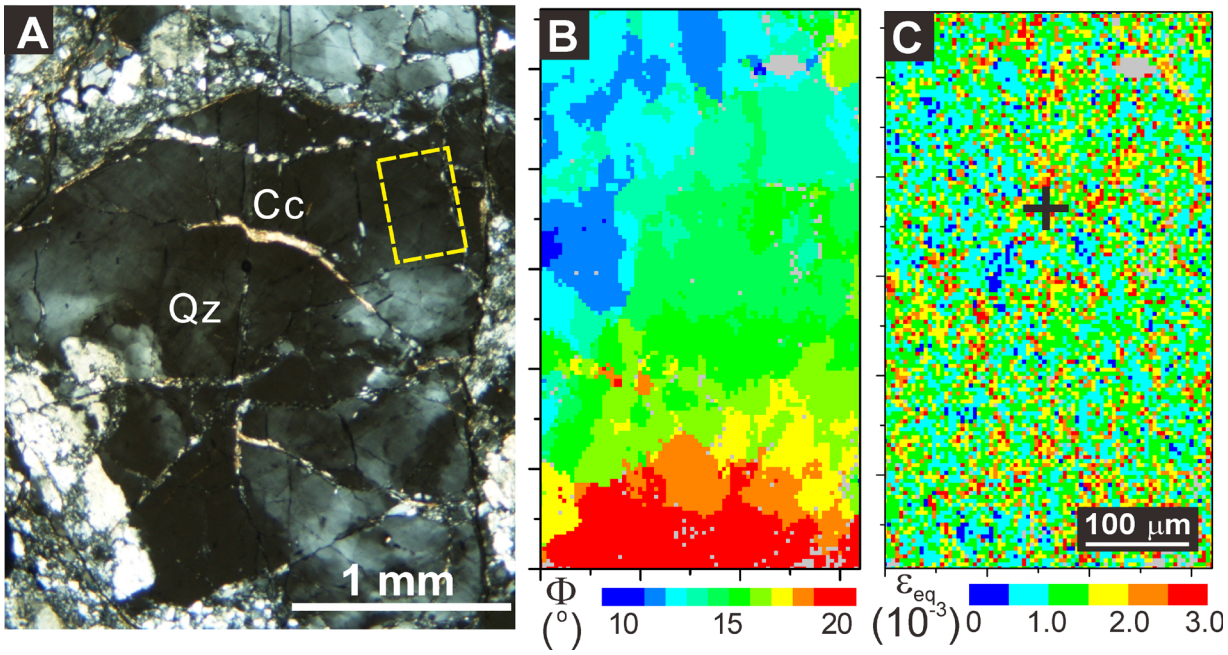

Figure 2.9.1: A) Optical micrograph of SAFOD gouge investigated in this study. B) Map of Euler angle F that defines the tilt of the crystal c-axis relative to the sample surface. C) Map of equivalent strain (in 10^{-3} units). The black cross refers to the position where the Laue pattern depicted in Figure 2.9.2 was exposed.

where e'_{ij} (i, j = 1–3) are the components of the strain tensor. The stress tensor (s_{ij}) in turn is calculated from the strain tensor and the elastic stiffness constants (C_{ijkl}) for trigonal quartz by applying Hooke's law $s_{ij} = C_{ijkl}\ e'_{kl}$. Figure 2.9.1A shows the position of one scan within the petrographic thin section. Figure 2.9.1B shows a map of Euler orientation angle F, which indicates minor bending ~10°. The corresponding map of equivalent strain (Figure 2.9.1C) displays residual strain with coherent areas exceeding 2×10^{-3} strains (orange red).

Findings

The range and frequency of strain values measured in the SAFOD sample can be displayed in histograms (Figure 2.9.3). The distribution peaks at 1×10^{-3} (Figure 2.9.3A). Strain can be converted to residual stress values, which are shown in Figure 2.9.3B. The equivalent stress peaks around 130 MPa, with a range from 40 to 600 MPa. This is highly significant against the instrumental resolution of ~40 MPa measured on the synthetic quartz crystal.

For us the most likely explanation is to attribute the observed high stress to seismic shock events. Such a mechanism can explain the high local strains observed in a matrix of weak phyllosilicates. The stress peaks in quartz were probably acquired during an earlier phase of the San Andreas Fault history. Currently measured macro-strengths are much lower (20-50 MPa) and may not represent the original strength of rocks (e.g. *Lockner et al.* 2011).

It is interesting to compare our findings with similar measurements from a rock subjected to a meteor impact shock event. As can be seen in the histograms in Figures 2.9.3A and 2.9.3B, elastic strains and stresses preserved in quartz from a stishovite-bearing quartzite from the Vredefort meteor crater in South Africa (*Chen et al.,* 2011) are slightly higher than the SAFOD distributions (~1.4×10^{-3} strain and 200 MPa, respectively). The fact that in the case of Vredefort such high strains can be stored in a quartz grain for up to billions of years is due to the strong confinement of the individual grain within the rock matrix.

With this exploratory study of cataclastic quartz from a fault zone we have become aware of the potential of Laue X-ray microdiffraction to determine residual stress in minerals as a paleopiezometer. We are impressed by the possibility to use this method in the future not only to record stress intensities but also stress directions in deformed rocks.

References

Chen K., Kunz M., Tamura N., Wenk H.-R. 2015. Seismic stress preserved in quartz from San Andreas Fault. Geology 43, 219-222.

Chen K., Kunz M., Tamura N., Wenk H.-R., 2011, Evidence for high stress in quartz from the impact site of Vredefort, South Africa: European J. Mineralogy, 23, 169–178.

Harrington R.M., Brodsky E.E., 2009, Source duration scales with magnitude differently for earthquakes on the San Andreas Fault and on secondary faults in Parkfield, California: Bulletin of the Seismological Society of America, 99, 2323–2334.

Lockner D.A., Morrow C., Moore D., and Hickman S., 2011, Low strength of deep San Andreas Fault gouge from SAFOD core: Nature, 472, 82–85.

Tamura N., 2014, XMAS: A versatile tool for analyzing synchrotron X-ray microdiffraction data, in Ice, G.E., and Barabash, R., eds., Strain and Dislocation Gradients from Diffraction: London, Imperial College Press, p. 125–155.

10 High-pressure, Temperature Elasticity of Fe- and Al-bearing MgSiO3: Implications for the Earth's Lower Mantle

Shuai Zhang, Sanne Cottaar, Tao Liu, Stephen Stackhouse, Burkhard Militzer

Introduction

Fe- and Al-bearing perovskite (Pv also known as bridgmanite) and post-perovskite (pPv) are the most abundant minerals in the Earth's lower mantle. A good knowledge of their elastic properties under relevant high-pressure (P) and temperature (T) conditions is of fundamental importance to the understanding of the structure and dynamics of the Earth's interior. However, there are scarce experimental data available on the elastic properties of these systems, and the uncertainty could potentially be huge due to the complexities in physics and technical issues relating to extreme conditions. This necessitates theoretical approaches, which are not limited by the same constraints as experimental approaches and have proven to be a powerful tool for determining the elastic properties of minerals at lower mantle conditions.

Previous reports on the elastic properties of Pv and pPv systems using first-principle calculations are mainly focused on pure $MgSiO_3$ at high-T conditions, or Fe/Al-bearing systems at 0 K. In recent years, there have been several studies on the effects of ferrous and ferric iron on the thermoelastic properties of Pv and pPv. To date, agreement with seismological models of the lower mantle has not yet been reached. One potential reason is that the influence of Al^{3+} has not yet been included, and another could be related to the possible inadequacy of using the quasi-harmonic approximation (QHA) in computing thermoelasticity at high-P and T. There has been one study that used density functional theory molecular dynamics (DFT-MD) to calculate the properties of Pv and pPv enriched with ferrous iron (*Muir and Brodholt*, 2015), however the study only reports values at one pressure.

Method

In this work, we apply DFT-MD to determine the elastic properties of ferrous and ferric iron-bearing Pv and pPv over a wide P and T regime relevant to the Earth's lower mantle. In the case of ferrous iron, only the HS state is considered, whereas for ferric iron, different Fe-Fe or Fe-Al compositions in various possible spin states are also considered.

We first determine the most stable spin configurations at 0 K for ferric iron systems. Based on these structures, thermoelasticity and seismic properties are calculated using the same method as that done in *Stackhouse and Brodholt* (2007).

The moduli and the seismic velocities are fitted as functions of P, T and x using:

$$V(T,P,x) = A_0(x)TP + A_1(x)T + A_2(x)P + A_3(x)$$

where

$$A_i(x) = k_i x + b_i$$

We used the 3rd-order Birch-Murnaghan equation of state (EoS) to analyze the relation between density and P, T and x. We assume linear dependence of ρ_0 and K_0, and independence of K_0', on T. The combination of these results with previous calculations on (Fe,Mg)O, enable us to determine the seismic properties of the mineral assemblage, to compare with the preliminary reference Earth model (PREM) and constrain the mineral composition of the lower mantle. We also study shear wave anisotropic properties resulting from deformation within a deep subducting slab in order to determine the effects of the presence of Fe or Al on the seismic anisotropy.

P, T and Composition Dependence of Seismic Properties

Our calculation shows that both V_p and V_s velocities steadily decrease with increased Fe or Al content. The effects of Fe is shown to be larger for both Pv and pPv. The pPv phase has higher velocities than the Pv phase. At 110 GPa, the differences in V_p and V_s are 0.8 % and 3.2 % respectively. These values further increase to 0.9 % and 3.9 % when x = 5 %, and then to 1.1 % and 4.5 % when x = 10 % for $MgSiO_3$ with Fe^{3+}-Fe^{3+} pairs and Fe^{3+}-Al^{3+} pairs. These changes can similarly be seen in both V_p and V_s but is smaller in V_s by ~0.5 %. The effects of replacing 25 % of Mg by ferrous iron on the velocities are similar to that the effect of Fe-Al pairs on Pv and pPv. At 110 GPa, the density of the pPv phase is higher than that of the Pv phase by 1.5%, 1.5%, 1.4%, and 1.3% for pure $MgSiO_3$, $Mg_{0.75}Fe_{0.25}SiO_3$, Fe^{3+} or Al^{3+} content at x = 6.25 %, and x = 12.5 %, respectively.

Mineralogical Composition of the Lower Mantle

Based on the results above, we examine a mixture of $Mg_{0.95}Fe_{0.05}SiO_3$ (fepv5) : $Mg_{1-x}Fe_xSi_{1-x}Fe_xO_3$ (fefepv) : $Mg_{1-x}Fe_xSi_{1-x}Al_xO_3$ (fealpv) : $Fe_{0.125}Mg_{0.875}O$ (fp12.5) = 34 : 10 : 43 : 13 (volume ratio). This corresponds to a mole ratio of Pv : ferropericlase (fp) = 74 : 26, which is close to the pyrolitic composition. The moduli and density values for fepv5 and fp12.5 are based on *Shukla et al.* (2015) and *Wu et al.* (2013) respectively.

Our calculation shows that, when choosing x = 0.06 in fealpv and x = 0.05 in fefepv, the V_p and V_s velocities match PREM very well from 50 GPa to the top of the D" region (Figure 2.10.1, left), and the agreement in density is also good (difference < 1%).

In this assemblage, the number of cations is remarkably consistent with that of pyrolite. Therefore, we can neglect minor phases such as $CaSiO_3$. We conclude that the major part of the Earth's mantle resembles a pyrolitic model. This is in contrast with the silicon-rich model for the Earth's lower mantle and implies that the extra silicon relative to the CI chondrite may reside in the D" region or the core.

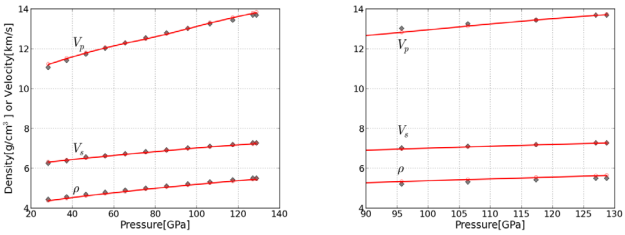

Figure 2.10.1: Comparing density and velocities of mineral assemblages with that of PREM (black diamond points) assuming the geotherm by *Brown and Shankland* (1981).

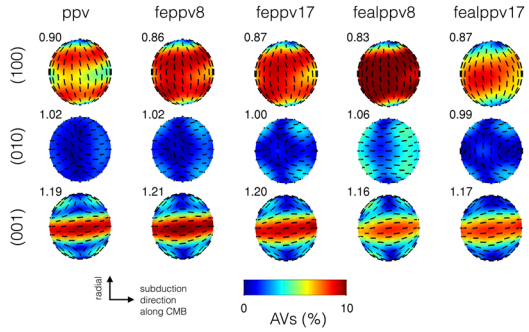

Figure 2.10.2: Shear wave splitting strength (AV_s, in color) and fast axis direction (black bar) shown as a function of seismic wave propagation direction on a sphere for the five different compositional model and three different sets of slips systems., $\xi = V_{SH}^2/V_{SV}^2$ is the value for transverse isotropy. ppv: pure $MgSiO_3$ pPv; feppv8 and feppv17: pPv with Fe^{3+}-Fe^{3+} content at 8% or 17%; fealppv8 and fealppv17: pPv with Fe^{3+}-Al^{3+} content at 8% or 17%.

At higher pressures when Pv can be less stable than pPv, we find that (Figure 2.10.1, right) with higher Al concentration in the pPv phase and less fp but with higher iron content, the velocities of the assemblage fit PREM values well in the high-pressure region (>105 GPa), although ρ is slightly higher (by 2%). This assemblage, if true, indicates that the lower most mantle has the same Mg/Si ratio, but more Fe and Al than the major part of mantle above. This is consistent with the $Fe^{2+} \rightarrow Fe^{3+}$ transformation and the varying of $Fe^{3+}/\Sigma Fe$ in the mantle with depth (*Xu et al.*, 2015).

However, the *Brown and Shankland* (1981) geotherm neglects the steep thermal gradient expected near the core-mantle boundary (CMB), where the temperature could be underestimated by a few hundred to 1500 K. This means that the velocities and the density of the mineral assemblage would overestimated (by about 1 % for V_p, 3 % for V_s, and 1 % for ρ). Including these temperature effects could support an assemblage with the same composition throughout the lower mantle. Also note that in reality (3D), both velocity and density variations are significant in the lowermost mantle and could reflect significant thermal and compositional variations.

Seismic Anisotropy

We forward model the resulting texture and seismic anisotropy in Pv and pPv using the Viscoplastic Self-Consistent (VPSC) method (*Lebensohn and Tomé*, 1993) and deformation information from a typical tracer within a subducting slab (*Cottaar et al.*, 2014). The resulting shear wave splitting and ξ values for pPv are shown in Figure 2.10.2 at 100 GPa and 2500 K. Generally, seismic observations underestimate the actual amplitudes at depth, while our model overestimates them due to assuming that pure dislocation creeps as a deformation mechanism and by excluding the presence of periclase. This leaves the (001) case (Figure 2.10.2) as the only compatible mechanism for seismic transverse isotropy and that is insensitive to the amount of Fe or Al included. None of the models predict strong azimuthal anisotropy, i.e. splitting through the vertical axis.

Acknowledgements

Calculations are performed using NCAR, NERSC, and Advanced Research Computing (U. Leeds) facilities. The authors appreciate UC Berkeley-Earth and Planetary Science colleagues for discussion; and Mingming Li and Allen McNamara for providing deformation information within a subducting slab. SZ and BM are supported by NSF; SS and TL by NERC grant number NE/K006290/1; SC by the Drapers' Company Research Fellowship from Pembroke College, Cambridge, UK.

References

Brown, J.M. and Shankland, T.J. (1981), Thermodynamic parameters in the Earth as determined from seismic profiles. *Geophys. J. R. Astr. Soc.*, 66, 579–596.

Cottaar, S., Li, M., McNamara, A.K., Romanowicz, B., and Wenk, H.-R. (2014), Synthetic seismic anisotropy models within a slab impinging on the core-mantle boundary. *Geophys. J. Int.,* 199 (1), 164–177.

Dziewonski, A.M. and Anderson, D.L. (1981), Preliminary reference Earth model. Phys. *Earth Planet. Inter.,* 25 (4), 297–356.

Lebensohn, R. and Tomé, C. (1993), A self-consistent anisotropic approach for the simulation of plastic deformation and texture development of polycrystals: application to zirconium alloys. *Acta Met. Mater.,* 41, 2611–2624.

Muir, J.M.R. and Brodholt, J.P. (2015), Elastic properties of ferrous bearing $MgSiO_3$ and their relevance to ULVZs. *Geophys. J. Int.,* 201 (1), 496–504.

Shukla, G., Wu, Z., Hsu, H., Floris, A., Cococcioni, M., and Wentzcovitch, R.M. (2015), Thermoelasticity of Fe^{2+}-bearing bridgmanite, *Geophys. Res. Lett.,* 42, doi:10.1002/2014GL062888.

Stackhouse, S. and Brodholt, J.P. (2007), The High-Temperature Elasticity of $MgSiO_3$ Post-Perovskite. In Post-Perovskite: The Last Mantle Phase Transition (eds K. Hirose, J. Brodholt, T. Lay and D. Yuen), *American Geophysical Union*, Washington, D. C.. doi: 10.1029/174GM09, (pp. 99–113).

Wu, Z., Justo, J.F., and Wentzcovitch, R.M. (2013), Elastic Anomalies in a Spin-Crossover System: Ferropericlase at Lower Mantle Conditions. *Phys. Rev. Lett.,* 110 (22), 228501.

Xu, S., Shim, S., and Morgan, D. (2015), Origin of Fe^{3+} in Fe-containing, Al-free mantle silicate perovskite. *Earth Planet. Sci. Lett.,* 409, 319–328.

11 Multi-shock, Ramp and Pre-compression Experiments in the Waste Heat Approximation

Raymond Jeanloz

Introduction

Shock waves are caused by hyper-velocity impact, arguably the most important process associated with the formation and early evolution of planets. Shocks are also used to study materials at the high pressures and temperatures existing deep inside planets, with current laboratory experiments exceeding conditions at the center of giant planets, in our solar system or elsewhere (e.g., pressures exceeding ~ 10 TPa = 100 million atmospheres; Earth's central pressure is under 0.4 TPa). Such pressures exceed the quantum forces stabilizing electron orbitals within atoms (2.3 TPa for n = 1 orbital in the Bohr atom).

Being a finite-amplitude pressure wave, a shock is generally self-steepening. That is, because sound velocity typically increases with compression or pressure, the peak of the pressure wave catches up with the foot of the wave until balanced off by viscous dissipation. The result is a steady-state shock front that is a jump in pressure, density and internal energy. In the limit of small amplitude, a shock is simply a seismic (i.e., elastic) wave. Sufficiently high pressures are achieved, both in nature and in the laboratory, that it is often useful to ignore material strength: the material is treated as though it were a fluid.

Dissipation can limit experiments, in that temperatures become much higher than planetary interior temperatures for shock pressures above about 0.5-1 TPa. High temperatures also limit the density to which materials can be compressed, yet high density is what we want to achieve in order to experimentally measure the chemical-bonding forces between atoms (*Jeanloz et al.,* 2007).

Controlling Shock Heating

The energy change on shock loading consists of an energy of compression plus waste heat due to dissipation in the shock front (Figure 2.11.1) (*Duvall,* 1962). The waste-heat approximation consists of ignoring the difference between the isentrope and Hugoniot; an error of third order in compression, amounting to about 5-20 percent at high compressions (Figure 2.11.2). To the degree reversible, phase transformations do not contribute to waste heat.

One way to reduce the waste heat is to break up the shock into two or more steps, as shown schematically on the right of Figure 2.11.1. A double shock evidently dissipates about 1/4 to 1/3 the energy of a single shock reaching the same final compression (Figure 2.11.3). More detailed analysis shows that the waste heat is minimized by setting the ratio of first to second (final) compression between 0.5 and 0.6, depending on the equation of state (value of s) and final value of η.

Evidently, multiple shocks can further reduce the dissipated energy. Extension beyond the results in Figure 2.11.3 shows that breaking up a single shock into four steps reduces the dissipation by about 90-95 percent. That is, a four-step shock approaches an isentrope, and can be treated as a large-amplitude version of an elastic (seismic) wave. In the limit of multiple shocks, the pressure, density and internal energy ramp up continuously with time.

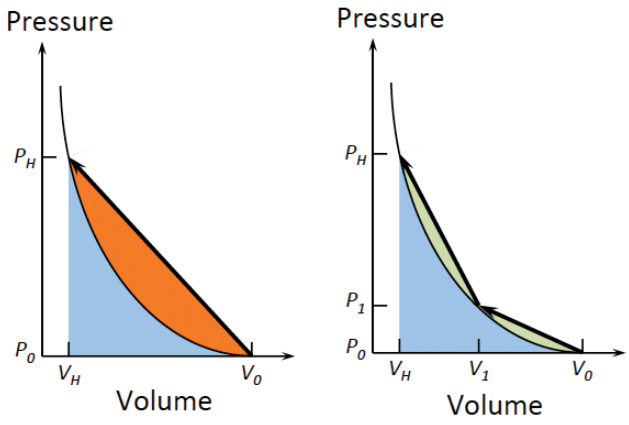

Figure 2.11.1. Schematic of shock-compression path (arrow) from initial (subscript *0*) to final (subscript *H*) volume V and pressure P. The curve is the shock-wave equation of state (Hugoniot), with the area below the arrow(s) giving the change in internal energy on shock compression: an area consisting of the compression energy (*blue*) and waste heat (*orange* and *green* for single- and double-shock experiments, respectively).

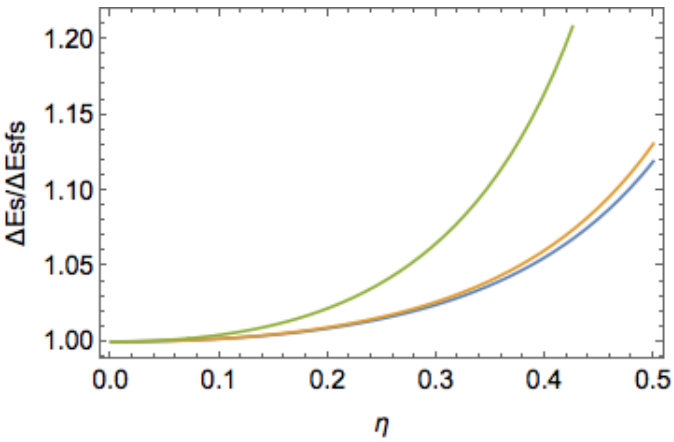

Figure 2.11.2. Ratio of compression energy in the waste heat approximation (isentrope approximated by Hugoniot) to that calculated from an Eulerian finite-strain equation of state, shown as a function of compression $\eta = 1 - V/V_0$ (parameters s = 1.0, 1.25 and 1.50, respectively, for *blue*, *orange* and *green* curves; corresponding to K_0' = 3.0, 4.0 and 5.0,: see *Jeanloz,* 1989).

Such ramp – shock-free – compression can be produced by use of a mechanical impactor (projectile) with graded density, or of a laser pulse that has an appropriate variation of intensity with time. The experiments are challenging because multi-shock and ramp waves are not stable: they evolve toward a sin-

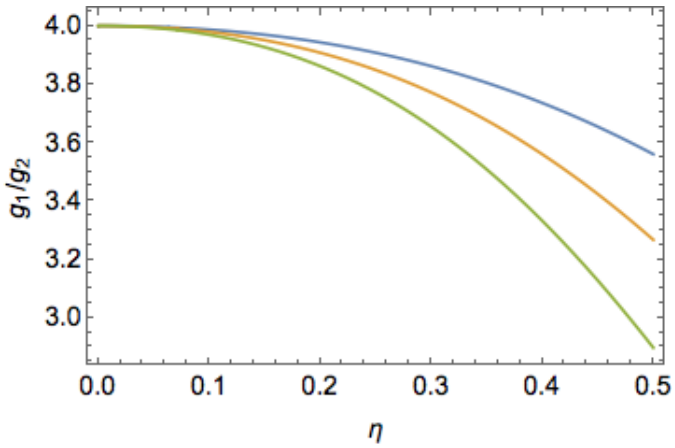

Figure 2.11.3 Ratio of waste heat for single- relative to double-shock compression shown as a function of compression $\eta = 1 - V/V_0$ (parameters s = 1.0, 1.25 and 1.50, respectively, for *blue*, *orange* and *green* curves; corresponding K_0' = 3.0, 4.0 and 5.0). First-shock compression is $\eta/2$.

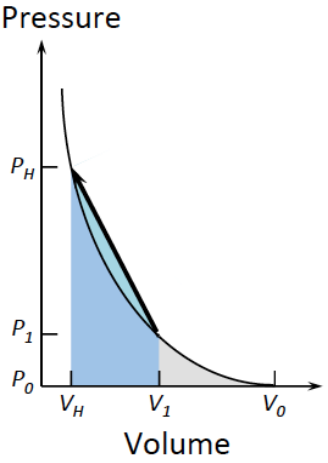

Figure 2.11.4. Schematic of shock compression of a sample pre-compressed to an initial pressure–volume state P_1-V_1, illustrating the reduced waste heat (*teal*) as compared with single-shock experiments.

gle shock discontinuity with time. Nevertheless, laser-driven ramp experiments have been performed to peak pressures of 5 TPa (50 Mbar) (*Smith et al., 2014).*

Another approach is to statically pre-compress a sample to a finite pressure, before dynamically compressing it with a shock or ramp wave (Figure 2.11.4). Laser-driven shock experiments have been successfully performed on samples pre-compressed to 1-20 GPa at room temperature using a diamond cell (*Jeanloz et al.,* 2007; *Brygoo et al.,* 2015).

Pre-compression generates less waste heat than double-shock loading, because there is no dissipation for the compression range between volumes of V_0 and V_1 (grey area in Figure 2.11.4), on the order of percent to tens of percent depending on the initial pre-compression (Figure 2.11.5). Clearly, a combination of ramp or multi-shock compression with static pre-compression leads to yet lower temperatures, hence higher final densities (compressions).

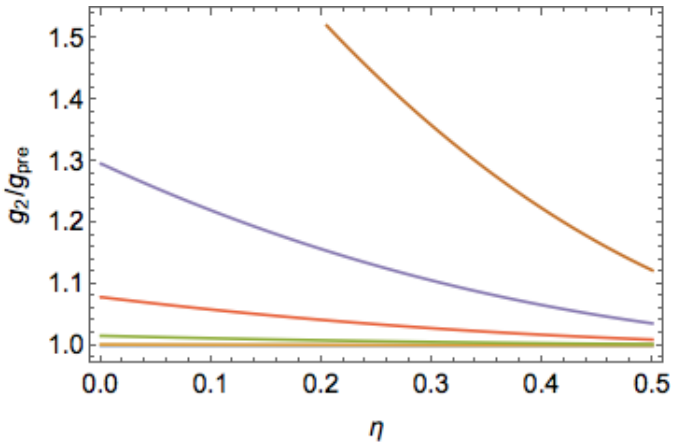

Figure 2.11.5. Ratio of double-shock waste heat to the waste heat from a single shock in a pre-compressed sample: in both cases, the first compression is to a value $\eta_1 = x\,\eta$ (s = 1.25; K_0' = 4.0).

Summary

The waste-heat approximation provides scaling relations for current and future experiments intended to dynamically reproduce the range of pressure–temperature conditions inside planets, and also for characterizing atomic-bonding forces to extreme. Breaking a shock into as few as four steps makes the compression nearly isentropic, with ramp compression generating even less dissipation. Pre-compression is particularly effective in reducing waste heat, and the combination laser-driven ramp (or multi-shock) compression with static pre-compression of samples provides an especially effective means of achieving high densities.

Acknowledgements

This is a summary of research in progress that has been supported by the Department of Energy, University of California, and UC Berkeley's Miller Institute for Basic Research in Science.

References

Brygoo, S., Millot, M., Loubeyre, P., et al. (2015), Analysis of laser shock experiments on precompressed samples using quartz reference and application to warm dense hydrogen and helium: *submitted for publication.*

Duvall, G.E. (1962), Concepts of shock wave propagation: *Bull. Seismological Soc. Am.*, v. 52, p. 869-893.

Jeanloz, R. (1989), Shock-wave equation of state and finite-strain theory: *J. Geophys. Res.*, v. 94, p. 5873-5886.

Jeanloz, R., Celliers, P.M., Collins, G. W., et al. (2007), Achieving high-density states through shock-wave loading of pre-compressed samples: *Proc. National Acad. Sci. (US)*, v. 104, p. 9116-9124.

Smith, R. F., Eggert, J. H., Jeanloz, R., et al. (2014), Ramp compression of diamond to 5 TPa: Experiments taking carbon to the Thomas-Fermi-Dirac regime: *Nature*, v. 511, p. 330-333.

Research Studies:
Earth Structure

University of California
Berkeley
Seismological Laboratory

13 On the presence of broad mantle plumes rooted in the large low shear velocity provinces at the base of the mantle

Scott W. French and Barbara Romanowicz

Introduction

In the 2014 annual report, we presented the construction of the first whole mantle shear velocity model obtained using teleseismic time domain waveforms and the spectral element method (SEM: *e.g., Capdeville et al.*, 2003). This model (SEMUCB_WM1, *French and Romanowicz*, 2014) represents an extension to the lower mantle of two generations of upper mantle models constructed using a similar approach (SEMum, *Lekic et al.*, 2011; SEMum2, *French et al.*, 2013), with the addition of shorter period body waveforms (down to 32 s period). Inspection of the SEMUCB_WM1 model reveals several striking features, which we present here.

"Fat" plumes across most of the lower mantle

The use of accurate forward wavefield computations afforded by the SEM is particularly useful for improving resolution of low velocity structures in the earth's mantle. Indeed, when the wavefield samples such a body, the first arriving waves are not those that went through this structure, but around it (where the velocity is faster). This is the well-known wavefront healing effect. On the other hand, when whole waveforms are considered, the effects of broadband interaction with the low velocity structure, such as diffraction focusing and multipathing, can be observed and can better constrain their shape and the corresponding low velocity anomaly. This is illustrated in Fig. 2.13.1, where we compare the predicted T component wavefield across a hypothetical whole mantle plume to that expected without the presence of the plume. Effects of the plume are particularly clear in the coda of the Sdiff phase, even for a path that does not directly sample the plume, but is removed from it by a distance equivalent to the diameter of the plume.

Inspection of the SEMUCB_WM1 model (*French and Romanowicz*, 2015) shows the presence of ~20 wide, vertically oriented, low velocity conduits, that are rooted in patches of significantly lower than average velocity in D" and extend continuously to at least 1000 km depth, under major hotspots located within the footprint of the two large low shear velocity provinces (LLSVPs) at the base of the mantle (*e.g.,* Fig. 2.13.2). Fig. 2.13.3 shows the improvement in resolution of these features compared with recent models based on secondary observables interpreted in the framework of first order approximations. There are no such fat plumes beneath hotspots that are located outside of the LLSVP's and the only clear plume conduit that does not correspond to a known active hotspot at the surface is located beneath the Indonesian subduction zone, in a location where unusually high 3He/4He ratios have been found among more typical subduction zone volcanism (*Macpherson et al.*, 1998).

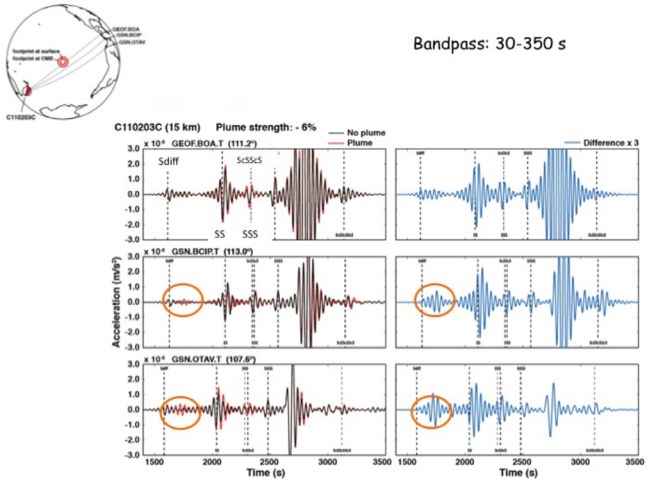

Figure 2.13.1: Left: Comparison of synthetic seismograms obtained with (red) and without (black) a plume. The plume extends from the base of the mantle to the surface and has a diameter of 600 km and a velocity reduction of 6%. Calculations are performed for three paths shown in the upper left hand corner, successively (from top to bottom) further and further away from the plume. Bandpass is 30-350 s. The red ellipses circle portions of the Sdiff coda that are particularly affected by the presence of the plume. Right: here the difference between the seismograms with and without plume are plotted (amplified three times).

The observed plume conduits can be followed continuously up to 1000 km depth. Around that depth, some are deflected horizontally and/or emerge as thinner conduits in the top part of the mantle, others cannot be further tracked, possibly because of lack of resolution. They appear to meander across the upper mantle and merge into the secondary scale convection associated with the motion of the tectonic plates (*e.g., French et al.*, 2013). The very vertical orientation and "fatness" of the plume conduits in the lower mantle suggests that 1) the viscosity of the lower mantle is very high and that most of the upwelling portion of the global circulation is concentrated in these plumes; 2) these plumes may be very old and stable, and/or may be rooted in a layer at the base of the mantle of significant density contrast, with some material entrained into the plumes; 3) in contrast, the viscosity at shallower depth, starting at 1000 km and above, is significantly lower and the site of more vigorous convective motions. This rheological boundary does not seem to correspond to any clear global seismic discontinuity, however it is also observed in tomographic images of subduction zones (*e.g., Fukao and Obayashi*, 2013), also confirmed in SEMUCB_WM1, as some subducted slabs "pond" near the 660 km discontinuity, while others do so around 1000 km depth.

Rheological boundary around 1000 km depth?

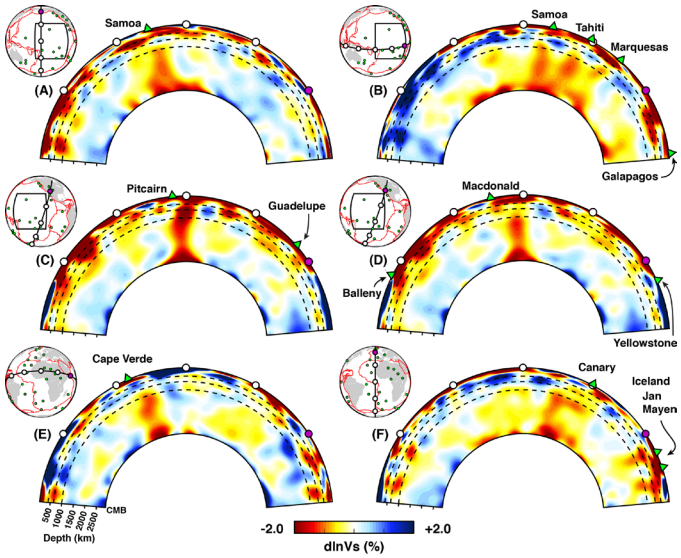

Figure 2.13.2: Depth cross-sections through the SEMUCB_WM1 model (*French and Romanowicz*, 2014), showing fat plumes beneath some prominent hotspots located above or on the border of the Pacific and African LLSVP's (Figure from *French and Romanowicz*, 2015).

ULVZ's at the roots of fat plumes?

There is already evidence for the presence of ultra low velocity zones (ULVZ's) beneath several of the observed "fat plumes": in the vicinity of Hawaii (*Cottaar and Romanowicz*, 2012), near Samoa (*Thorne et al.*, 2013) and possibly near Iceland (*Helmberger et al.*, 1998). Because all the imaged plumes have very low velocity roots in the lower mantle, it is possible that these roots all contain ULVZs. This should guide further work aimed at detecting the presence of ULVZs.

Acknowledgements

We acknowledge support from the National Science Foundation (grants EAR-0738284 and EAR-1417229). SWF acknowledges support from an NSF Graduate Research Fellowship. Computations were performed at the National Energy Research Scientific Computing Center, supported by the Department of Energy Office of Science (Contract No. DE-AC02-05CH11231).

References

Capdeville, Y., Chaljub, E., Vilotte, J.-P., Montagner, J.-P. (2003), Coupling the spectral element method with a modal solution for elastic wave propagation in global earth models, *Geophys. J. Int.,* 152, 34–67.

Cottaar, S. and Romanowicz, B. (2012), An unusually large ULVZ at the base of the mantle near Hawaii, Earth. Planet. Sci. Lett. 355-356, 213-222.

French, S., Lekic, V., Romanowicz, B., (2013), Waveform Tomography Reveals Channeled Flow at the Base of the Oceanic Asthenosphere, *Science,* 342, 227–230.

French, S. and Romanowicz, B., (2014), Whole mantle radially anisotropic shear-velocity structure from spectral-element waveform tomography, *Geophys. J. Int.*, 199, 1303-1327.

French, S. W. and B. Romanowicz (2015), Fat plumes rooted at the base of the mantle beneath major hotspots, *Nature*, in press.

Fukao, Y., Obayashi, M. (2013), Subducted slabs stagnant above, penetrating through, and trapped below the 660 km discontinuity, *J. Geophys. Res.*, 118(11), 5920–5938.

Helmberger, D. V., Wen, L. and Ding, X. (1998), Seismic evidence that the source of the Iceland hotspot lies at the core-mantle boundary, *Nature* 396, 251-255.

Lekic, V. and Romanowicz, B. (2011), Inferring upper-mantle structure by full waveform tomography with the spectral element method, *Geophys. J. Int.*, 185, 799–831.

Macpherson, C. G., Hilton, D. R., Sinton, J. M., Poreda, R. J. and Craig, H. (1998), High 3He/4He ratios in the Manus backarc basin: implications for mantle mixing and the origin of plumes in the western Pacific Ocean, *Geology,* 26, 1007-1010.

Thorne, M. S., Garnero, E. J., Jahnke, G., Igel, H. and McNamara, A. (2013), Mega ultra low velocity zone and mantle flow, *Earth Planet. Sci. Lett.,* 364, 59-67.

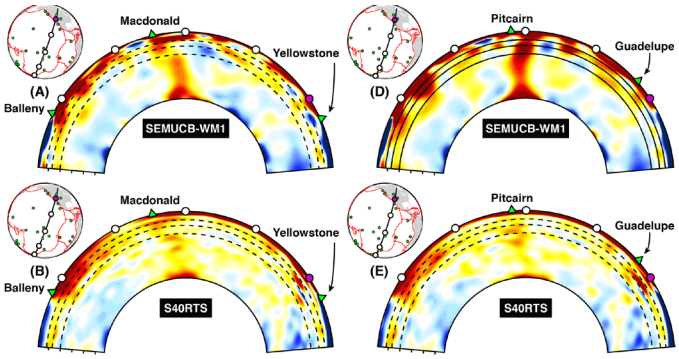

Figure 2.13.3: Comparison of depth cross sections passing through Macdonald (left) and Pitcairn (right) in SEMUCB_WM1 (top) and S40RTS (Bottom, *Ritsema et al.*, 2011). This comparison shows that the two models agree on the long wavelength structure, but the broad plume conduits are clearly better defined in the new, full waveform SEM-based model.

14 Seismic Constraints on the Nature of the Iceland Hotspot

Kaiqing Yuan and Barbara Romanowicz

Introduction

Iceland, a well-known active hotspot, is located on the mid-Atlantic ridge and is the focus of many studies that attempts to clarify the interaction between mantle upwelling and ocean ridge spreading, thus address fundamental questions concerning the nature of mantle dynamics. There is a long-standing debate on whether the Iceland hotspot originates at shallow depths or is caused by a deep mantle plume. Seismic tomography models show that there is a strong low-velocity anomaly beneath Iceland that extends to 660 km (*Ritsema and Allen*, 2003) and possibly deeper (*Rickers et al.*, 2013). However, geochemical studies on the volcanic rocks from Iceland find a high $^{3}He/^{4}He$ ratio that cannot be explained by upper mantle processes. This suggests a lower mantle plume origin (*Foulger and Pearson*, 2001).

The lowermost part of mantle, known as the D" region, is both a thermal and chemical boundary layer between the solid, silicate mantle and fluid, iron outer core. Many studies have shown the presence of Ultra Low Velocity Zones (ULVZ) in the D" layer. A ULVZ is often characterized by a large S-wave velocity reduction (-10 % to -30 %) and a thickness of ~5-30 km. The lateral extension of the ULVZs is not well constrained. However, a recent study shows an unusually large ULVZ beneath Hawaii. This may indicate the root of a long-lived, stable plume related to the Hawaii hotspot (*Cottaar and Romanowicz*, 2012).

A recently developed global tomographic model of the earth's mantle (*French and Romanowicz*, 2014) confirms the presence of wide plumes rooted at the base of the mantle, extending across most of the lower mantle in the vicinity of Hawaii and Iceland, as well as many other hotspots (*French and Romanowicz*, 2015). In this study, we aim to explore the S-wave velocity structure at the base of the mantle near Iceland, in order to better constrain the extent of the ULVZ that has previously been documented (*Helmberger et al.*, 1998) and may reside inside the root of the Iceland plume.

Data and Method

In order to directly detect S-wave velocity variations near Core-Mantle Boundary (CMB), we use the S_{diff} phase, which is the S-wave diffracted along the CMB. We also look at the S, SKS and SKKS phases as reference phases to eliminate possible causes of waveform anomalies elsewhere in the mantle. Here we provide an example; a M_w6.8 event that occurred in Pakistan on 09/28/2013 (Table 2.14.1), and was well-recorded by the USArray in North America.

Figure 2.14.1 shows the event location, station distribution and ray geometry. The broadband seismic waveform data is obtained from the IRIS Date Management Center (DMC) via the Wilber 3 service. We remove the instrument response and rotated the horizontal components to radial and tangential directions, the filter the data in different passbands.

To simulate the waveform down to periods ~10 s requires very expensive computations. In order to speed up the calculation while keeping the computation accurate in the region of interest, ie. the D" region, we use the "sandwiched" version of the coupled spectral element method (Sandwich - CSEM) (*Capdeville et al.*, 2003). In this method, the earth is vertically divided into three parts. The core and most of the mantle are treated as 1D, and for that we use a mode solution. In the D" region, which we are trying to model, the wavefield is computed in 3D with the spectral element method.

Inside the D" region, we use the recently published whole mantle S-wave velocity model SEMUCB-WM1 (*French and Romanowicz*, 2014) as a background velocity model. In order to fit the data, we choose to use a forward modeling method, ie. impose ULVZ models on the background velocity and then calculate the waveform with Sandwich CSEM. We will then systematically test the effects of the ULVZ location, height, size, and velocity reductions, and utilize this information to guide the model selection.

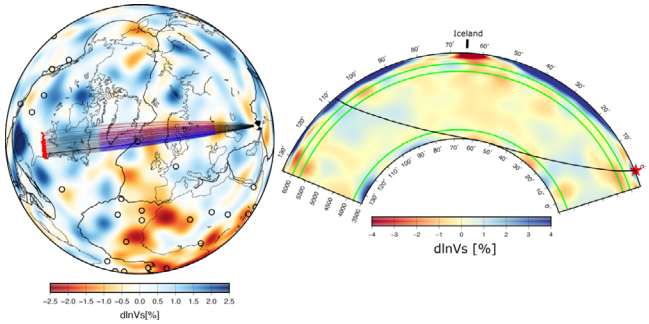

Figure 2.14.1: Map and cross-section showing the spatial distribution of event, stations, and S_{diff} wave paths to the USArray. Left) The earthquake is marked by the black and white beach-ball. Stations are shown by red dots, corresponding to an epicentral distance of 108°-110°. Colored segments correspond to different azimuths, and also indicate the portion of the S or S_{diff} path that penetrates into the D" region (here 300 km above the CMB). Black lines show the ray paths in the rest of mantle. Background color is the global S-wave velocity model SEMUCB-WM1 (*French and Romanowicz*, 2014) at 2800 km. Right) Black lines shows the SH_{diff} ray path at distance of 108°. Event is marked by a red star. Three green lines from top to bottom are at 410, 660 and 2590 km depth, respectively. This cross-section is plotted along the great circle plane at azimuth, 332°, which passes through Iceland.

Event	Time	Long.	Lat.	Depth	Mag.
Pakistan	09/28/2013	65.505E	27.183N	12km	Mw6.8

Table 2.14.1: Earthquake used in the example shown in Figures 2.14.1 and 2.14.2.

Results and Discussion

Figure 2.14.2 shows the SH component of the S_{diff}, filtered between 10-20 s, a bandpass in which waveform anom-

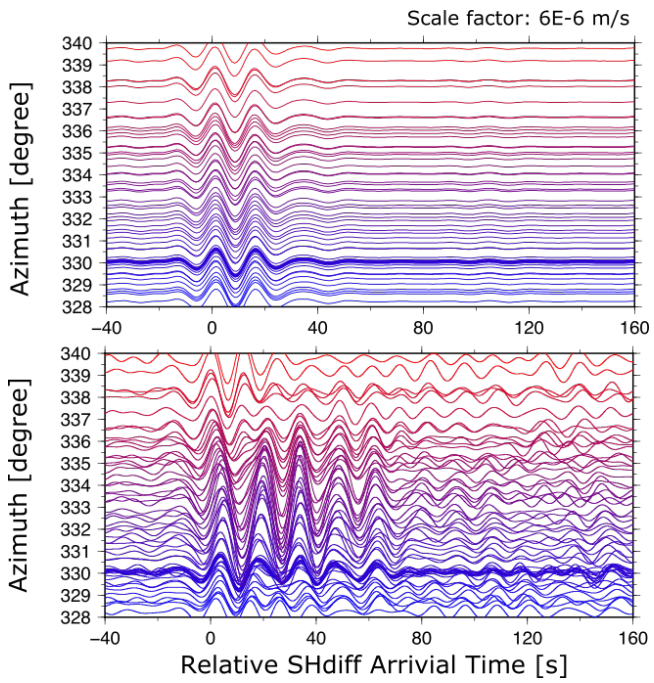

Figure 2.14.2: SH_{diff} waveforms bandpass filtered between 10 and 20 s, Top) 1D synthetics, Bottom) real data. Waveforms are aligned at predicted S_{diff} arrival time (calculated with TauP) and sorted by azimuth. Colors represents different ray azimuths, with the same convention as in Figure 2.14.1, left. Amplitude in both panels indicates velocity, and the scale factor is 6×10^{-6} ms^{-1}.

alies in the coda of the S_{diff} are particularly clear, compared to 1D synthetics. The observed waveforms (Figure 2.14.2, bottom) exhibit far more complexity than the 1D synthetics (Figure 2.14.2, top), in particular an azimuthal dependent travel time delay (~7 - 8 s) and a complex S_{diff} coda. Such complexities cannot be explained by current tomographic models, not even by SEMUCB_WM1. According to Figure 2.14.1, left, we find that these waveform anomalies correspond mainly to paths that sample the lowermost mantle, near Iceland. This may indicate a S-wave velocity anomaly in that region. Although we cannot yet rule contributing effects from the mantle, looking at other mantle phases, ie. S, SKS, SKKS, will provide us more constraints on the interpretation of these observations. Our future work will focus on including new waveforms that sample the lowermost mantle under Iceland from other directions, and compute an ensemble of synthetics based on different 3D models. Thus, would help us confirm the presence of the Iceland ULVZ, and characterize it further.

Acknowledgements

This study is supported by the NSF CSEDI Grants EAR 1067513 and 1464014. The broadband waveform data is downloaded from IRIS (www.iris.edu). The 3D simulation CSEM code is provided by Yann Capdeville.

References

Capdeville, Y., A. To, B. Romanowicz, (2003), Coupling spectral elements and modes in a spherical earth: an extension to the sandwich case, *Geophys. J. Int.*, 154 (1), 44-57.

Cottaar, S. and B. Romanowicz, (2012), An unusually large ULVZ at the base of the mantle near Hawaii, *Earth and Planet. Sci Lett.*, 355-356.

Foulger, G.R. and D.G. Pearson, (2001), Is Iceland underlain by a plume in the lower mantle? Seismology and helium isotopes, *Geophys. J. Int.*, 145, F1-F2.

French, S. W. and B. Romanowicz, (2014), Whole mantle radially anisotropic shear-velocity structure from spectral-element waveform tomography, *Geophys. J. Int.*, 199, 1303-1327.

French, S. W. and B. Romanowicz, (2015), Fat plumes rooted at the base of the mantle beneath major hotspots, *Nature*, in press.

Helmberger, D. V., L. Wen, and X. Ding, (1998), Seismic evidence that the source of the Iceland hotspot lies at the core-mantle boundary, *Nature*, 251-254.

Ritsema, J. and R. M. Allen, (2003), The Elusive Mantle Plume, *Earth and Planet. Sci. Lett.*, 207, 1-12.

Rickers, F., A. Fichtner, and J. Trampert, (2013), The Iceland-Jan Mayen plume system and its impact on the mantle dynamics in the North Atlantic region: Evidence from full-waveform inversion, *Earth and Planet. Sci. Lett.*, 367, 39-51.

15 Probing the Anisotropic Structure of North America's Upper Mantle Combining Long and Short Period Seismic Constraints

Marco Calò, Thomas Bodin, Barbara Romanowicz

Introduction

Different approaches have been used to image crust and lithospheric structure at continental scales, and particularly North America (NA). At long periods (20 - 250 s), surface wave tomography provides resolution of volumetric heterogeneity of ~500 km laterally and ~50 km in depth, down to ~300 km (*French and Romanowicz,* 2014*, and references therein*). However, surface waves cannot uniquely resolve sharp interfaces, such as the Moho, the Lithosphere-Asthenosphere Boundary (LAB) or the possible presence of Mid-Lithospheric Discontinuities (MLD's). In order to image such discontinuities, methods based on the analysis of converted phases at crust and upper mantle interfaces (e.g. the receiver functions) have been developed. Since surface wave data and receiver functions provide complementary constraints on the lithosphere, several studies showed the possibility to combine them to obtain more robust models of the crust and uppermost mantle (e.g. *Lawrence and Wiens,* 2004). In recent years, forward modeling approaches using a Monte Carlo Markov Chain (MCMC) framework have been developed for this purpose, although they are time consuming and are a computational burden.

Here we propose a transdimensional MCMC technique (*Green,* 2003) that allows us to combine fundamental mode Love and Rayleigh wave dispersion curves and P-to-S converted phase data to retrieve 1D radially anisotropic layered models beneath a set of stations in NA. Our approach has several original aspects:

1. We consider both Love and Rayleigh wave dispersion data, allowing us to include radial anisotropy - the presence of which is prevalent in the uppermost 200 km of the mantle (e.g. *Dziewonski and Anderson,* 1981) - in our inversion.
2. Instead of a standard RF methodology, our body wave dataset derives directly from seismic waveforms through a cross-convolution method (*Bodin et al.,* 2014), thus avoiding instability issues arising from deconvolution and importantly, allowing us to take into account crustal multiples without ambiguity.
3. We use a transdimensional MCMC approach in which the number of isotropic and anisotropic layers are treated as unknowns, allowing us to obtain models compatible with the data, with the least number of parameters (*Bodin et al,* 2015).

Because the proposed forward modeling approach is computationally much heavier than the standard RF migration, we have chosen 30 stations that may be representative of the lateral variations of structure in NA, at least to first order. We then started from a recently developed high-resolution global radially anisotropic shear velocity model of the mantle (SEMUCB_WM1, *French and Romanowicz,* 2014), to which we have applied a cluster analysis method (e.g. *Lekic and Romanowicz,* 2011), in order to objectively define three distinct regions in which the shear velocity variations with depth are similar, across the continent. We then pick about 10 stations in each region for which high quality data is available and performed our analysis at these stations.

The patterns observed by applying the 1D stochastic joint inversion of long period dispersion curves and scattered phase data, provide some insights on the lithospheric structure of NA (*Calò et al., in preparation*).

Regionalization of the North American Continent

We applied k-means cluster analysis to the SEMUCB_WM1 global radially anisotropic shear velocity model (*French and Romanowicz,* 2014) in the depth range 50-350km, in order to separate the North American region into three main provinces (Figure 2.15.1; Oceanic-P1, Cratonic-P2, and Transition-P3 zone).

The mean standard deviation of the velocity profiles in each province is 0.05 kms^{-1} and the largest euclidean norm between the average 1D profile of each region and the 1D models does not exceed 0.15 kms^{-1}. These values suggest that each macro-region encloses 1D profiles that are very similar in the depth range considered, and that a separation of the NA into three regions by cluster analysis well reflects the main units of the lithosphere across the continent, to the first order.

Construction of 1D Models

We calculated 1D V_s and radial anisotropy ($\xi=(V_{sh}/V_{sv})^2$) profiles and posterior noise estimation at 30 stations deployed in the NA continent, using an updated version of the transdimensional Markov-chain algorithm (*Bodin et al.*, 2014). In this version we jointly invert three datasets:

1. Rayleigh and Love phase velocity dispersion curves from 25 s to 250 s, extracted from the global model of *Ekström et al.,* (2011).
2. Rayleigh and Love group velocity dispersion curves from 16 s to 150 s, extracted from the global model of *Shapiro et al.,* (2002).
3. Averaged seismograms for calculating receiver functions using the cross-convolution method (*Bodin et al.,* 2014).

Synthetic tests reproducing the real data conditions show that both data and inversion method are suitable to properly estimate posterior errors, absolute velocity values and sharp discontinuities, down to 300 km.

Figure 2.15.2 shows an example 1D profile of Vsv and ξ for a station in each province. The stations belonging to each region

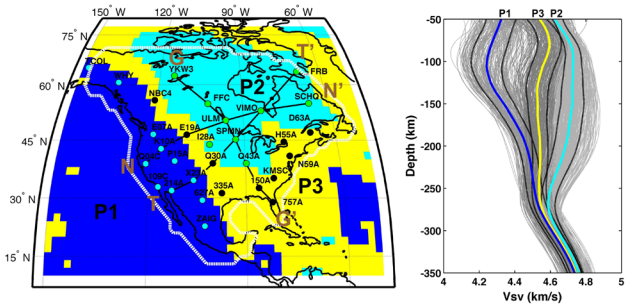

Figure 2.15.1: Left) Geographic extents of the 3 regions (P1, P2 and P3), identified using k-means clustering applied to the model SEMUMCB-WM1. The position and name of the stations used to calculate the 1D probabilistic profiles are indicated. Right) 1D V_{sv} velocity profiles of SEMUMCB-WM1 enclosed in the study region. The different colors indicate averages of vertical profiles in each of the regions. Black dashed lines are the standard deviations of the profiles of each province (P1, P2, P3).

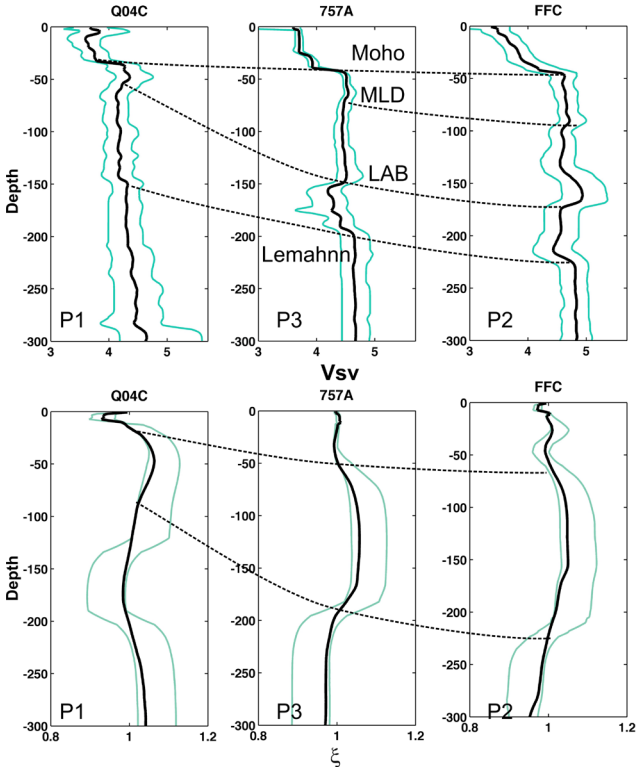

Figure 2.15.2: Examples of 1D profiles of Vsv (top) and ξ (bottom) calculated at three stations using experimental data. Each station is located in a macro-region (P1, P2, P3) in which the NA continent has been divided into (Figure 2.15.1). Dashed-lines laterally connect the main discontinuities observed on the profiles.

show similar features; therefore the patterns shown in figure 2.15.2 can be considered representative of each province. In the V_{sv} profiles, we observe the gradual deepening of the Moho in the sequence P1-P3-P2 (ocean-transition-craton). Profiles of P2 and P3 generally show the presence of a MLD at depth of 80-130 km, as well as a LAB that reaches 200-250 km depths. The LAB in stations located in P1 is generally much shallower (60-120 km). A sudden increase of velocity at depth ranging from 150 km to 300 km in all the profiles is interpreted as the expression of the Lehmann discontinuity. The corresponding distributions of ξ show that the NA continent is dominated by a gradual deepening of the region of $\xi > 1$, from 80-150 km beneath the province P1, to 222-250 km beneath P2 and P3.

Acknowledgements

This project is funded by the "UC Lab-fee" collaboration program (UCOP grant 12-LR-236345) and is in collaboration with M. Maceira and C. Larmat at Los Alamos National Laboratory. Thomas Bodin wishes to acknowledge support from the Miller Institute for Basic Research at the University of California, Berkeley

References

Bodin, T., Capdeville Y, Romanowicz B, and Montagner J.P. (2015), Interpreting Radial Anisotropy in Global and Regional Tomographic Models, 2014. Book *Chapter. The Earth's heterogeneous mantle. A Khan, F Deschamps & K Kawai (eds), Springer International Publishing.* doi: 10.1007/978-3-319-15627-9.

Bodin, T., Yuan, H., and Romanowicz B. (2014), Inversion of receiver functions without deconvolution—application to the Indian craton. *Geophys. J. Int*. doi:10.1093/gji/ggt431.

Dziewonski, A. M., Anderson D. L. (1981), Preliminary reference Earth model. *Physics of the Earth and Planetary Interiors,* 25, S.297–356.

French, S., and Romanowicz, B. (2014) Whole-mantle radially anisotropic shear velocity structure from spectral-element waveform tomography, *Geophys. J. Int.*, doi: 10.1093/gji/ggu334 .

Green, P. J. (2003) Trans-dimensional Markov chain Monte Carlo, *OUP, Oxford.*

Ekström, G. (2011) A global model of Love and Rayleigh surface wave dispersion and anisotropy, 25–250 s. *Geophys. J. Int*, 187: 1668–1686. doi: 10.1111/j.1365-246X.2011.05225.

Lekic, V. and Romanowicz B. (2011) Tectonic regionalization without a priori information: a clustering analysis of upper mantle tomography, *Earth Planet. Sci. Lett.*, 308, 151-160.

Shapiro, N.M., and Ritzwoller M.H. (2002) Monte-Carlo inversion for a global shear velocity model of the crust and upper mantle, *Geophys. J. Int*, 151, 1, 88-105.

Lawrence, J.F, and Weins D.A. (2004) Combined Receiver-Function and Surface Wave Phase-Velocity Inversion Using a Niching Genetic Algorithm: Application to Patagonia. *Bulletin of the Seismological Society of America*, 4, 3, 977–98.

16 Imaging Anisotropic Layering with Bayesian Inversion of Multiple Data Types

Thomas Bodin, Julie Leiva, and Barbara Romanowicz

Introduction

Seismic anisotropy in the crust and upper mantle can be produced by multiple physical processes at different spatial scales. In the mantle, plastic deformation of olivine aggregates results in a crystallographic preferential orientation (CPO) of minerals, and produces large scale seismic anisotropy that can be observed seismologically. These observations are usually related to the strain field, and interpreted in terms of either present day flow, or frozen flow from the geological past. Furthermore, the spatial distribution of cracks, fluid inclusions, or seismic discontinuities can induce apparent anisotropy, called Shape-Preferred Orientation (SPO). In this way, anisotropic properties of rocks are closely related to their geological history and present configuration and hence, reveal essential information about the Earth's structure and dynamics.

Azimuthal anisotropy in the crust and upper mantle can be observed from different seismic measurements, sampling the Earth at different scales: surface wave observations, core-refracted shear wave (SKS) splitting measurements, and receiver functions. These three different data types are characterized by different sensitivities to structure, they are modeled with different approximations of the wave equation, and associated with different uncertainties. A well-known problem in seismology is that they often provide incompatible earth models, leading to contradictory interpretations. In order to improve resolution, several studies have proposed to combine these different types of observations with joint inversion algorithms. However, several challenges remain in anisotropic imaging:

1. To our knowledge, azimuthal variations of surface wave dispersion measurements have never been inverted jointly with receiver functions.

2. It is difficult to jointly invert different data types, as inverted models strongly depend on the choice of parameters used to weigh the relative contribution of each datasets in the inversion.

In this work, we address these issues with a method for 1D inversion under a seismic station. We jointly invert dispersion curves with their azimuthal variations, together with converted body waves (receiver functions), and SKS data.

Method

As shown in Figure 2.16.1, our model is parameterized in terms of a stack of layers with constant seismic velocity. We use a trans-dimensional formalism, where the number of unknowns is variable (*Bodin et al.*, 2014, 2015). Following the principle of simplicity, the goal is to explain our datasets with the least number of free parameters. Each layer can be either isotropic (and described solely by its shear wave velocity Vs), or azimuthally anisotropic (and described by three unknown parameters: Vs, the level of azimuthal anisotropy δVs, and the direction of the horizontal fast axis relative to the North Ψfast).

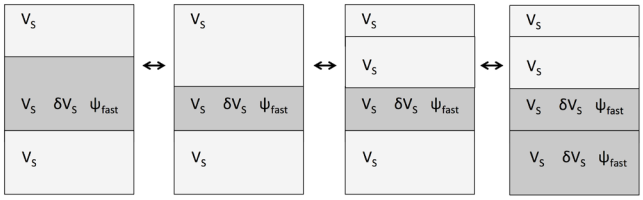

Figure 2.16.1: The 1D model is parameterized with a variable number of layers, each of which can be either isotropic and described by one parameter (light gray), or azimuthally anisotropic and described by three parameters (dark gray). As our Monte Carlo parameter search algorithm samples the space of possible models, different types of jumps are used to explore different geometries (change the depth of a discontinuity, add/remove an isotropic layer, add/remove anisotropy to an existing layer).

The thickness of layers is also variable, and the last layer is a half-space.

The number of layers, k, as well as the number of anisotropic layers, l<k, are free parameters in the inversion (See Figure 2.16.1). It is clear that observations can always be better explained with more model parameters (with l and k large). However, in a Bayesian framework, overly complex models with a large number of parameters have a lower probability and are naturally penalized. Between a simple and a complex model that fit the data equally well, the simple one will be preferred. In this way, anisotropy will only be included into the model if required by the data.

We use a forward modeling approach, where at each step of the Monte Carlo sampler, a new model, as defined in Figure 2.16.1, is to be tested, and data predicted for this model are compared to actual measurements. For Rayleigh waves, dispersion curves and their azimuthal variations are computed with a normal mode formalism in a spherical Earth. For body waves, *i.e.* receiver functions and SKS waveforms, the impulse response of a model to an incoming planar wave is computed with a reflectivity propagator matrix method.

We cast our inverse problem in a Bayesian framework, where information on model parameters is represented in probabilistic terms. The goal is to generate a large ensemble of layered models, the distribution of which approximates the posterior function, which here is defined in a variable dimensional space, and can be sampled with the reversible-jump Markov chain Monte Carlo (rj-McMC) sampler.

This `ensemble solution' contains many models with variable parameterizations. Here we represent the posterior probability of the shear wave velocity at a given depth simply by plotting the histogram of the values selected for the ensemble solution.

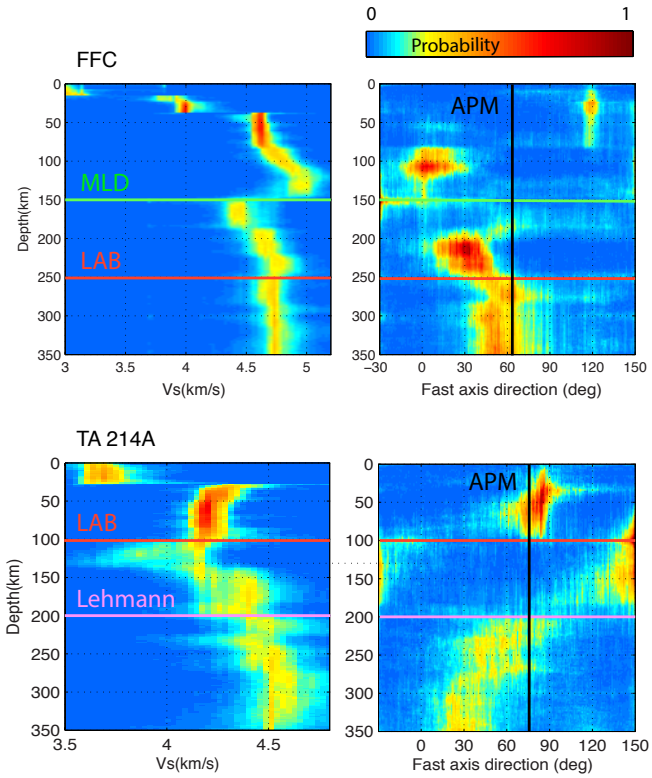

Figure 2.16.2: Results for Joint inversion of surface waves, SKS waveforms and receiver functions for station FFC in the North American Craton (upper panels) and TA-214A in the Southern Basin and Range (lower panels).

Application to Two Different Tectonic Regions in North America

We apply this method to seismic observations recorded at two different locations in north America. First, we invert data from station FFC (N54 W102), which is an old, reliable, and well studied station located at the core of the Slave Craton. Since a large number of studies have already been published about the structure under this station, we view this as an opportunity to test and validate the proposed scheme. In a second step, we invert seismic data recorded at station TA-214A, of the US transportable array, which is a much noisier, recent, and less studied station, located in the southwest US, close to a diffuse plate boundary, where we expect more complex 3D structure due to recent tectonic activity. Here, 3D effects in our data won't be able to be accounted for by our 1D model and hence, will be treated as data errors by our Bayesian scheme.

Top panels in Figure 2.16.2 show results for FFC. A sharp negative velocity jump appears at 150 km, which we interpret as a mid-lithospheric discontinuity (MLD), the physical cause and nature of which remain elusive, but which may be related to a low-velocity zone within the lithosphere. The base of the lithosphere at 250 km is given by the change in direction of anisotropy. Below 250 km, the direction is aligned with the absolute motion of the North-American plate. Overall, results for FFC are compatible with previous studies.

Results for station TA-214A are shown in the bottom panels of Figure 2.16.2. A clear negative discontinuity in Vs is visible at 100 km with a positive jump at 150 km, thus producing a low velocity zone of 50 km that could be interpreted as the asthenosphere. In this case, the shallow LAB at 100 km is compatible with a number of Sp receiver functions studies in the region. Here, the sharp LAB discontinuity cannot be solely explained with a thermal gradient, and hence suggests the presence of partial melt in the asthenosphere in this region. The vertical distribution of fast axis direction clearly shows three distinct domains:

1. The lithospheric extension of the basin and ranges in the east-west direction (90 deg) is clearly visible in the first 100 km, also observed in surface wave or full waveform tomographic models. This E-W direction of fast axis is close to being perpendicular to the north America-Pacific plate boundary, and corresponds to the direction of opening of the gulf of California.

2. There is a sharp change of direction of anisotropy at 100 km, which confirms the interpretation of the negative discontinuity as the LAB. A distinct layer between 100-150 km is clearly visible with a direction of 150 deg, compatible with shear wave splitting observations obtained in this region.

3. The jump at 180-200 km in the direction of anisotropy to about 60 deg seems associated with a positive step in the velocity, and could be the "Lehmann" discontinuity.

References

Bodin, T., Capdeville, Y., Romanowicz, B., Montagner, J.P. (2015), Interpreting Radial Anisotropy in Global and Regional Tomographic Models. In the Earth's heterogeneous mantle. A Khan, F Deschamps and K Kawai(eds), *Springer International Publishing* DOI: 10.1007/978-3-319-15627-9.

T Bodin, Yuan, H , and Romanowicz, B. (2014), Inversion of receiver functions without deconvolution, *Geophysical Journal International*, 196 (2), 1025–1033.

17 Wavefield inversion of surface waves using Particle Swarm Optimization (PSO) for delineating seismic structure in saline permafrost: A case study from the Barrow peninsula, AK

Shan Dou, Jonathan Ajo-Franklin, Douglas Dreger, John Peterson, Craig Ulrich, Baptiste Dafflon, Susan Hubbard

Summary

Seismic investigations of permafrost are essential in cold-region environments, with applications to static corrections for seismic exploration and site characterization for infrastructure development. However, since uniform layering of increasing velocities rarely exist in permafrost, commonly used refraction and reflection methods are sometimes difficult to apply.

Surface-wave methods are advantageous because their applicability does not require regular velocity gradients. Nevertheless, permafrost poses distinct challenges to surface wave inversion: the irregular velocity variations in permafrost, combined with the marked velocity contrasts between frozen and unfrozen ground, often yield complicated dispersion spectra in which higher-order and leaky modes are dominant. Owing to the difficulties in retrieving and identifying dispersion curves from such spectra, the conventional, dispersion-curved-based inversion methods become inapplicable. Instead, full-wavefield approaches are preferred.

In this study, we use the full-wavefield surface wave inversion method that was previously described in Dou and Ajo-Franklin (2014) to invert for near-surface velocity structures of our permafrost field site at Barrow, Alaska. By using a full-wavefield, dispersion-spectrum-based objective function, the inversion becomes much less susceptible to cycle-skipping problems that often hinder waveform inversions. We also make use of an "intelligent" search algorithm, particle swarm optimization (PSO), to search for the global minima of the objective function. Although dispersion spectra, rather than waveforms, were used in the inversion, the inverted velocity models are able to provide good fits for both the spectra and the waveforms, proving the effectiveness of the method.

Our inversion results reveal that despite the high Arctic climate at Barrow, permafrost at our field site is far from being frozen solid. Underneath ~1–5.7 m of high-velocity, frozen layer is a pronounced low-velocity, unfrozen or partially frozen layer (thicknesses range from 8 m to over 34 m) that is persistently present along our 4300 m-long survey transect across the Barrow Peninsula. This layer is likely saline, in which the dissolved salts lower the freezing point of the pore water, hence preventing further freezing even when the corresponding ground temperatures are as low as -6 to -9 °C year around. Being water-rich and highly sensitive to thermal disturbance, this saline layer may degrade with accelerated rate in a warming climate. Therefore, its future impact should be estimated for climate modeling efforts and engineering practices.

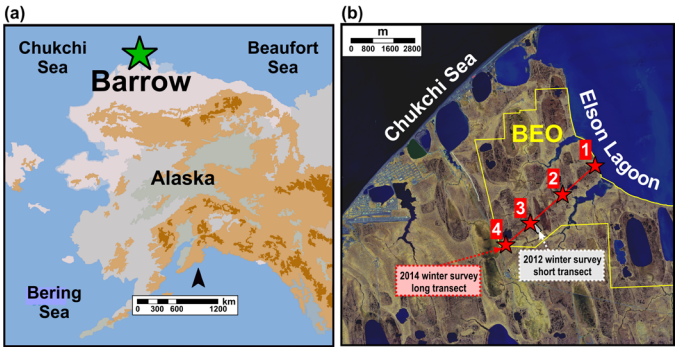

Figure 2.17.1: Maps of the study area near Barrow, Alaska: (a) the Barrow area within Alaska (green star). (b) The 4300 m-long survey transect (red line) on the Barrow peninsula. Red stars (1–4) denote the locations of the multichannel surface wave survey.

Field Site and Seismic Acquisition Layout

The Barrow Peninsula, located at the northern extremity of the Arctic Coastal Plain in Alaska, is underlain by continuous permafrost to estimated depths of more than 300 m. The sediments are primarily of marine origin.

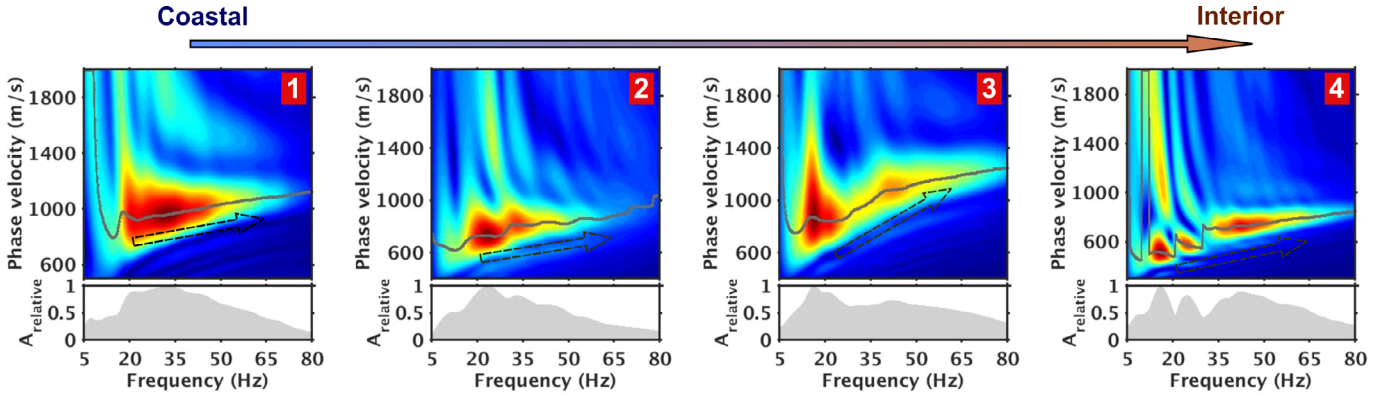

Figure 2.17.2: Dispersion spectra of the multichannel surface wave data. Red arrows on the left denote arrivals that signal the bottom of the low-velocity zones.

In early May of 2014, we conducted an active multichannel surface-wave survey (sledge hammer source) along a 4300 m (2.7 mi) northeast-southwest trending transect that extended from the coastal to the interior areas of the peninsula. We acquired surface-wave gathers—each with a maximum offset of 84 m and receiver spacing of 1 m—from four nearly equidistantly distributed subsections of the transect (Figure 2.17.1).

Dispersion Characteristics of The Field Data

Dispersion spectra of all the surface wave gathers (Figure 2.17.2) show dominant higher-order and leaky modes, as well as inversely dispersive trends, which signify the presence of velocity reversal and strong velocity contrast.

Full-wavefield Inversion: Objective function

Our objective function computes the misfit (root-mean-square deviation) between the observed and the synthetic dispersion spectra. The synthetic wavefield is generated with the wavenumber integration method (Herrmann, 2004).

Particle Swarm Optimization (PSO)

PSO (Kennedy and Eberhart, 1995) is a population based stochastic optimization technique, inspired by social behaviors of bird flocking or fish schooling. PSO is easy to implement, readily parallelizable, and requires very few parameter adjustments.

Parameterization

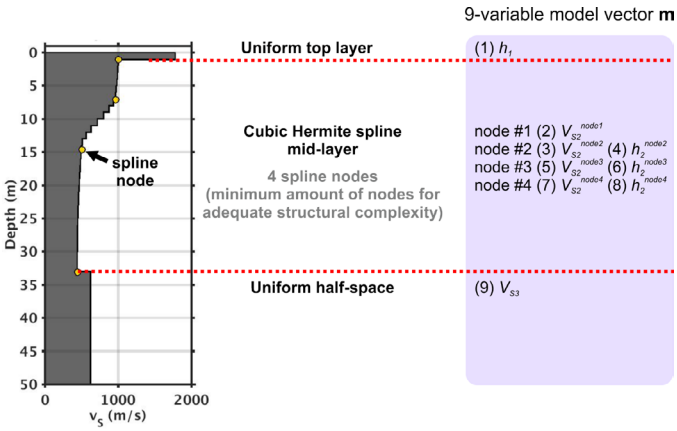

Figure 2.17.3: Schematics of the 9-variable layer model parameterization.

Results and Interpretation

Figure 2.17.4 shows the inverted velocity profiles. Note that as we move from the coastal to the interior sites, neither the depth extent nor the velocities of the low-velocity layers exhibit systematic trends. Therefore, the saline layer is less likely to be caused by present-time seawater incursion, but more likely to be the result of the repeated Arctic ocean regression and transgression over geological time.

Acknowledgements

This study is part of the Next-Generation Ecosystem Experiments (NGEE-Arctic) project sponsored by the Office of Biological and Environmental Research in the DOE Office of Science.

References

Dou, S., and Ajo-Franklin, J. (2014), Full-wavefield inversion of surface waves for mapping embedded low-velocity zones in permafrost: *Geophysics*, v. 79, no. 6, EN107-EN124. doi: 10.1190/geo2013-0427.1.

Herrmann, R. B., Computer programs in seismology. 2004.

Kennedy, J., and Eberhart, R. (1995), Particle swarm optimization: *Proceedings of IEEE International Conference on Neural Networks*, v. 4, 1942-1948. doi: 10.1109/ICNN.1995.488968.

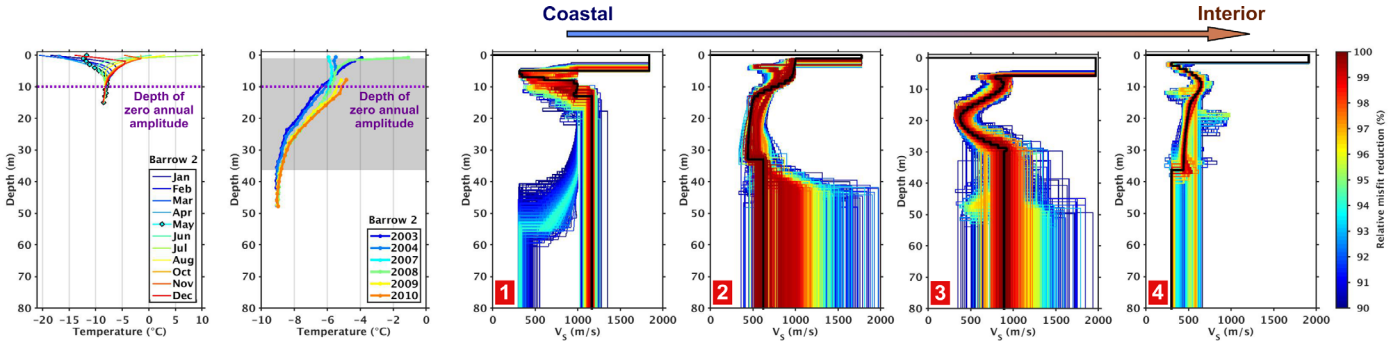

Figure 2.17.4: Inverted velocity profiles and the borehole temperature measurements at relevant depths.

18 Mantle Flow Geometry Beneath the Juan-de-Fuca Plate System

Robert Martin-Short, Richard Allen, Ian Bastow, Eoghan Totten, Mark Richards

Introduction

Over the past decades, measurement of seismic anisotropy has become a standard tool for understanding mantle convection. However, isolation of signals from the asthenosphere is challenging, because most seismometers are sited on continental crust, whose great thickness and complex deformation history influence seismic waves en-route to the surface. Thus, the challenge is to obtain data recorded on oceanic lithosphere, which is thinner and simpler. We present stacked shear wave splitting measurements from seismometers deployed across the Juan-de-Fuca and Gorda plates. This provides insight into seismic anisotropy beneath the oceanic lithosphere, allowing for an interpretation of mantle flow beneath an ocean basin from ridge to trench.

The Juan-de-Fuca plate system represents the northernmost section of the Farallon slab, which is approaching complete subduction beneath the North American continent (*Riddihough*, 1984). It is subdivided into the Explorer, Juan-de-Fuca and Gorda segments, which subduct at approximately N60°E along the Cascadia arc. Multiple lines of evidence point to segmentation of the subducting slab, a feature most clearly seen in tomographic studies (*Long et al.*, 2008).

Shear Wave Splitting

We investigate mantle flow geometry below the Juan-de-Fuca plate system using a combination of shear wave splitting and geodynamic modeling. Our seismic data comes from the Cascadia Initiative deployments, including 27 onshore Transportable Array (TA) sites (instrumented since 2010) and 70 ocean bottom seismometers (OBS), deployed in ten-month phases over four years (*Toomey et al.*, 2014). We analyze OBS data from years 1–3 of the Cascadia Initiative (2011–2012, 2012–2013, and 2013–2014) and four years of records from the NEPTUNE cabled seafloor observatory (*Heesemann*, 2014). We also utilize all public data from the X9 OBS array, deployed along the Blanco Fracture Zone in 2012–2013 (*Toomey et al.*, 2014).

The splitting parameters phi (Φ) and delay time (δt) are calculated using the software packages Splitlab (*Wustefeld et al.*, 2008) and SHEBA (*Wustefeld et al.*, 2009); the measurements are classified as 'good', 'fair', or 'poor' according to the criteria of Wüstefeld and Bokelmann (2008) and stacked using the method of Wolfe and Silver (1998). Filtering was used to optimize noise reduction without unduly compromising the splitting measurements.

Results and Interpretation

The TA (onshore) stations produce a uniform splitting pattern along the length of the subduction zone (Figure 2.18.1). The mean fast direction and delay time are N72°E and 1.34 seconds, respectively. Stations on the Juan-de-Fuca plate display a more

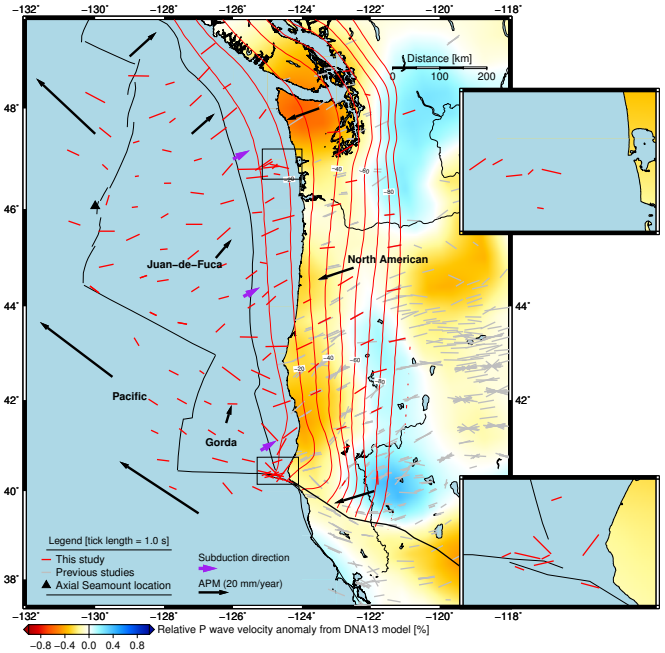

Figure 2.18.1: Map showing the shear wave splitting results determined by this study (red bars) alongside a compilation of previous work. The displayed tomography is a vertical average through the DNA13 P-wave velocity model of Porritt et al. (2014) between depths of 100 and 400 km, which corresponds to the range thought to be the main source of the obsrved anisotropy. Black lines indicate plate boundaries, while the red lines are slab depth contours spaced at 10 km intervals. Black arrows show the direction and magnitude of absolute plate motion (APM), while purple arrows show the subduction direction (*Gripp and Gorden*, 2002). The splitting pattern on Juan-de-Fuca rotates from roughly NW-SE orientations west of the ridge to SW-NE orientations at the trench, before migrating into the subduction direction onshore. On Gorda the splitting geometry is well aligned with the direction of Pacific plate motion, but switches suddenly into a subducton parallel orientation east of the trench.

complicated splitting geometry: with the exception of a single, ridge-parallel result near Cobb Hotspot, splitting directions vary between trench perpendicular and the plate-motion direction. Alignment with APM direction increases towards the trench, and the measurements then rotate into the subduction direction as one moves onshore.

Sites on the Gorda plate produce a highly uniform pattern, but they are neither aligned with Gorda motion nor the subduction direction. Their mean splitting direction of N66°W aligns more closely with the motion of the Pacific plate (~N57°W13). A marked change in splitting direction is observed just east of the trench in this region, where the fast directions rotate approximately 70° into a trench-perpendicular orientation.

The main source of the observed anisotropy is interpreted to be the lattice-preferred orientation (LPO) of mantle olivine crystals, whose alignment is caused by viscous shearing of the asthenosphere. Thus, the splitting pattern provides first order constraints on asthenosphere flow geometry. We suggest that

basal drag of the moving plates provides the greatest influence on mantle flow in this region, thus explaining why the splitting pattern on Juan-de-Fuca becomes increasingly well aligned with APM as one moves east, away from the influence of the ridge.

The splitting pattern on Gorda is interesting because it suggests that asthenospheric flow beneath this plate is controlled by the regional pattern of shearing induced by the north-

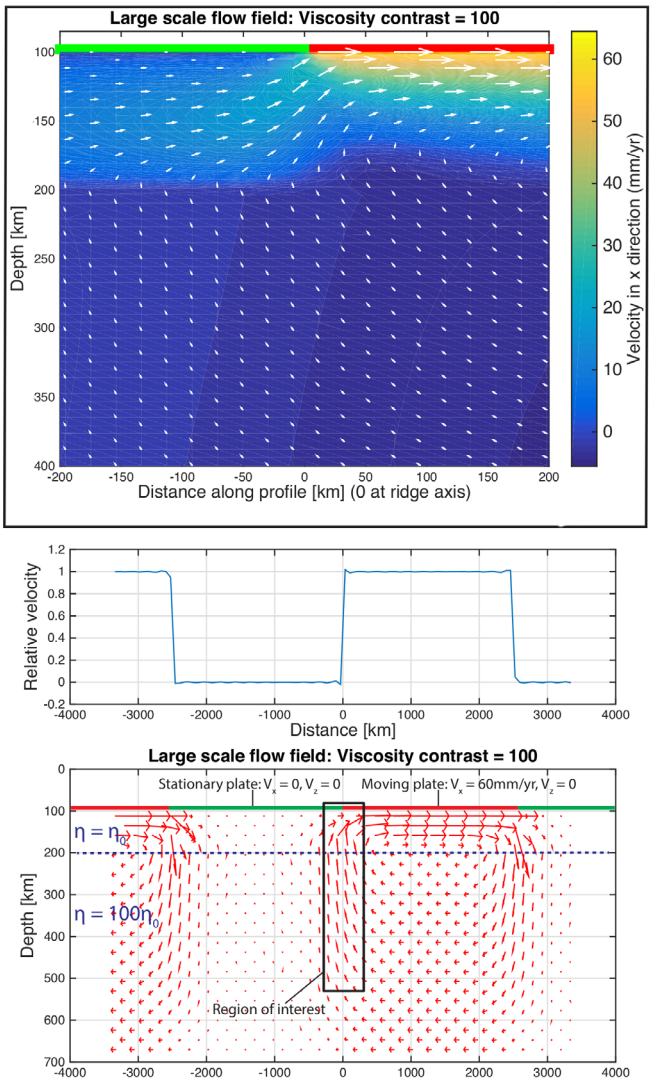

Figure 2.18.2: Results of two-dimensional modeling using the method of Hagar and O'Connell (1981) to simulate the mantle flow geometry below the Gorda plate as induced by the motion of the Pacific plate. In these models the green plate is stationary, while the red plate moves to the right at a rate of 60 mm/yr. This roughly simulates the situation in profile perpendicular to the Gorda ridge. The vertical velocity is set to zero at depths of 100 km (corresponding to the base of the lithosphere) and 660 km. The model consists of two layers—an 'asthenosphere' from 100–200 km and a 'lower mantle' below 200 km depth. The viscosity of the lower mantle is 100-times that of the asthenosphere. The lower panel shows details of the model set-up, including the imposed periodic surface velocity field and region of interest. Motion of the moving plate is seen to stimulate a flow field beneath the adjacent stationary plate. This lends credence to our interpretation that the shear wave splitting pattern observed on Gorda could be a result of the rapid motion of the nearby Pacific plate.

westward motion of the Pacific plate, which moves at about 60 mm/yr (*Gripp and Gorden*, 2002). The Gorda plate is small and has a low absolute velocity. Additionally, it is undergoing internal deformation and is divided into a series of small, fault-controlled blocks (*Wilson*, 1989). In contrast, the Pacific plate is large, intact and fast moving. We have constructed a 2D model of this situation using the method of Hager and O'Connell (1981) to show that motion of the Pacific plate is capable of generating significant westward flow beneath the width of the Gorda, under the assumption that flow is largely confined to the uppermost mantle due to a thin, low viscosity channel (viscosity contrast 100, channel thickness 100 km) beneath the Gorda plate. This simple model demonstrates the plausibility of our interpretation of the splitting pattern (Figure 2.18.2).

Acknowledgements

This study was made possible by the crews of the various research vessels involved in the deployment and recovery of Cascadia Initiative seismometers. The work benefitted from discussions with Jennifer Lodewyk, Andy Frassetto, and Caroline Eakin. GMT (*Wessel and Smith*, 1998) and MATLAB where used to create the figures.

References

Gripp, A. E. and Gordon, R. G. (2002), Young tracks of hotspots and current plate velocities, *Geophysical Journal International,* 150, 321-361.

Hager, B. H. and O'Connell, R. J. (1981), A simple global model of plate dynamics and mantle convection, *Journal of Geophysical Research: Solid Earth*, 86, 4843-4867.

Heesemann, M., *et al.* (2014), Ocean Networks Canada: From geohazards research laboratories to Smart Ocean Systems, *Oceanography,* 27, 151-153.

Long, M. D. and Silver, P. G. (2008), The subduction zone flow field from seismic anisotropy: a global view, *Science,* 319, 315-318.

Porritt, R.W., Allen, R.A., and Pollitz, F.F. (2014), Seismic imaging east of the Rocky Mountains with USArray, *Earth and Planetary Science Letters,* 402, 16-25.

Riddihough, R. (1984), Recent movements of the Juan de Fuca plate system, *Journal of Geophysical Research: Solid Earth*, 89, 6980-6994.

Toomey, D. R., *et al.* (2014), The Cascadia initiative: A sea change in seismological studies of subduction zones, *Oceanography*, 27(2), 138-150.

Wessel, P. and Smith, W. H. (1998), New, improved version of Generic Mapping Tools, *Eos, Transactions American Geophysical Union,* 79, 579-579.

Wilson, D. S. (1989), Deformation of the so-called Gorda Plate, *Journal of Geophysical Research: Solid Earth*, 94, 3065-3075.

Wolfe, C. J. and Silver, P. G. (1998), Seismic anisotropy of oceanic upper mantle: Shear wave splitting methodologies and observations, *Journal of Geophysical Research: Solid Earth*, 103, 749-771.

Wüstefeld, A., *et al.* (2008), SplitLab: A shear-wave splitting environment in Matlab, *Computers and Geosciences*, 34, 515-528.

Wüstefeld, A., *et al.* (2009), Identifying global seismic anisotropy patterns by correlating shear-wave splitting and surface-wave data, *Physics of the Earth and Planetary Interiors*, 176, 198-212.

19 Accumulation of Buoyant Material Beneath Subducting Juan de Fuca Plate

William B. Hawley, Richard M. Allen, Mark A. Richards

Introduction

Plate tectonics is fundamental to the explanation of a wide range of geological phenomena, yet there is no complete physical description of how it operates. Of particular interest is the degree to which these lithospheric plates are coupled to the convecting mantle beneath. Recent studies (*Kawakatsu et al.*, 2009; *Naif et al.*, 2013; *Stern et al.*, 2015) and thus the understanding of the processes at the lithosphere-asthenosphere boundary (LAB suggest a layer rich in partial melt beneath oceanic lithosphere. A region of high partial melt is mechanically weak and buoyant, so we must ask what happens to it at subduction zones. We use teleseismic body waves to image the mantle below the Cascadia Subduction Zone, which reveal a strong low-velocity anomaly just below the flexing slab. We propose this feature is accumulated low-velocity, buoyant, weak material from beneath the Juan de Fuca lithosphere and use a geodynamical model to show how it would accumulate.

Data

The Cascadia Initiative (CI) (*Toomey et al.*, 2014) is a four-year (2011–2015) seismic deployment that covers the Juan de Fuca (JdF) plate and Cascadia Subduction Zone (CSZ). It is comprised of 70 broadband ocean-bottom seismometers (OBS) that occupy 120 sites, as well as 27 land-based stations. We use 61,559 P-wave arrivals from 444 teleseismic ($30° \leq \Delta \leq 80°$) events (M_W 6.0 to 7.5) observed by the Transportable Array, CI, and other regional networks to generate a P-velocity model through finite-frequency tomographic inversion following Obrebski et al. (2010). The noise characteristics of the OBS require that we filter arrivals to long periods (9.1 – 12.5 seconds). Our application of finite-frequency sensitivity kernels means that there is no need for smoothing.

Tomographic Model

Our inversion shows a north-striking, east-dipping, high-velocity (+3% P-wave velocity, dV_p) JdF slab, seen at 100 km depth as a north-south structure at 122°W between 40°N and 50°N (Figure 2.19.1a). A previously unidentified low-velocity anomaly (-2 to -3% dV_p) is also seen with similar strike as the JdF slab, just to the west. This feature appears just beneath the JdF plate, but the bulk of the signal is restricted to the top 200 km of the model, while the JdF signal extends as deep as 400 km.

Interpretation

Our observation of this low V_p "sausage" in Cascadia appears unique, but is likely related to observations of a layer of partial melt beneath Pacific, Philippine Sea, and Cocos lithospheres reported in studies by Kawakatsu et al. (2009), Naif et al. (2013), and Stern et al. (2015). These studies used different techniques—Kawakatsu et al. used receiver functions from borehole OBS, Naif et al. used a magnetotelluric array, and Stern et al. used explosion-generated reflected P-waves—to resolve a narrow (10-25 km) region immediately below oceanic lithospheres characterized by low seismic wave velocities (-7 to -10% dV_s and dV_p) and high conductivity (4 to 6 Ω m), which the authors interpret as partial melt fractions of ~1 to 4%.

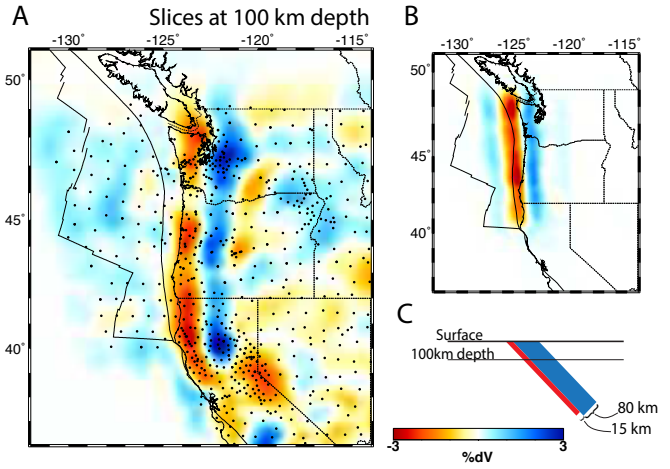

Figure 2.19.1 Horizontal slice at 100 km depth from our model. A) The three tectonic plates are labeled, delineated by the thin black lines. Stations used in the inversion are dots; additional stations were used to the east and south of the map shown. The background color shows the relative P-wave velocity as a percent deviation from the average of the model, as shown by the lower right color bar. B) Recovery of a synthetic +4%dV_p 80 km thick slab underlain by a -10%dV_p 15 km thick slab. The extent of each is similar, and resembles the anomalies in (A). C) A schematic of the synthetic model recovered in (B).

While these observations appear to illuminate a thinner feature than that observed in our tomographic model, our frequency-dependent sensitivity kernels explain the thickness of our observed low-velocity feature. Figure 2.19.1b shows a synthetic recovery of two dipping structures: an 80-km thick, +4% dV_p layer underlain by a 15-km thick, -10% dV_p layer, arranged as in Figure 2.19.1c. After the inversion, the two layers appear to be of similar thickness and intensity. Since our observation is consistent with a previously reported feature, we believe the two are linked, not unique to Cascadia, and not transient.

Geodynamical Model

The large partial melt fraction proposed for this layer implies that it is weak and buoyant (*Hirth and Kohlstedt*, 1996). We suggest the material is accumulating beneath the subducting slab because its buoyancy and low viscosity prevent it from being advected down-dip. A simple geodynamical argument shows that this mechanism results in accumulation of low-viscosity material at the subduction zone.

Figure 2.19.2 shows the schematic of a simple proposed model in cross section. A layer of thickness h, viscosity μ, and

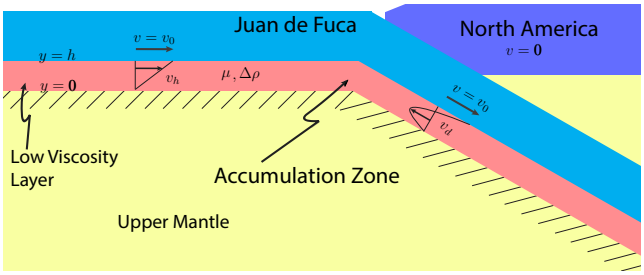

Figure 2.19.2 A schematic of the geodynamical model setup. Fluxes derived from the horizontal velocity, v_h , and the dipping velocity, v_d, show that more material enters the subduction zone than is advected away (see text). This results in accumulation of material at the point labeled "accumulation zone."

density difference Δρ is between a rigid, stationary mantle and a rigid plate moving with velocity v_0. Ocean-ward of the trench, advection by the overriding plate drives the (horizontal) velocity, defined as simple Couette flow, $v_h = v_o(y/h)$. Down-dip of the trench, Couette flow is modulated by Poiseuille flow driven by the buoyancy of the material, such that the (dipping) velocity $v_d = v_o(y/h) - ((\Delta\rho g y \sin\theta/(2\mu))(y-h)$. The accumulation rate of this material depends on the relative contributions of the Couette and Poiseuille terms. Integrating to flux, the Couette term is $f_c = (1/2)v_o h$, and the Poiseuille term is $f_p = -(\Delta\rho g h^3 \sin\theta)/12\mu$. We use conservative estimates for the parameters to compare the Couette and Poiseuille flux terms; v_0 = 40mm yr^{-1} (Wilson, 1993) 50–100 km south of the active Sovanco transform. Slight deformation of the northern Juan de Fuca plate adjacent to the Nootka fault zone is also apparent East of the northern Gorda ridge, younger (< 3 Ma, h = 10km, Δρ = 1kg m^{-3} (~0.1% density of basalt), g = 9.8 m s^{-2}, and μ = 10^{17} Pa s (Hirth and Kohlstedt, 1996; Kawakatsu et al., 2009). These parameters produce a Poiseuille flux of order 10^{-5} m^2 s^{-1}, and a Couette flux of ~5 × 10^{-6} m^2 s^{-1}. A significant Poiseuille term means the weak region atop the asthenosphere would collect beneath a subducting plate where it starts to dive into the deeper mantle.

Discussion

This accumulated material could be partly responsible for rapid uplift (*Zandt and Furlong*, 1982) and volcanism in the Coast Range of California. Lachenbruch and Sass (1980) proposed that as the southern edge of the Gorda-JdF slab migrates northward with the Mendocino Triple Junction, the window that opens beneath North America fills with asthenosphere which undergoes decompression melting, and leads to high heat flow and volcanism. Seismic observations by Hole et al. (1998) and Furlong and Schwartz (2004) reveal a high-velocity mafic layer at the bottom of the North American crust that requires more melt than standard asthenospheric upwelling models predict. Yet both the lack of high-grade metamorphism inferred from the seismic studies as well as the heat flow observations of Lachenbruch and Sass (1980) require less heat than predicted from the same asthenospheric upwelling models (*Hole et al.*, 1998). A mechanism to generate more melt at lower temperatures has been elusive, but the accumulated low-velocity material may provide that mechanism.

Conclusions

We propose that a previously observed region of large partial melt fraction at the base of oceanic lithospheres is prone to accumulate at subduction zones due to its own buoyancy, and we provide the first tomographic evidence of such a feature in the Cascadia Subduction Zone. Both the chemistry and the rheological properties of this accumulation zone have implications for the California Coast Range, as well as for subduction dynamics in general.

Acknowledgements

We would like to thank the Ocean Bottom Seismograph Instrument Pool (OBSIP) Management Office (OMO) staff for help in managing and understanding the OBS data. IRIS and the Cascadia Initiative Expedition Team provided the data for this work.

References

Furlong, K.P., Schwartz, S.Y., 2004. Influence of the Mendocino Triple Junction on the Tectonics of Coastal California. Annu. Rev. Earth Planet. Sci. 32, 403–433. doi:10.1146/annurev.earth.32.101802.120252

Hirth, G., Kohlstedt, D.L., 1996. Water in the oceanic upper mantle: implications for rheology, melt extraction and the evolution of the lithosphere. Earth Planet. Sci. Lett. 144, 93–108. doi:10.1016/0012-821X(96)00154-9

Hole, J.A., Beaudoin, B.C., Henstock, T.J., 1998. Wide-angle seismic constraints on the evolution of the deep San Andreas plate boundary by Mendocino triple junction migration. Tectonics 17, 802–818. doi:10.1029/98TC02261

Kawakatsu, H., Kumar, P., Takei, Y., Shinohara, M., Kanazawa, T., Araki, E., Suyehiro, K., 2009. Seismic Evidence for Sharp Lithosphere-Asthenosphere Boundaries of Oceanic Plates. Science 324, 499–502. doi:10.1126/science.1169499

Lachenbruch, A.H., Sass, J.H., 1980. Heat flow and energetics of the San Andreas Fault Zone. J. Geophys. Res. Solid Earth 85, 6185–6222. doi:10.1029/JB085iB11p06185

Naif, S., Key, K., Constable, S., Evans, R.L., 2013. Melt-rich channel observed at the lithosphere-asthenosphere boundary. Nature 495, 356–359. doi:10.1038/nature11939

Obrebski, M., Allen, R.M., Xue, M., Hung, S.-H., 2010. Slab-plume interaction beneath the Pacific Northwest. Geophys. Res. Lett. 37, L14305. doi:10.1029/2010GL043489

Stern, T.A., Henrys, S.A., Okaya, D., Louie, J.N., Savage, M.K., Lamb, S., Sato, H., Sutherland, R., Iwasaki, T., 2015. A seismic reflection image for the base of a tectonic plate. Nature 518, 85–88. doi:10.1038/nature14146

Toomey, D., Allen, R., Barclay, A., Bell, S., Bromirski, P., Carlson, R., Chen, X., Collins, J., Dziak, R., Evers, B., Forsyth, D., Gerstoft, P., Hooft, E., Livelybrooks, D., Lodewyk, J., Luther, D., McGuire, J., Schwartz, S., Tolstoy, M., Trehu, A., Weirathmueller, M., Wilcock, W., 2014. The Cascadia Initiative: A Sea Change In Seismological Studies of Subduction Zones. Oceanography 27, 138–150. doi:10.5670/oceanog.2014.49

Wilson, D.S., 1993. Confidence intervals for motion and deformation of the Juan de Fuca Plate. J. Geophys. Res. Solid Earth 98, 16053–16071. doi:10.1029/93JB01227

Zandt, G., Furlong, K.P., 1982. Evolution and thickness of the lithosphere beneath coastal California. Geology 10, 376–381. doi:10.1130/0091-7613(1982)

20 3D Pre-Stack Depth Migration of Receiver Functions with the Fast Marching Method: A Kirchhoff Approach

Cheng Cheng, Thomas Bodin, Richard Allen

Introduction

We present a novel 3 D pre-stack Kirchhoff depth migration (PKDM) method for teleseismic receiver functions. The proposed algorithm considers the effects of diffraction, scattering, and traveltime alternation caused by 3 D volumetric heterogeneities. It is therefore particularly useful to image complex 3 D structures such as dipping discontinuities, which is hard to accomplish with traditional methods. The whole scheme is based on the acoustic wave migration principle. At each time step of the receiver function, energy is migrated back to the ensemble of potential conversion points in the image, given a smooth 3 D reference model. Traveltimes for P and S waves are computed with an efficient Eikonal solver, the Fast Marching Method (FMM). We also consider elastic scattering patterns, where the amplitude of converted S waves depend on the angle between the incident P wave, and the scattered S wave. Synthetic experiments demonstrate the validity of the method for a variety of dipping angle discontinuities. Comparison with the widely used Common Conversion Point (CCP) stacking method reveals that our migration shows considerable improvement. For example, the effect of multiple reflections that usually produce apparent discontinuities, is avoided. The proposed approach is practical, computationally efficient, and is therefore a potentially powerful alternative to standard CCP methods for imaging large-scale continental structure under dense networks.

Method

Pre-stack Kirchhoff migration of seismic records is a well-established technique in industries to image shallow sedimentary structures. It was later introduced to seismology for imaging larger scale structures as local networks became dense enough. Teleseismic Kirchhoff migration is an imaging scheme applied to the scattered wavefield associated to incident body waves recorded at an array of stations. The data are weighted and stacked along diffraction hyperbolae for every potential scattering point in a regular grid, defining the model space.

Effectively, one sums over all the available data that have a traveltime consistent with the scatterer at the target point, *r*. The main advantage of pre-stack migration techniques over CCP depth mapping is that they make much fewer assumptions about the subsurface structure, and thus consider seismic scattering in more general terms. However, they still rely on a smoothly varying background velocity model, necessary to back-project the scattered wavefield. In practice, we can get this absolute velocity model from either global or regional tomographic images, 3D volumetric large-scale velocity structure is essential for proper image focusing.

Our method can be viewed as a simplification on Levander et al.'s (2005) acoustic equation in order to consider real 3 D structures, improved by incorporating elastic scattering patterns,

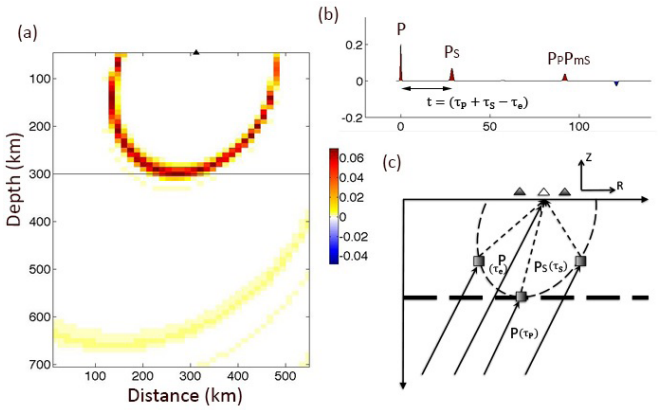

Figure 2.20.1: Schematic illustrations of how Kirchhoff migration works for a teleseismic receiver function. (a) Migrated parabola of one receiver function, constructed from a simple model made of a horizontal layer over a half space. A vertical slice is shown. (b) Synthetic receiver function used for migration. (c) Ray paths for direct P wave and transmitted S wave in the same vertical plane as (a). The converted P_s phase is migrated to all possible conversion points that predict the observed traveltime, *t*.

which will be discussed in detail in the following sections.

Overall, the main advantage of our method is the computational efficiency, which makes feasible applications at continental scales. Instead of calculating the full wavefield at each grid point by using an expensive 2D finite-difference solver. We make some simplifications, which allow us to include the full 3D velocity structure. Instead of calculating the traveltime geometric spreading term using a finite-difference solver in a heterogeneous model, we simplify it as a 1/d term in a 3D case (*Rondenay*, 2009), where *d* is the distance between *r* and r_0. In this way, these simplifications leave us with only the traveltime calculation, for which we implement with the Fast Marching Method.

Figure 2.20.1 illustrates how teleseismic Kirchoff migration works in our receiver function case.

Synthetic Testing Results

We compare the results of CCP depth mapping and final FMM pre-stack migration for different dipping interfaces (Figure 2.20.2). Imaging dipping structures is one of the challenges in understanding the dynamics of subduction zones (*Rondenay*, 2009). The images obtained by 3 D pre-stack migration are shown along the same profile, which is perpendicular to the strike of the dipping plane. This allows us to directly compare the two approaches and see their systematic differences.

As shown in Figure 2.20.2a and d, both methods recover the discontinuity quite well in the 0° dipping case. However, the pre-stack Kirchhoff migration does not show any artifacts due to multiple reflections, as the energy does not interfere

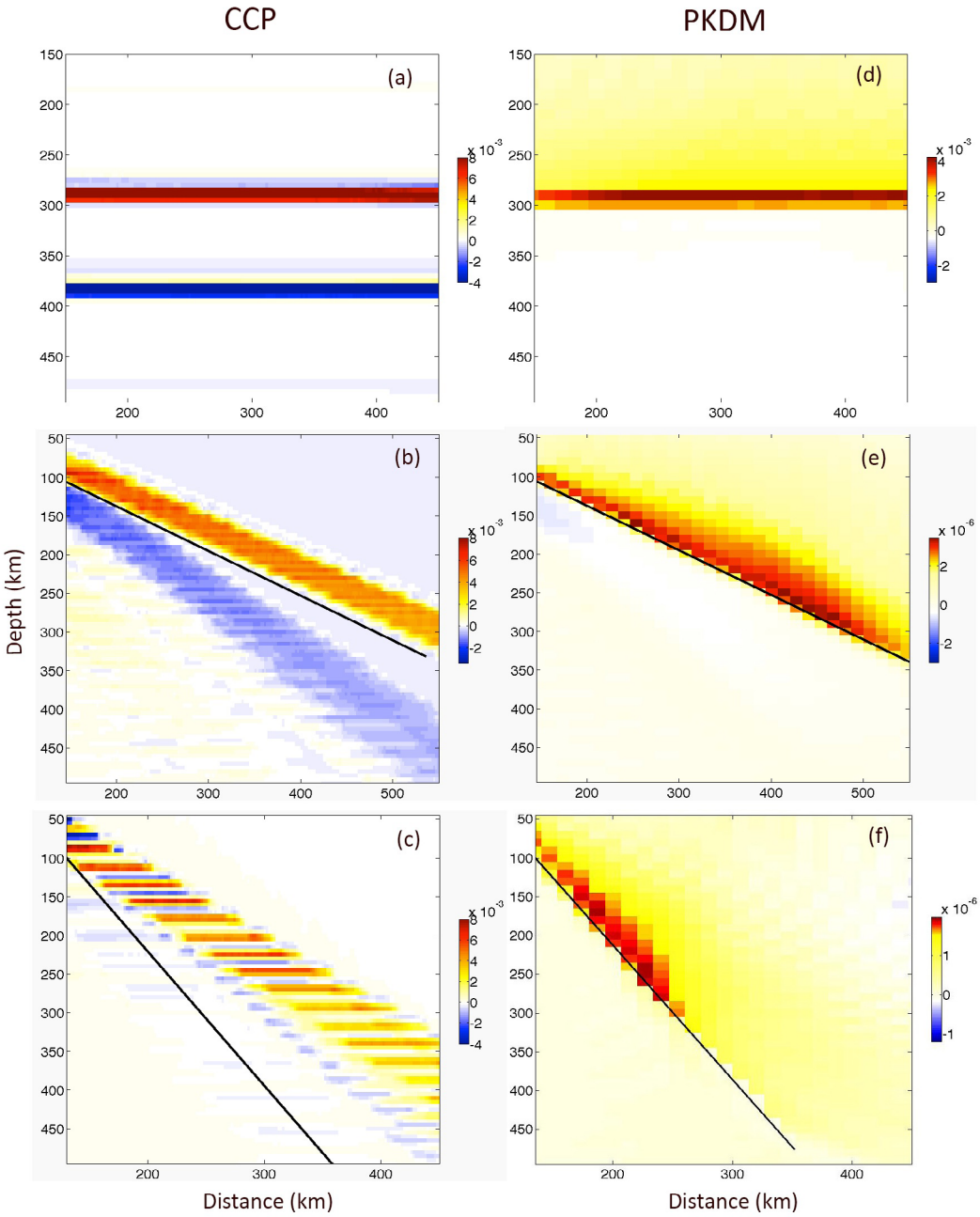

Figure 2.20.2: Receiver function images using CCP depth migration (a)-(c), and 3D pre-stack Kirchhoff depth migration (d)-(f) for our three synthetic models with dips of 0° (a,d), 30° (b,e), and 60° (c,f). Solid black lines mark the real location of the model discontinuity

constructively during the stacking process. When interpreting receiver function CCP stacks, it is well known that the image is contaminated by spurious discontinuities due to multiples. How and whether to interpret the negative energy below the Moho or other positive discontinuities is unclear. The lithospheric signal can be at the same depth as the multiples. In the case of dipping interfaces, the assumption of a horizontal and planar structure adopted in the CCP stacking leads to either wrong information on geometry or distortion of the shape of the discontinuities, such as shallow dipping structures or defocussing of the diffracted energies (Figure 2.20.2b and c). In contrast, pre-stack migration significantly reduces unwanted stacking effects and properly accounts for the propagation effects of lateral heterogeneities by making no assumption on the shape of the discontinuities (Figure 2.20.2e and f).

References

Rondenay, S. (2009), Upper mantle imaging with array recordings of converted and scattered teleseismic waves, *Surv. Geophys.*, 30, 377-405.

Levander, A., Niu, F. & Symes, W.W. (2005), Imaging teleseismic P and S scattered waves using the Kirchhoff integral. In: Levander A, Nolet G (eds) Seismic Earth: array analysis of broadband seismograms. *AGU Geophysical Monograph*. AGU, Washington, DC. No. 157, 149–169, doi: 10.1029/157GM10.

Research Studies:
Rheology and Fault Mechanics

22 Pushing the Limits of InSAR for Interseismic Deformation Characterization

Estelle Chaussard, Roland Bürgmann, Heresh Fattahi, Christopher W. Johnson, and Ingrid Johanson

Abstract

Evaluation of interseismic deformation (fault creep and strain accumulation) traditionally relies on terrestrial short-baseline measurements for creep and GPS for regional deformation, which provide precise but sparse measurements. Here, we show that InSAR (Interferometric Synthetic Aperture Radar) can resolve small-amplitude long- and short-wavelengths, horizontal and vertical displacements associated with interseismic deformation. InSAR is kept independent from GPS data. We show that a large 1992-2011 SAR dataset over the San Francisco Bay Area enables characterization of local and regional deformation signals as small as 2 mm/yr without the need of aligning the velocity field to a GPS-based model. By implementing an interferogram selection method directly based on the spatial coherence, our new time series approach enables interseismic deformation mapping in vegetated areas with a high spatial coverage.

Method

1) Long-wavelength deformation from InSAR

InSAR remains rarely used to characterize long-wavelength deformation due to long-wavelength noise (ramps) resulting from orbital errors, which are considered to be larger than the interseismic signal (e.g. Bürgmann et al., 2006). However, Fattahi and Amelung (2014) showed that when combining tens to hundreds of SAR acquisitions through time series analysis, the orbital accuracy of SAR satellites enables detection of long-wavelength deformation of a few mm per year per hundred kilometers. We use over 250 SAR images acquired by the ERS1-2 and Envisat satellites of the European Space Agency to resolve the 1992-2011 interseismic deformation in the San Francisco Bay Area. By combining hundreds of acquisitions, the mean velocity map precision is ~1.3 mm/yr/100km, given the orbital accuracy, which enables detection of long-wavelength deformation without removing any orbital ramps (except for a local oscillator drift correction applied to Envisat ASAR) and without performing any alignment to a prior model of deformation based on GPS data (allowing InSAR and GPS data to be kept independent).

2) Maintaining coherence in vegetated areas

To measure interseismic deformation it is necessary to maintain coherence across faults despite the transition from urban areas to vegetated hillslopes. We develop an alternative interferogram selection method that accounts for the level of spatial coherence in each interferogram for consideration in the SBAS (Small Baseline Subset) time series inversion (*Berardino et al*., 2002) (Figure 2.22.1). Only interferograms with a high percentage of pixels (50%) above a sufficient spatial correlation (0.5) in our area of interest, comprising vegetated hillsides across the Calaveras Fault (black rectangle on the bottom row of Figure 2.22.1), are included in the time series analysis, leading to temporal coherence >0.5 in the east compared to values of ~0.3 with the standard SBAS selection (Figure 2.22.1).

3) Validation

To compare InSAR velocities with independent datasets (horizontal GPS), we must first separate the InSAR line of sight (LOS) into its horizontal and vertical components. We combine ascending and descending velocity maps to retrieve horizontal and vertical displacement fields following the approach of *Wright et al*. (2004). Figure 2.22.2a shows the vertical velocity field and the horizontal velocity field projected into motion parallel to the average strike of the Hayward and Calaveras Faults (N32°W). We then compare horizontal InSAR velocities with horizontal BAVU3 GPS velocities (*Bürgmann et al*., 2014) (Figure 2.22.2b), both referenced to the GPS station LUTZ in order to evaluate the InSAR accuracy.

Results

Our coherence based selection leads to a much higher spatial coverage than previous works (*Shirzaei and Bürgmann, 2013*) but some acquisitions must be discarded due to low coherence, leading to a lower temporal sampling (Figure 2.22.1 top rows, red). For the evaluation of steady interseismic deformation, the increased spatial coverage in vegetated areas is necessary.

Decomposition of LOS InSAR into vertical and horizontal motions (Figure 2.22.2a) confirms that most of the interseismic deformation in the Bay Area is horizontal (i.e., tectonic), the vertical deformation mostly local and hydrologic (subsidence along shorelines and floodplains due to compaction of man-made fill and clay rich Bay mud and uplift in the Santa Clara Valley due to long-term aquifer system recovery (*Chaussard et al*., 2014)). The horizontal deformation illustrates the tectonic interseismic deformation (Figure 2.22.2a, right). We resolve its two components: the long-wavelength deformation (color gradient) corresponding to the elastic strain accumulation along locked faults of the San Andreas system, and the short-wavelength deformation (near-fault) marked by sharp color jumps observed across the creeping Hayward and Calaveras Faults (*Chaussard et al.*, 2015).

The comparison between independent horizontal InSAR and GPS velocities (Figure 2.22.2b) shows good agreement with an average absolute deviation of 2 mm/yr. Velocities at pixels with temporal coherence higher than 0.7 (blue circles) or between 0.5-0.7 (green triangles) also agree equally well with the GPS data. This confirms that a temporal coherence threshold of 0.5 is acceptable in the Bay Area. These results demonstrate that InSAR mean velocity maps enable resolving vertical and horizontal deformation partitioning in the Bay Area for both short and long wavelength signals as small as 2mm/yr.

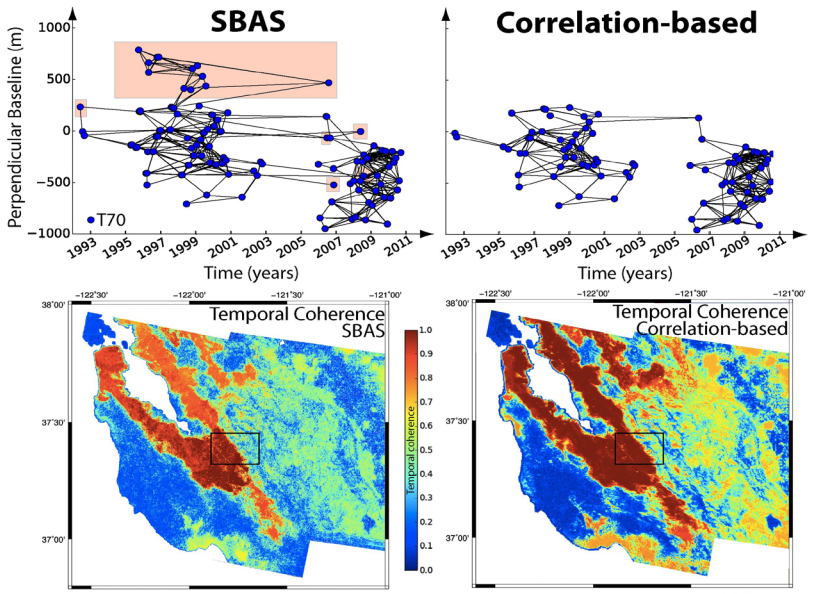

Figure 2.22.1: Comparison between SBAS (left) and our correlation based selection (right) using only interferograms with over 50% of pixels with correlation >0.5 in the area of interest (black box on bottom row). Top: baseline plots for tracks 70, bottom: resulting temporal coherence maps.

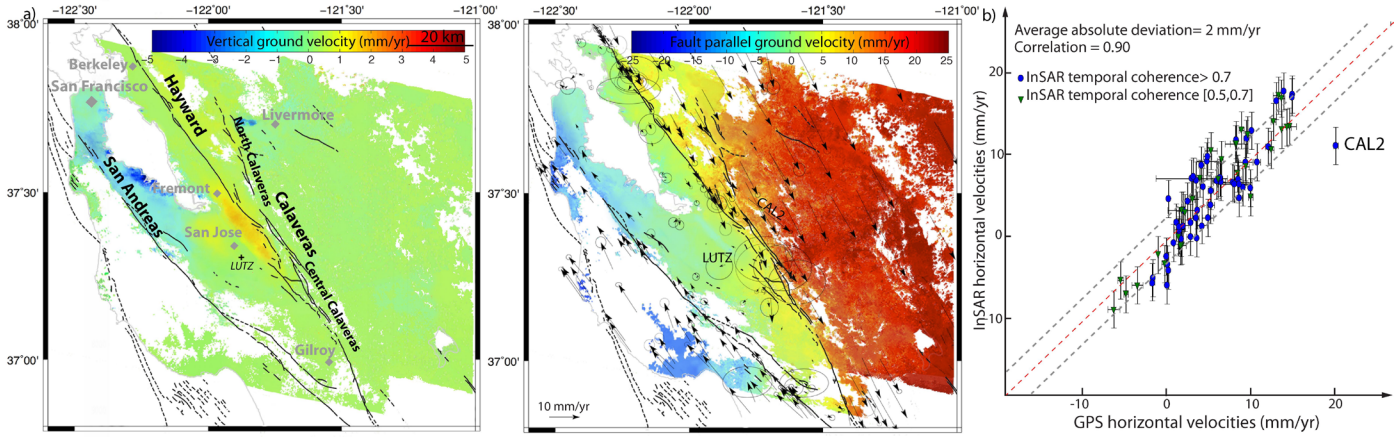

Figure 2.22.2: a) Mean vertical (left) and Hayward-Calaveras Fault-parallel (right) ground velocity from 19 years of SAR data in the San Francisco Bay Area with respect to GPS station LUTZ. Black lines are mapped fault traces and grey diamonds main cities. Black arrows show horizontal BAVU3 GPS velocities. b) InSAR velocities mean rate for pixels within 200 m from each GPS station. Blue circles show pixels with a temporal coherence >0.7 in the InSAR velocity map, green triangles pixels with a temporal coherence between 0.5-0.7.

Acknowledgments

We thank NASA for support through grant NNX12AQ32G and the U.S. Geological Survey National Earthquake Hazards Reduction Program (NEHRP) for support through grants G12AP20096 and G13AP00035.

References

Berardino, P., G. Fornaro, R. Lanari, and E. Sansosti, A new algorithm for surface deformation monitoring based on small baseline differential SAR interferograms, *IEEE Trans. Geosci. Remote Sensing*, 40(11), 2375–2383, doi:10.1109/TGRS.2002.803792, 2002.

Bürgmann, R., G. Hilley, A. Ferretti, and F. Novali, Resolving vertical tectonics in the San Francisco Bay Area from permanent scatterer InSAR and GPS analysis, *Geol.*, 34(3), 221, doi:10.1130/G22064.1, 2006.

Chaussard, E., R. Bürgmann, H. Fattahi, R. M. Nadeau, T. Taira, C. W. Johnson, and I. Johanson, Potential for larger earthquakes in the East San Francisco Bay Area due to the direct connection between the Hayward and Calaveras Faults, *GRL.*, 42, 2015.

Chaussard, E., R. Bürgmann, M. Shirzaei, E. J. Fielding, and B. Baker, Predictability of hydraulic head changes and characterization of aquifer-system and fault properties from InSAR-derived ground deformation, *JGR*, 119, 6572–6590, 2014.

Fattahi, H., and F. Amelung (2014), InSAR uncertainty due to orbital errors, *Geophysical Journal International*, 199(1), 549–560, doi:10.1093/gji/ggu276, 2014.

Shirzaei, M., and R. Bürgmann, Time-dependent model of creep on the Hayward fault from joint inversion of 18 years of InSAR and surface creep data, *JGR*, 118(4), doi:10.1002/jgrb.50149, 2013.

Wright, T. J., B. E. Parsons, and Z. Lu, Toward mapping surface deformation in three dimensions using InSAR, *GRL*, 31(1), doi:10.1029/2003GL018827, 2004

23 Potential for Larger Earthquakes in the East San Francisco Bay Area Due to the Direct Connection Between the Hayward and Calaveras Faults

Estelle Chaussard, Roland Bürgmann, Heresh Fattahi, Robert M. Nadeau, Taka'aki Taira, Christopher W. Johnson, and Ingrid Johanson

Abstract

The Hayward and Calaveras Faults (HC and CF), two strike-slip faults of the San Andreas System in the East San Francisco Bay Area, are commonly considered independent structures for seismic hazard assessment. We use InSAR (Interferometric Synthetic Aperture Radar) to show that surface creep on the Hayward Fault continues 15 km farther south than previously known, revealing new potential for rupture and damage south of Fremont. The extended trace of the Hayward Fault, also illuminated by shallow repeating micro-earthquakes, documents a surface connection with the Calaveras Fault. At depths greater than 3-5 km, repeating micro-earthquakes located 10 km north of the surface connection highlight the 3-D wedge geometry of the junction. Our new model of the HF and CF argues that they should be treated as a single structure with potential for earthquake ruptures generating events with magnitudes greater than 7, posing a higher seismic hazard than previously considered.

Method

1) InSAR

Traditionally, faults' surface traces are mapped using spatially limited field observations. InSAR observations of surface creep have been used to identify the HF trace in urban areas (*Schmidt et al.*, 2005; *Shirzaei and Bürgmann*, 2013), but fault traces have not been successfully delineated in vegetated hillsides due to loss of coherence. To overcome this limitation we modify the small baseline subset (SBAS) time series method (*Berardino et al.*, 2002) to select only interferograms with a high percentage of pixels (50%) above a sufficient spatial correlation (0.5) in our area of interest that is comprised of vegetated hillsides across the CF. We resolve the 1992-2011 deformation using time-series analysis of ERS and Envisat data, with >250 acquisitions from 4 tracks (2 descending and 2 ascending, combined to retrieve horizontal and vertical components). The only ramp removed in the processing is the local oscillator drift correction of the Envisat ASAR instrument. The remaining signal contains only small orbital errors (~1.3 mm/yr/100 km) (*Fattahi and Amelung*, 2014).

2) Characteristically Repeating Earthquakes

To illustrate the 3D geometry of the faults we rely on characteristically repeating earthquakes (CREs). CRE sequences are events occurring in essentially identical locations, with similar magnitudes, and with high waveform correlation coefficients. They represent small locked asperities that are repeatedly loaded to rupture by surrounding creep. The scaling between recurrence time, seismic moment, and CRE slip, first established at Parkfield (*Nadeau and Johnson*, 1998), is now widely used to obtain fault slip parameters. We evaluate CRE locations using the Double-Difference Real-Time catalog (*Waldhauser and Schaff*, 2008) and cumulative displacement using the empirical relationship between seismic moment and slip (*Nadeau and Johnson*, 1998).

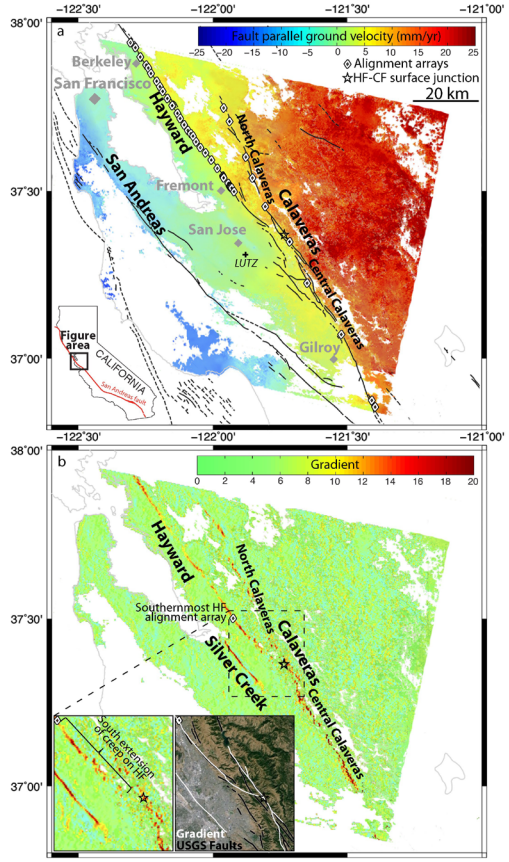

Figure 2.23.1: a) Mean HF-parallel ground velocity. Blue colors are NW motion and red colors SE with respect to the GPS station LUTZ. Black lines are fault traces, white diamonds alignment-array, black star shows the HF-CF surface junction, and grey diamonds are major cities. b) Derived gradient map. High gradient (red) correspond to the surface traces of creeping faults (HF and CF) and a fault (Silver Creek Fault) blocking groundwater. Dashed rectangle (zoomed in the bottom left) highlights the southernmost extension of creep on the HF (inset).

Results

Figure 2.23.1a shows the mean horizontal velocity projected into HF-CF parallel motion (N32°W). Both short- (creep) and long-wavelength (strain accumulation) signals are resolved.

The gradient map locates the creeping fault traces of HF and CF (Figure 2.23.1b) and shows that creep on the HF continues 15 km farther south than the southernmost alignment arrays and mapped active trace (*Lienkaemper*, 2008) in the city of Fremont (Figure 2.23.1b), revealing new potential for rupture

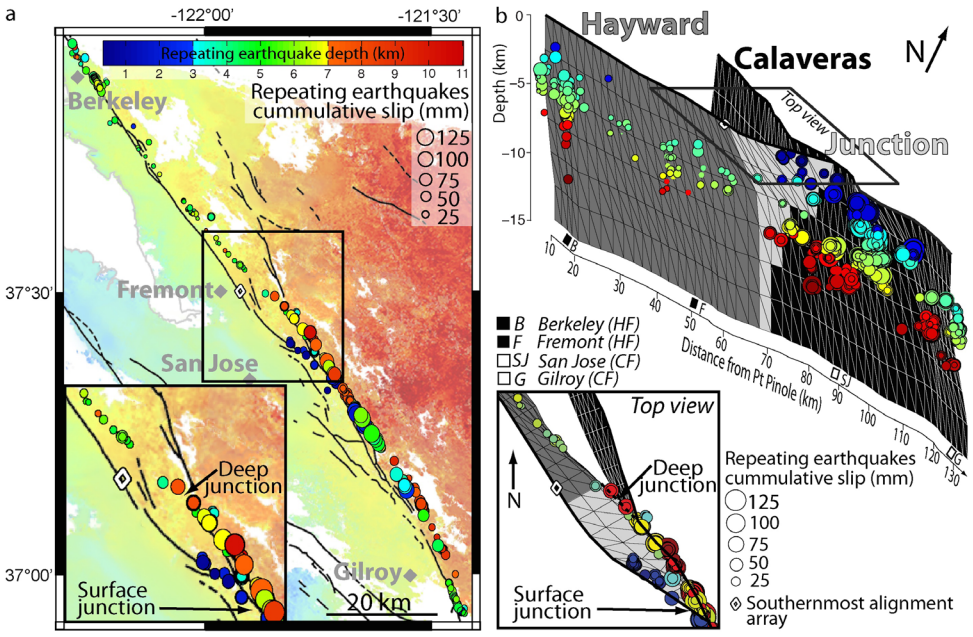

Figure 2.23.2: a) CREs color-coded by depth with radius proportional to their 1992-2011 cumulative slip, overlaying the mean InSAR ground velocity. Shallow CREs (blue) confirm the southward continuation of the HF surface creep and the surface junction with the CF. Continuous CREs between the CF and HF illuminate the junction at depth 10 km north of the surface junction. The black box (bottom left inset) enlarges the region of the junction. b) Model of the refined geometry of the HF (grey) and CF (black). The light grey mesh highlights the newly established connection.

and damage. This southernmost HF span bends southeastward and appears to merge with the CF near 37°21'26"N (black star on Figure 2.23.1). This creep south of Fremont has likely been missed due to its occurrence in vegetated hillsides (Figure 2.23.1b).

We constrain the 3D geometry of the linking fault structure between the HF and CF using the CREs (Figure 2.23.2a). The shallow CREs (blue) align well with the southernmost section of the creeping HF, confirming surface connection. Intermediate-depth CREs (>3 km) occur along a continuous plane ~10 km farther north, illustrating the junction's depth (Figure 2.23.2) in agreement with previous works (e.g. *Andrews et al.,* (1998)). We develop a model of the 3D geometry of the junction with surface traces based on gradient maps and dips derived from CRE locations (Figure 2.23.2b). This new model argues for a direct connection via a dipping wedge-shaped fault plane. A combination of space geodesy and seismology can illustrate the structure of active faults.

The HF and CF should be treated as a single, continuous structure with potential for earthquake ruptures propagating across and generating events with magnitudes much larger than M7, especially given that creeping patches may participate in a rupture in the presence of dynamic weakening (*Noda and Lapusta,* 2013*).*

Acknowledgments

We thank NASA for support through grant NNX12AQ32G and the U.S. Geological Survey National Earthquake Hazards Reduction Program (NEHRP) for support through grants G12AP20096 and G13AP00035.

References

Andrews, D.J., Oppenheimer, D.H., and Lienkaemper, J. J. The Mission Link Between the Hayward and Calaveras Faults, *Journal of Geophysical Research*, 98(B7), 12083–12095, 1993.

Berardino, P., Fornaro, G., Lanari, R. & Sansosti, E. A new algorithm for surface deformation monitoring based on small baseline differential SAR interferograms. *IEEE Trans. Geosci. Remote Sensing* 40, 2375–2383, doi:10.1109/TGRS.2002.803792, 2002.

Fattahi, H. & Amelung, F. InSAR uncertainty due to orbital errors. *Geophys. J. Roy. Astr. S.,* 199, 549–560, doi:10.1093/gji/ggu276, 2014.

Lienkaemper, J. J. Digital database of recently active traces of the Hayward Fault, California. U.S. Geological Survey Data Series 177, version 1.1. http://pubs.usgs.gov/ds/2006/177/, 2006, revised 2008.

Nadeau, R. M. M. & Johnson, L. R. Seismological studies at Parkfield VI: Moment release rates and estimates of source parameters for small repeating earthquakes. *Bulletin of the Seismological Society of America,* 88, 790–814, 1998.

Noda, H. & Lapusta, N. Stable creeping fault segments can become destructive as a result of dynamic weakening. *Nature,* 493, 518–521, doi:10.1038/nature11703, 2013.

Schmidt, D. A., Bürgmann, R., Nadeau, R. M. M. and d'Alessio, M. Distribution of aseismic slip rate on the Hayward fault inferred from seismic and geodetic data. *Journal of Geophysical Research-Solid Earth,* 110, doi:10.1029/2004JB003397, 2005.

Shirzaei, M. & Bürgmann, R. Time-dependent model of creep on the Hayward fault from joint inversion of 18 years of InSAR and surface creep data. *Journal of Geophysical Research-Solid Earth*, 118, 1733–1746, doi:10.1002/jgrb.50149, 2013.

Waldhauser, F. & Schaff, D. P. Large-scale relocation of two decades of Northern California seismicity using cross-correlation and double-difference methods. *Journal of Geophysical Research-Solid Earth*, 113, doi:10.1029/2007JB005479, 2008

24 Interseismic Coupling and Refined Earthquake Potential on the Hayward-Calaveras fault zone

Estelle Chaussard, Roland Bürgmann, Heresh Fattahi, Christopher W. Johnson, Robert M. Nadeau, Taka'aki Taira, and Ingrid Johanson

Abstract

Evaluation of interseismic strain accumulation and fault creep traditionally relies on GPS and alignment arrays that provide precise but spatially sparse measurements. Here, we resolve interseismic deformation associated with the Hayward and Calaveras Faults (HF and CF) in the East San Francisco Bay Area by using InSAR. We estimate the long-term slip rates by inverting the long-wavelength deformation and the shallow slip due to creep by inverting the remaining velocity field. The slip distribution reveals the locations of partially locked patches with potential for a M6.8±0.3 on the HF near San Leandro, a M6.6±0.2 on the northern CF near Livermore, a M6.5±0.1 on the HF south of Fremont, and a M6.2±0.2 near Morgan Hill on the central CF. Cascading multi-segment ruptures could produce a M6.9±0.1 on the HF (from Berkeley to the CF junction), a M6.6±0.1 on the northern CF, a M6.9±0.2 on the central CF (from the junction to Gilroy), and a M7.1±0.1 with a joint rupture of the HF and central CF.

Method

Reassessing earthquake potential requires precise characterization of the long-term slip rates (loading rates) and of the shallow slip rates due to creep. We first use over 250 SAR of the ERS1-2 and Envisat satellites to resolve the 1992-2011 interseismic InSAR velocity field (*Chaussard et al.*, 2015). Then we invert the long-wavelength for long-term slip rates on deep dislocations (3000 km vertical faults below the locking depth of 12.5 km, (*Bürgmann et al.*, 2006)), masking the near-fault velocity (creep). We then use the InSAR fault-parallel motion , corrected for deformations from the deep-dislocation model (i.e., inversion of the residuals of Figure 2.23.1) to invert for shallow slip distribution (above the locking depth). We use the geometry of the Hayward-Calaveras fault zone (HCFZ) from *Chaussard et al.* (2015) and perform a least-squares inversion with smoothness and positivity constraints for uniform slip on triangular dislocation elements in a homogeneous elastic half-space (*Meade*, 2007). A smoothing constraint is imposed using a Laplacian operator and the best fitting model is chosen based on the agreement between the slip rates on surface patches and the measured slip at alignment arrays (AAs).

Results

The deep dislocation model derived from the InSAR mean velocity field agrees well with the data (Figure 2.23.1 top row) and provides sufficient constraints, the addition of GPS data did not provide additional constraints (Figure 2.23.1 bottom row). The long-term slip rates obtained do not differ significantly from previous works using InSAR, GPS, and geology.

The shallow slip distribution of the preferred model (good fit to the data and best agreement between slip on surface patches and observed by AAs creep) is shown in Figure 2.23.2. The view facing the HF (top) reveals similar features to previous models of the HF; a slow creeping patch near Berkeley (~3 mm/yr), a locked patch beneath San Leandro, and a fast creeping patch near Fremont (~9 mm/yr) (*Schmidt et al.,* 2005*; Shirzaei and Bürgmann,* 2013). The view facing the CF (bottom) reveals a locked patch on the northern CF north of Livermore, a slow creeping patch south of Livermore (~3 mm/yr), and two fast creeping patches on the central CF (>12 mm/yr) south of San Jose and Morgan Hill, separated by a slower patch (~9 mm/yr). Most of the slip is limited to the shallowest 5 km on the HCFZ which is in agreement with the locations of historical earthquakes and of microseismicity (Figure 2.23.2).

Considering the time since the last earthquakes and the differences between long-term and shallow slip rates (slip predictable approach), we evaluate that the slow creeping patches (white dashed lines on Figure 2.23.2) near San Leandro could produce a M6.8±0.3, a M6.6±0.2 north of Livermore, a M6.5±0.1 near Fremont, and a M6.2±0.2 near Morgan Hill. Given the direct connection between the HF and CF and the quasi-continuous locking at depths >5 km, there is potential for cascading multi-segment ruptures. To this day the HF could produce a M6.9±0.1 from Berkeley to Fremont, the north CF a M6.6±0.1, central CF a M6.9±0.2 for a rupture ending in Gilroy, and a joint rupture involving the CF and the HF could produce a M7.1±0.1 or larger if propagating north of Berkeley on the HF, or south of Gilroy on the CF.

Acknowledgments

We thank NASA for support through grant NNX12AQ32G and the U.S. Geological Survey National Earthquake Hazards Reduction Program (NEHRP) for support through grants G12AP20096 and G13AP00035.

References

Bürgmann, R., G. Hilley, A. Ferretti, and F. Novali, Resolving vertical tectonics in the San Francisco Bay Area from permanent scatterer InSAR and GPS analysis, *Geol*, 34(3), 221, doi:10.1130/G22064.1, 2006.

Chaussard, E., R. Bürgmann, H. Fattahi, R. M. Nadeau, T. Taira, C. W. Johnson, and I. Johanson, Potential for larger earthquakes in the East San Francisco Bay Area due to the direct connection between the Hayward and Calaveras Faults, *Geophys. Res. Lett.*, 42, doi:10.1002/2015GL063575, 2015.

Meade, B. J., Algorithms for the calculation of exact displacements, strains, and stresses for triangular dislocation elements in a uniform elastic half space, *Computers & Geosciences*, 33(8), 1064–1075, doi:10.1016/j.cageo.2006.12.003, 2007.

Schmidt, D. A., R. Bürgmann, R. M. M. Nadeau, and M. d'Alessio, Distribution of aseismic slip rate on the Hayward fault inferred

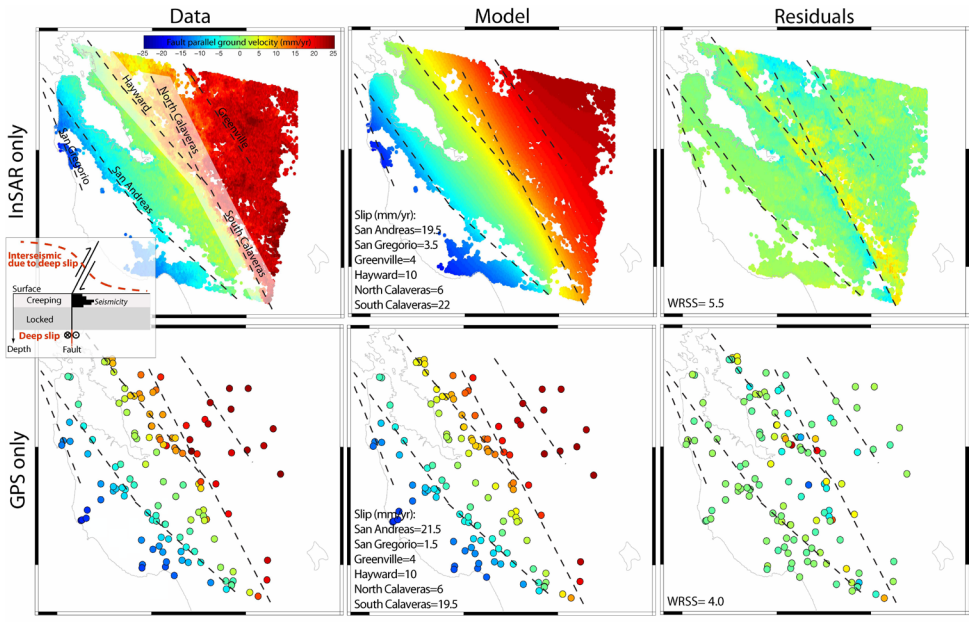

Figure 2.23.1: Deep dislocation model. Dashed lines indicate the surface projection of the 3000 km deep vertical dislocations, based on Bürgmann et al. (2006). Top: inversion based on InSAR, bottom on GPS. The near-fault velocity field (white overlay) is masked for the inversion. The residual velocity field, dominated by deformation due to shallow fault creep, is used for the inversion of shallow slip (Figure 2.23.2).

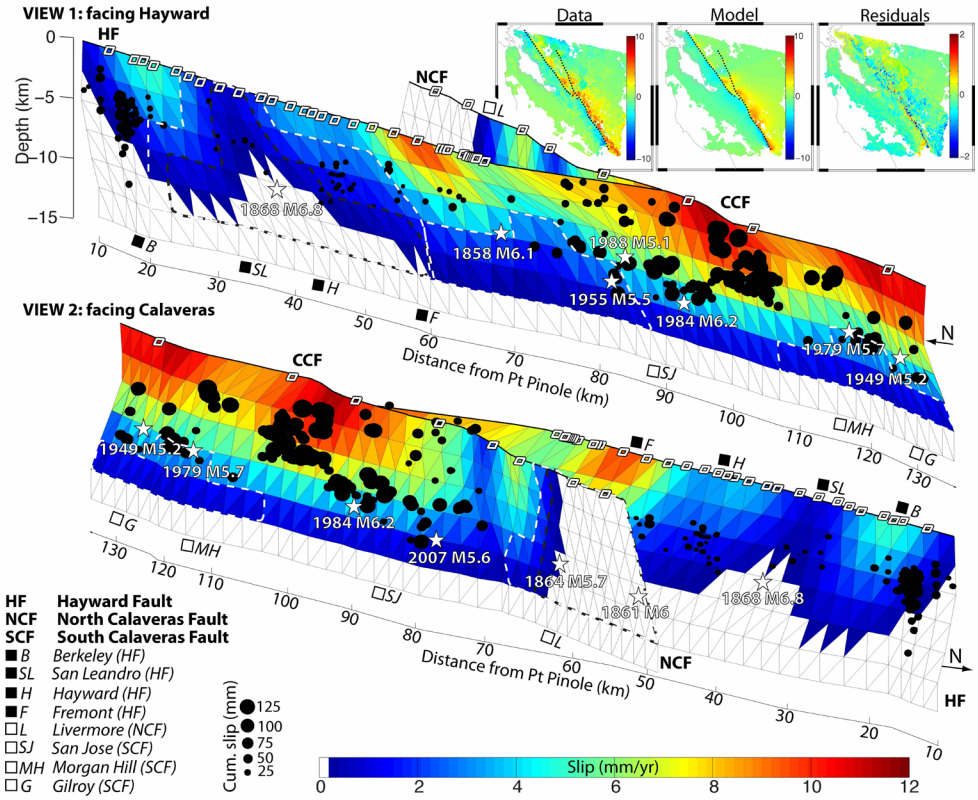

Figure 2.23.2: Shallow slip distribution on the HCFZ. Top view: north toward the left (facing HF), bottom view: north toward the right (facing CF). Black dots are repeating earthquakes with their size proportional to 1992-2011 slip, white stars are historical earthquakes, and white diamonds show the AA locations. The black dashed lines are locked patches (<1mm/yr) and the white dashed lines low slipping patches (<3 mm/yr).

from seismic and geodetic data, *Journal of Geophysical Research-Solid Earth*, 110(B8), doi:10.1029/2004JB003397, 2005.

Shirzaei, M., and R. Bürgmann, Time-dependent model of creep on the Hayward fault from joint inversion of 18 years of InSAR and surface creep data, *Journal of Geophysical Research-Solid Earth,* 118(4), 1733–1746, doi:10.1002/jgrb.50149. 2013..

25 Characteristic Repeating Earthquake Sequences Along the Pacific Trench of Mexico

Luis A. Dominguez and Taka'aki Taira

Introduction

Repeating earthquakes are sequences of events with nearly identical waveforms and hypocenters that are coincident within a resolution of a few meters. Events in repeating earthquake sequences have nearly the same magnitudes and have recurrence intervals that generally vary in proportion to the inverse of the aseismic slip rate on the fault where the repeating earthquakes are located (*Nadeau and Johnson*, 1998; *McEvilly*, 2004). The location, magnitude and recurrence interval properties of the sequences can be used to infer the spatial and temporal distribution of deep aseismic slip rates that are continually loading the asperities of the sequences to repeated failure. In effect, the sequences can act as creep meters at seismogenic depths, which may improve our understanding of how large damaging earthquakes may nucleate.

We systematically examine 14 years of waveform records (from 2001 through 2014) to identify repeating earthquakes along the flat subducting segment of the Cocos plate (Central Mexico). A significant number (>300) of possible sets of events with highly correlated features (correlation coefficient (cc) >0.95 and spectral coherency (coh) >0.95) have been found between the trench line and the 20 km iso-contour of the subducting slab. The reported set of correlated waveforms shows a well-defined clustering in space and a marked increase of repeating earthquake activity after the M7.5 2012, Ometepec earthquake. A long-term temporal behavior of repeating earthquakes in Mexico will provide key constraints on better understanding of the earthquake cycle at the plate interface.

Diversity of Earthquakes in Mexico

Several transient mechanisms, such as slow slip events, tremors, and very low frequency earthquakes have been reported in Mexico (*Rivet et al.,* 2013). For instance, it is well known that a larger segment of the trench known as the Guerrero Gap (indicated in Figure 2.25.1) has not ruptured in a large megathrust event for the past 100 years. This area coincides with the rupture zones of reported slow slip events in the past 15 years and the location of a significant number of repeating earthquakes reported in this study. We here search for repeating earthquakes to examine spatio-temporal variation of slip budgets in the subduction of the Cocos Plate as different transient phenomena are continuously loading and unloading stress along asperities in an area where megathrust earthquakes occur. Tracking the behavior of repeating earthquakes activity provides a tool to examine how creeping is affected or not by the interaction between earthquakes, slow slip events and tremors.

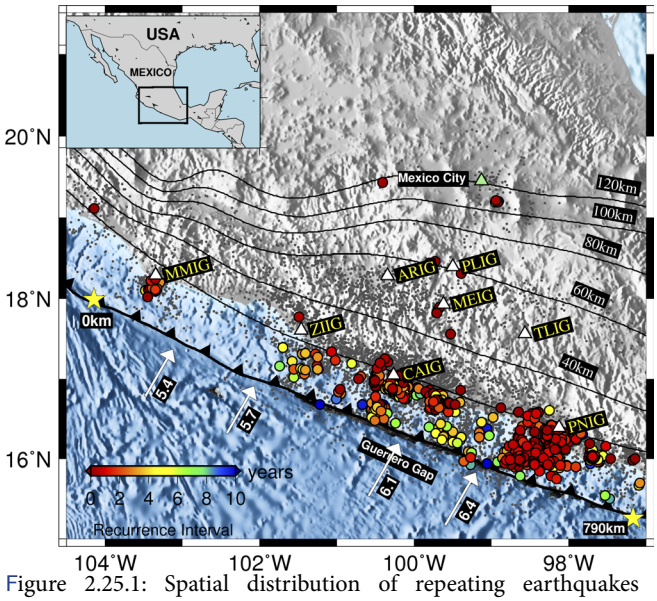

Figure 2.25.1: Spatial distribution of repeating earthquakes in Mexico. Stars indicate the reference points along the trench used in Figure 2.25.2. Colorscale shows the recurrence time for each event pair. Black lines indice the depth of the subducting slab (*Pardo et al.*, 1995). Triangles show the location of the stations used in this study, and gray dots show the seismicity reported in the area.

Methods and Results

A search of characteristic repeating sequences was performed by comparing all possible pairs of events reported by the Mexican Seismological Service within the study area. We analyzed data from eight permanent stations at a maximum distance of 200 km from the coast. Figure 2.25.1 indicates the spatial distribution of the waveform pairs with highly correlated waveforms. The magnitudes of the repeating earthquakes range from M3.1 to M4.5. The recurrence intervals between each repeater vary within a few a minutes up to 12 years. We also observed a large gap of seismic activity between station MMIG and ZIIG, where no repeaters were found. There is a sharp increase in repeater seismic activity near station PNIG, mainly after the 2012 M7.5 Ometepec earthquake.

Figure 2.25.2 shows the temporal distribution of the repeating earthquakes as a function of distance along the trench (reference points are shown with stars in Fig. 2.25.1). Shadowed areas indicate the occurrence of slow slip events, usually located inland north of the region where repeating events occur, and green bars show the rupture lengths of earthquakes >M6.0 that commonly rupture along the reported repeating earthquakes.

Conclusions

We have found strong evidence of the occurrence of characteristic repeating earthquakes. Our analysis finds that

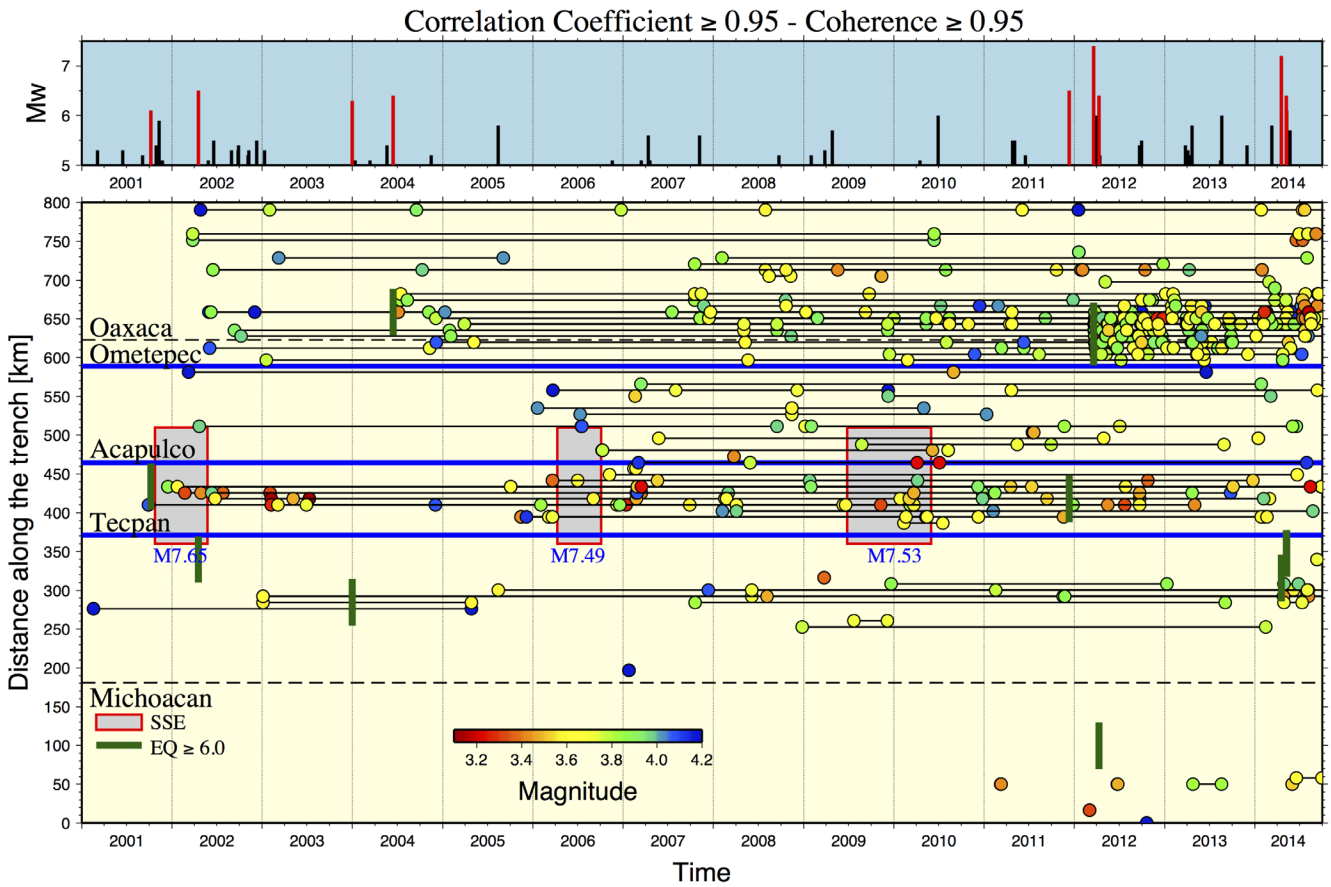

Figure 2.25.2: Temporal distribution of earthquakes along the trench. Distance along the trench reference points are indicated in Figure 2.25.1. Interconnected circles show pairs of events with high correlation coefficients (cc>0.95) and high coherency (coh>0.95). Shadow areas indicate the temporal occurance of slow slip events (SSEs), and green bars show the rupture length of earthquakes larger than M6.0. The overhead plot shows the earthquake catalog for events M>5.0.

characteristic repeating earthquakes happen to occur at shallow depths (<20 km), where large megathrust earthquake nucleate. Spatial clustering of the events suggests changes in seismic coupling along the trench, while highly variant recurrence times may indicate variations in the loading and unloading of stress during the inter-seismic period.

Acknowledgements

This project is funded by the UC-MEXUS grant CN-1443. We also want to thank the Mexican Seismological Service for proving the data and for the maintenance of the permanent seismological network of Mexico.

Reference

Nadeau, R. M., and L. R. Johnson (1998), Seismological studies at Parkfield VI: Moment release rates and estimates of source para-meters for small repeating earthquake, *Bull. Seismol. Soc. Am.*, 88(3), 790–814.

Nadeau, R. M., and T. V. McEvilly (2004), Periodic pulsing of characteristic microearthquakes on the San Andreas fault, *Science*, 303(5655), 220–222, doi:10.1126/science.1090353.

Pardo, M., and G. Suárez (1995), Shape of the subducted Rivera and Cocos plates in southern Mexico: Seismic and tectonic implications, *J. Geophys. Res.*, 100, 12,357–12,373.

Rivet, D., Campillo, M., Radiguet, M., Zigone, D., Cruz-Atienza, V., Shapiro, N., Kostoglodov, V., Cotte, N., Cougoulat, G., Walpersdorf, A., Daub, E. (2013), Seismic velocity changes, strain rate and non-volcanic tremors during the 2009-2010 slow slip event in Guerrero, Mexico, *Geopys. Journal Int*, 196(1), 14, doi: 10.1093/gji/ggt374.

26 Fifteen Years of Surface Deformation in Western Taiwan: Insight from SAR Interferometry

Mong-Han Huang (JPL), Roland Bürgmann, Jyr-Ching Hu (National Taiwan University)

Introduction

Geodetically measured surface displacements are produced by a combination of underlying deformation processes acting at different spatial and temporal scales. A complete history of surface measurements in an area can help discriminate different types of deformation due to different sources, including tectonic, hydrologic and human. In this study, which includes the active mountain front and adjacent coastal plain of southwestern Taiwan, we use Synthetic Aperture Radar (SAR) images from 1995 to 2001 and from 2005 to 2009 to generate time series of surface deformation based on a modified InSAR small baseline method. This result shows significant range increase in line of sight (LOS) that is dominated by land subsidence in the coastal area in W and SW Taiwan, and is highly correlated with annual precipitation. In SW Taiwan, LOS increase is associated with the southwestward structural escape due to the tectonic loading from the Philippine Sea Plate. The estimated LOS velocity based on continuous GPS measurements of 3D displacements between 2006 and 2009 generally agrees with InSAR. Fifteen years of surface deformation history would allow us to identify the spatial patterns of seasonal versus long-term deformation in SW Taiwan. The seasonal displacement is mainly associated with groundwater recharge and withdrawal, whereas the long-term deformation may indicate long-term tectonic loading in SW Taiwan during the interseismic period of the earthquake cycle, including elastic strain along or continuous creep on the active faults. These results are potentially useful for evaluating seismic hazards.

Data and Method

We use SAR images from European Remote Sensing (ERS) 1 and 2 and Environment Satellite (Envisat) satellites developed by the European Space Agency (ESA). We use 40 ERS SAR acquisitions between 1995 and 2001, and 21 Envisat ASAR acquisitions between 2004 and 2009. For both ERS and Envisat datasets, acquisitions of track 232 and frames 3123-3159 (Figure 2.26.1) cover most of western Taiwan, and the satellite look direction is ~N70°W and look angle is ~23.5°. We obtain floating scenes (frames 3123, 3141, and 3159) for the ERS datasets and floating pass for the Envisat dataset. The vegetated and topographically rough terrains of Taiwan make the conventional InSAR to be challenging, so in order to maintain the quality of interferograms we only process interferograms that have relatively small spatial (< 200 m) and temporal (< 2.5 years) baselines. We estimate the point scatterers of interferograms and their time series are based on a modified small baseline subset (SBAS) algorithm (*Berardino et al.,* 2002).

Result

The result of mean crustal deformation in different decades

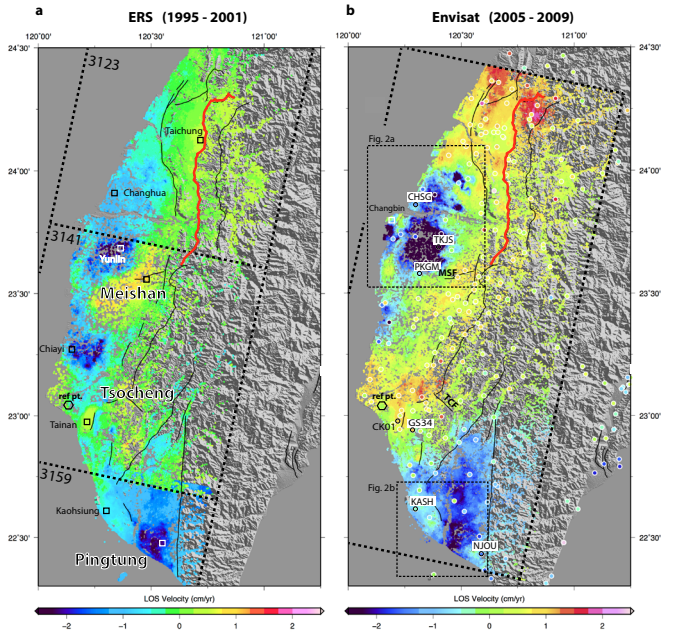

Figure 2.26.1: Mean annual line of sight (LOS) velocity during (a) 1995-1999 (before the 1999 M_w 7.6 Chi-Chi earthquake) and (b) 2005-2009. Positive LOS velocity means range decrease and negative means increase. White circles are continuous GPS and color in the circles are converted LOS velocity.

is shown in Figure 2.26.1. In both 1996-2001 and 2005-2009 time periods, there is higher surface uplift near Meishan and Tsocheng. The seismicity in western Taiwan also shows shallow (<10 km) seismicity between the Meishan and the Tsocheng faults. The two high surface uplift regions locate roughly at the northern and southern ends of shallow seismicity. The source of the seismicity and surface uplift may be due to change of foreland basin depth in western Taiwan and stress loading from the Philippine Sea plate. In Pingtung, the range increase (blue region in Figure 2.26.1) is mainly the result of southwestward horizontal displacement due to tectonic escape.

Figure 2.26.2 shows close-ups of Figure 2.26.1 with relevant color scales for the land subsidence areas in W and SW Taiwan, respectively. Our InSAR result agrees well with the CGPS measurements, but InSAR can further characterize the land subsidence spatial distribution and size. In Figure 2.26.2b, InSAR result reveals land subsidence in the regions without GPS station coverage such as western Yunlin (Mailiao), which was developed on landfill since the late 1990s.

Figure 2.26.3 compares time series of InSAR and precipitation. This result shows some correlation between surface deformation and precipitation with a time delay, especially in sites in Yunlin, Chiayi, and Pingtung. The time delay between surface deformation and precipitation in Figure 2.26.3 shows a ~4 month lag in Yunlin, ~3.5 months in Chiayi, ~2 months in Kaohsiung, and ~3 months in Pingtung, whereas no significant

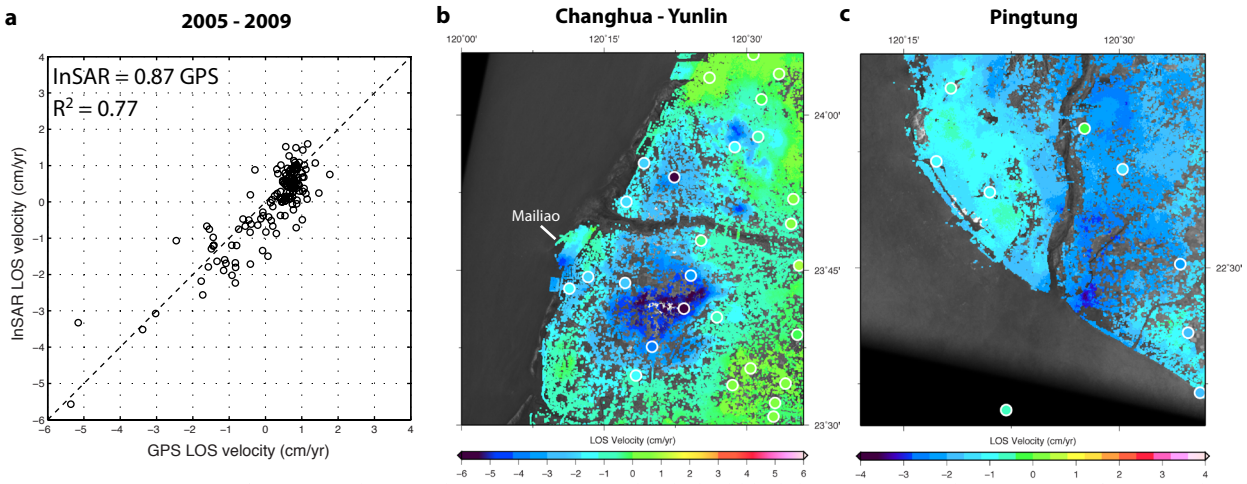

Figure 2.26.2: (a) Comparison of InSAR and CGPS during 2006-2009. The dashed black line represents the one-to-one function. (b) Close-up of Figure 2.26.1b showing land subsidence in western Taiwan (Changhua and Yunlin) and (c) Pingtung Plain.

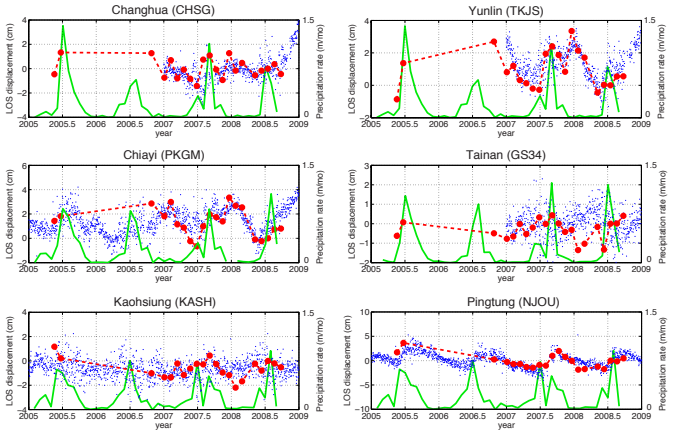

Figure 2.26.3: Comparison of InSAR (red dots), GPS (blue dots), and precipitation data (green lines). Note the long-term InSAR and GPS mean LOS velocities are removed. The name in the parentheses is the CGPS station name (see Figure 2.26.1b for location)

time delay is observed in Changhua and Tainan. The time delay indicates different hydraulic conductivity in different regions in western Taiwan and may imply a change of aquifer system and sediment property in the Western Plain. However, we do not have a complete set of groundwater well time series and precipitation data to investigate relationships between ground surface and hydraulic head.

Summary

We investigate crustal deformation in western Taiwan during 1995-2001 and during 2005-2009 based on a modified SBAS InSAR method. Our results reveal regions with satellite range increase in the coastal area due to land subsidence, and in the Pingtung Plain due to tectonic escape. Chiayi (near the Meishan fault) is undergoing tectonic uplift related range decrease, whereas tectonic escape in the Pingtung Plain also results in range increase. In the Chiayi area, tectonic related surface uplift as well as shallow (<10 km) seismicity reflect continuous slip along the foreland basin due to stress loading from the Philippine Sea Plate.

Mean LOS velocity and seasonality of western Taiwan revealed by InSAR outline anthropogenic water usage and tectonic related deformations, which are important topics for land usage and hazard monitoring. With considering of groundwater and precipitation data, we will be able to estimate storativity and hydraulic conductivity in the sedimentary layers, which is important for groundwater monitoring and management. Besides, longer-term crustal deformation may indicate regional tectonic stress loading and fault creep or locking sections. Investigating fault locking depth and slip in interseismic and coseismic periods from surface deformation observation will help estimate slip budget and thus benefits natural hazard mitigation.

Acknowledgements

The Larsen fellowship and NASA grant NNX12AQ32G supported M.-H. Huang for this study. The ERS SAR images were purchased under NSC 98-2628-M-002-016 and NSC 101-2116-M-002-012, and the Envisat ASAR images are available through ESA project number 28610.

References

Berardino, P., Fornaro, G., Lanari, R., and Sansosti, E., 2002, A new algorithm for surface deformation monitoring based on small baseline differential SAR interferograms. *IEEE Transactions on Geoscience and Remote Sensing*, 40, *2375-2383, doi:10.1109/TGRS.2002.803792.*

27 Lithospheric Rheology Constrained from Twenty-five Years of Postseismic Deformation Following the 1989 M_w 6.9 Earthquake

Mong-Han Huang (JPL), Roland Bürgmann, Fred Pollitz (USGS)

Introduction

The October 17, 1989 M_w 6.9 Loma Prieta earthquake provides the first opportunity to probe the crustal and upper mantle rheology in the San Francisco Bay Area since the 1906 M_w 7.9 San Francisco earthquake. Here we use geodetic observations including GPS and InSAR to characterize the Loma Prieta earthquake postseismic displacements from 1989 to 2013. Pre-earthquake deformation rates are constrained by nearly 20 years of USGS trilateration measurements and removed from the postseismic measurements prior to the analysis. We observe GPS horizontal displacements at mean rates of 1-4 mm/yr toward the Loma Prieta Mountain until 2000, and ~2 mm/yr surface subsidence of the northern Santa Cruz Mountains between 1992 and 2002 shown by InSAR, which is not associated with the seasonal and longer-term hydrological deformation in the adjoining Santa Clara Valley. Previous work indicates afterslip dominated in the early (1989-1994) postseismic period, so we focus on modeling the postseismic viscoelastic relaxation constrained by the geodetic observations after 1994. The best fitting model predicts an elastic 19-km-thick upper crust above an 11-km-thick viscoelastic lower crust with viscosity of 6×10^{18} Pa s, underlain by a viscous upper mantle with viscosity of 2×10^{19} Pa s. The millimeter-scale postseismic deformation does not resolve the viscosity in different layers very well, and the lower crustal deformation may be localized in a narrow shear zone. However, the inferred lithospheric rheology is consistent with previous estimates based on post-1906 San Francisco earthquake measurements along the San Andreas Fault system. The viscoelastic relaxation may also contribute to the enduring increase of aseismic slip and repeating earthquake activity on the San Andreas Fault near San Juan Bautista, which continued for at least a decade after the Loma Prieta event.

Data

We combine GPS in three time periods – *Segall et al.* (2000), *d'Alessio et al.* (2005), and PBO data to construct a 25-year-long postseismic time series. We use the secular motion model by Bürgmann et al. (1997) to remove interseismic deformation in the area (Figure 2.27.1). We use 52 ERS-1/2 SAR descending acquisitions (Track: 70) between 1992 and 2006 and 46 Envisat ASAR descending acquisitions (Track: 70) between 2005 and 2010, which are developed and maintained by the European Space Agency (ESA). We generate interferograms that have less than 250 m perpendicular orbit separation and three years temporal baselines, respectively. We consider a point scatterer to be stable if the phase measurement at that point maintains its spatial correlation higher than 0.4 in at least 50% of all interferograms, and the time series result is shown in Figure 2.27.2.

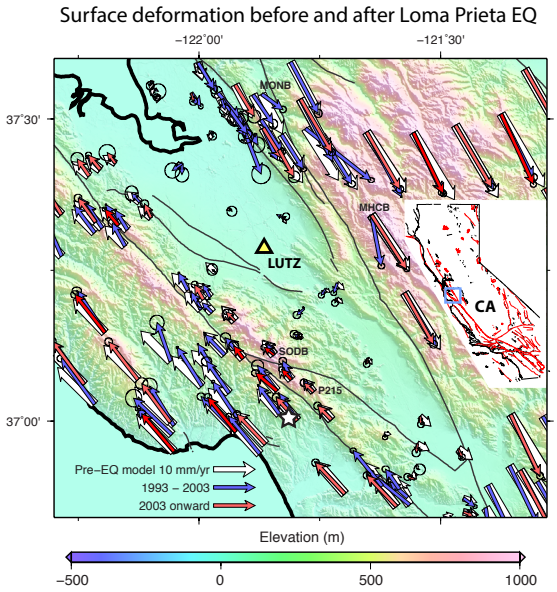

Figure 2.27.1: Geodetic horizontal measurements in the southern San Francisco Bay Area, shown in the blue box in the map. Surface deformation before (white arrows) and after (blue and red arrows) the Loma Prieta earthquake are shown relative to station LUTZ (yellow triangle). The white star indicates the Loma Prieta earthquake epicenter.

Model

We first test the viscoelastic relaxation due to the Loma Prieta coseismic stress change in the lower crust and upper mantle during 1995 – 2014. To explore the rheologic structure, we perform a grid search for different lower-crustal and upper-mantle viscosities, allowed to vary between 10^{16} and 10^{20} Pa s, and compare the model surface deformation with GPS time series during 1995 – 2013 and InSAR time series during 1992 – 2010. Subsequently, we use dislocation models in a layered elastic half-space to calculate afterslip in 1989-1995, 1995-2000, and 2000-present time periods, by inverting the residuals from the viscoelastic model predictions. We invert for distributed afterslip on two fault planes associated with the Loma Prieta fault rupture zone and the Foothills thrust belt, respectively.

Summary

Based on dislocation modeling, afterslip on the fault that ruptured in the earthquake and a buried fault within the Foothill thrust belt dominates the rapid early postseismic deformation. Our modeling using a 1D viscoelastic structure composed of an elastic upper crust and Maxwell viscoelastic lower crust and upper mantle, implies that the viscosities of the lower crust and upper mantle are about 6×10^{18} Pa s and 2×10^{19} Pa s, respectively. A combined afterslip-viscoelastic model can better explain early and late Loma Prieta postseismic deformation,

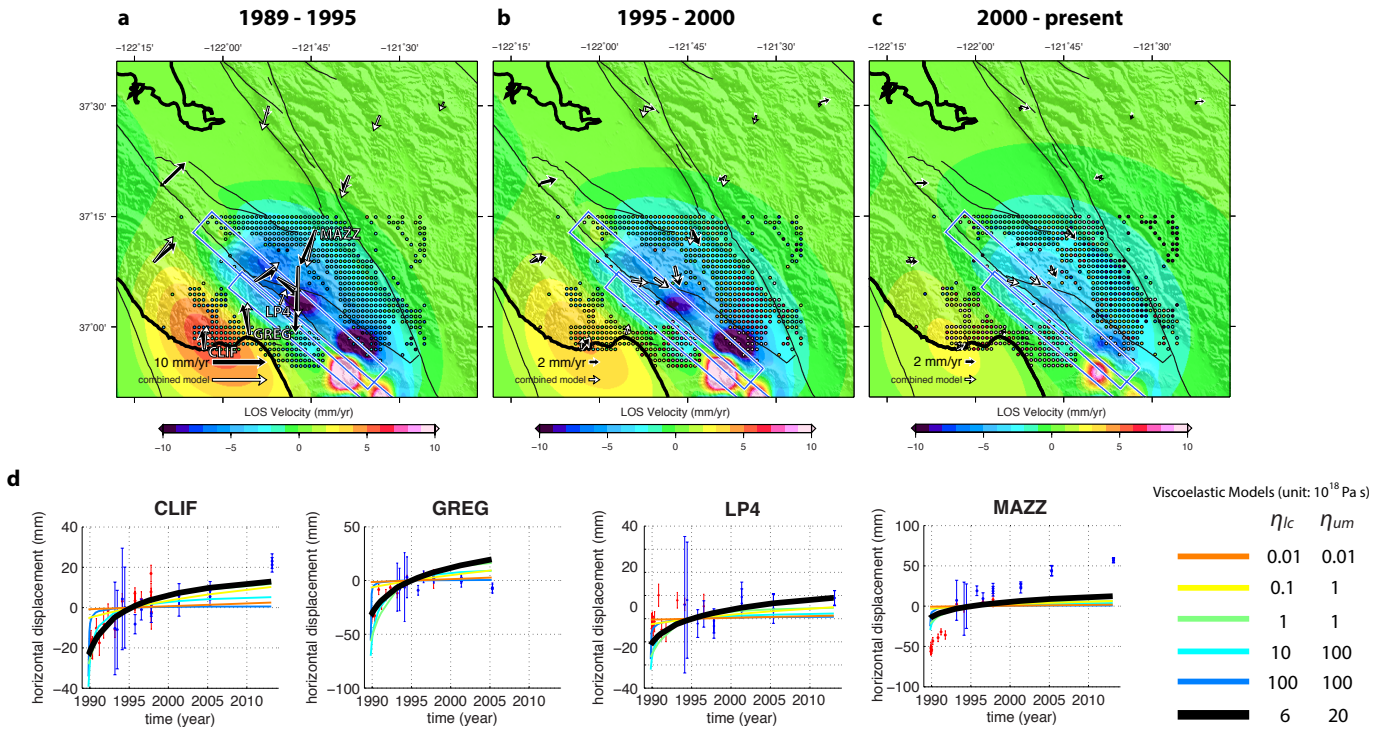

Figure 2.27.3: Viscoelastic relaxation and afterslip combined model fitting to GPS data in (a) 1989 – 1995, (b) 1995 – 2000, and (c) 2000 - present time periods. The black arrows are GPS postseismic displacements, and the white arrows are the multiple-mechanism models in different time periods. The background colors show the predicted relaxation in LOS. (d) Selected GPS time series. The colored lines are viscoelastic relaxation fitting with different lower-crustal and upper-mantle viscosities, and the thick black lines are the best fitting viscoelastic relaxation model

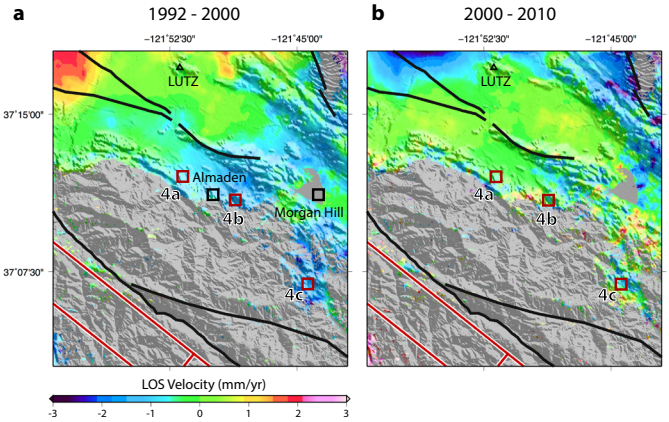

Figure 2.27.2: InSAR line of sight (LOS) velocity during (a) 1992-2000 and (b) 2000-2010. Positive LOS value is range decrease, which represents eastward and/or uplift motion and vise versa. The LOS interseismic secular motion is removed based on Bürgmann et al. (1997), and the velocity is relative to station LUTZ. The black lines are the major fault lines, and the red lines are the coseismic fault geometry.

where the afterslip is reduced in the later period. We do not attempt to identify a transient component of the rheology that might further enhance the contribution of viscoelastic relaxation to the early postseismic deformation. Our geodetic measurements cannot tightly resolve lithospheric viscosity due to the low amount of the postseismic displacement from this M_w 6.9 earthquake and higher data uncertainty in the early 1990s. The enduringly accelerated activity of repeating earthquakes and fault creep on the San Andreas Fault and the Sargent Fault after the Loma Prieta earthquake is coherent in time with the modeled postseismic deformation. This suggests that viscoelastic relaxation drove shallow slip on these creeping faults following the Loma Prieta earthquake.

Acknowledgements

We thank D. Dreger, T. Bodin, I. Johanson, E. Chaussard, C. Johnson, and R. Turner for discussion and constructive suggestions. The ERS and Envisat SAR data are copyrighted by the European Space Agency and were provided through the WInSAR archive at UNAVCO. This project is supported by the National Science Foundation grant (EAR-0951430) and NASA (NXX08AG50G).

References

Bürgmann, R., P. Segall, M. Lisowski, and J. Svarc (1997), Postseismic strain following the 1989 Loma Prieta earthquake from GPS and leveling measurements, *J. Geophys. Res.*, 102, 4933-4955, doi: 10.1029/96JB03171.

d'Alessio, M. A., I. A. Johanson, R. Bürgmann, D. A. Schmidt, and M. H. Murray (2005), Slicing up the San Francisco Bay Area: Block kinematics and fault slip rates from GPS-derived surface velocities, *J. Geophys. Res.*, 110, doi:10.1029/2004JB003496.

Segall, P., R. Bürgmann, and M. Matthews (2000), Time dependent deformation following the 1989 Loma Prieta earthquake, *J. Geophys. Res.*, 105, 5615-5634, doi:10.1029/1999JB900352.

28 3D Surface Deformation of the Slumgullion Landslide from UAVSAR Derived Interferograms

Brent Delbridge, Roland Bürgmann, Eric Fielding, Scott Hensley, William Schulz

Introduction

Resolving the kinematics of landslide deformation is necessary to evaluate the controlling mechanisms. An improved understanding of how landslides respond to environmental changes is essential to hazard mitigation and will have societal, environmental and financial impacts across the globe. Increasing global temperatures are predicted to lead to more frequent and intense precipitation and consequently an increased risk of landslide failure (*Coe*, 2012).

Historically, studies of landslide displacements have been limited to sparse point measurements acquired with labor-intensive terrestrial methods or GPS. The last two decades have seen the rise of space-based repeat-pass Interferometric Synthetic Aperture Radar (InSAR) as an increasingly important tool for the monitoring of active ground deformation, including landslide motion and hillslope creep. The measurement of the full landslide-wide surface deformation allows for the examination of how motion is accommodated between multiple kinematic domains that comprise the landslide, and overcomes the insufficient spatial coverage of traditional GPS point measurements.

In order to address these current limitations, we utilize the unique capabilities of the NASA/JPLs UAVSAR airborne repeat-pass SAR interferometry system to provide surface geodetic measurements with "landslide-wide" spatial coverage, optimal imaging geometries and temporal resolution of our choosing. Unlike traditional InSAR we are not restricted to fixed flight tracks or fixed repeat times, allowing for optimal imaging geometries and timing.

To take full advantage of the unique airborne-geodetic UAVSAR system capabilities we invert for the full 3D surface deformation field at the Slumgullion Landslide in Colorado, USA (Figure 2.28.1). By combining four optimally chosen look directions we are able to extract the full 3D velocity field, with adequate redundancy in the inversion to accurately estimate errors.

Study Site: Slumgullion Landslide

The Slumgullion landslide is a deep-seated landslide located in the San Juan Mountains of southwestern Colorado (Figure 2.28.2). The rapid deformation rates (2 cm/day) and large spatial extent in which to examine the complex interaction of different kinematic elements make the Slumgullion Landslide an ideal target to study landslide mechanics. The currently active portion of the landslide has been deforming for the past 300 years (*Fleming et al.*, 1999) with total displacements on the order of hundreds of meters (*Coe et al.*, 2003). The slide sits on top of an older, inactive landslide deposit which radiocarbon dating suggests failed catastrophically approximately 700 years ago. This catastrophic failure dammed the Lake Fork of the Gunnison River forming the second largest natural lake in Colorado, Lake San Cristobal. The currently active portion of the Slumgullion landslide is measured to be ~3.9 km long and ~300 m wide. Specifically, in this study, we determine the full 3D deformation field across the entire landslide surface to explore how the landslide motion responds to the perturbation by infiltration of seasonal snowmelt.

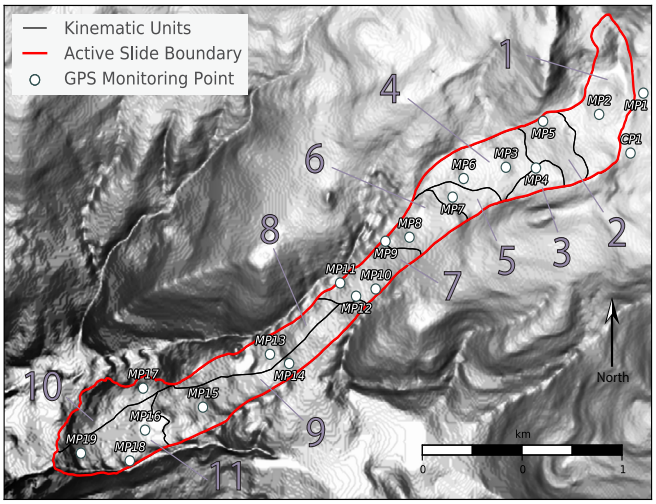

Figure 2.28.1: Shaded relief DEM of the Slumgullion Landslide and surrounding terrain. The 1/3 arcsecond DEM is from the USGSs' National Elevation Dataset (NED). The black lines show the distinct geomorphic domains within the slide as identified by *Schulz et al.* 2012. The circles represent USGS GPS control points used in this study.

UAVSAR interferograms

The NASA/JPL UAVSAR airborne repeat-pass SAR interferometry system is flown aboard a NASA Gulfstream III and is capable of acquiring L-Band (24 cm wavelength) SAR images with a resolution of 1.9 m in range and 0.8 m in the azimuth direction (*Hensley et al.*, 2009). The UAVSAR system was designed by NASA's Earth Science Technology Office (ESTO) Instrument Incubator Program (IIP) with its primary focus on providing repeat-pass radar interferometry at a variety of timescales and optimal imaging geometries in order to provide precise measurements of Earth's surface deformation.

3D Vector Inversion

To obtain the full 3D vector displacement field we combine the LOS measurements from the four flight lines. We first prepare each LOS interferogram by fitting and removing a plane to remove residuals due to baseline errors. We then normalize the phase from each interferogram to a common time interval to account for differences in the duration and acquisition times. The LOS vector is then estimated for each pixel using a

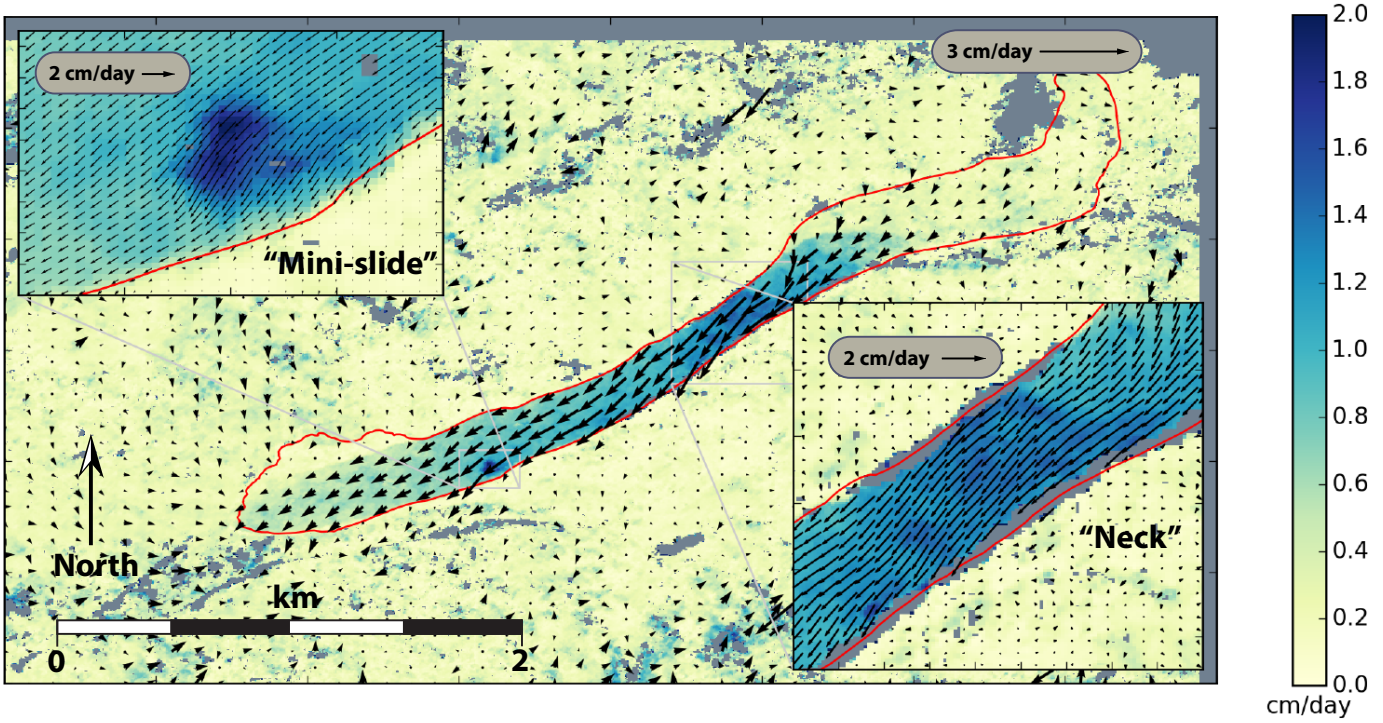

Figure 2.28.2: Horizontal velocity vectors corresponding to the results of the 3D vector inversions. The magnitude of the total velocities are shown with color ranges from yellow to blue corresponding to velocities ranging from 0 to 2 cm/day. The gray regions denote masked out regions of low coherence. The black arrows represent a downsampled representation of the same inverted horizontal velocity field. The inset in the top left corner shows a 7-times zoomed detail of a local failure we denote as the "mini-slide." The inset in the bottom right corner shows a 3-times zoomed detail of the steep and narrow landslide neck.

DEM for the region and the acquisition flight parameters and geometry. The covariance for each pixel is estimated from the correlation matrix and we perform a least squares inversion for the displacement. The desired displacement vector is expressed in terms of the natural physical coordinates North, East, and Up.

Acknowledgements

This work was generously supported by NSF grant 3928423049, and NSF GRFP Fellowship 923843294.

References

Coe, J. A. (2012), Regional moisture balance control of landslide motion: Implications for landslide forecasting in a changing climate, *Geology*, 40, 323–326.

Coe, J. A., Ellis, W. L., Godt, J. W., Savage, W. Z., Savage, J. E., Michael, J. A., Kibler, J. D., Powers, P. S., Lidke, D. J., and Debray, S. (2003), Seasonal movement of the Slumgullion landslide determined from global positioning system surveys and field instrumentation, July1998-March 2002, *Engineering Geology*, 68, 67-101.

Fleming, R., Baum, R., and Giardino, M. (1999), Map and description of the active part of the Slumgullion landslide, Hinsdale County, Colorado, *Open-file Report, US Department of the Interior*, US Geological Survey.

Hensley, S., Zebker, H., Jones, C., Michel, T., Muellerschoen, R., and Chapman, B. (2009), First deformation results using the nasa/jpl uavsar instrument, *Synthetic Aperture Radar*, APSAR 2009. 2nd Asian-Pacific Conference, IEEE, 1051–1055.

Schulz, W., Coe, J., Shurtleff, B., Panosky, J., Farina, P., Ricci, P. P., and Barsacchi, G. (2012) Kinematics of the Slumgullion landslide revealed by ground-based InSAR surveys, *Landslides and Engineered Slopes, Protecting Society through Improved Understanding*, Taylor & Francis Group, London, 1273-1279.

29 Seasonal Deformation of Slow Moving Earth Flows Characterized by InSAR Tracking in the Berkeley Hills, California

Julien Cohen-Waeber (LLNL), Estelle Chaussard, Roland Bürgmann, Nicholas Sitar, Alessandro Ferretti

Introduction

Technologies such as continuous Global Positioning Systems (GPS) and Interferometric Synthetic Aperture Radar (InSAR) are capable of measuring active surface displacement with as much as sub-centimeter precision and accuracy. GPS tracking of discrete points in real time is common and reliable. InSAR allows widespread surface deformation tracking. These technologies are complementary and lend themselves to numerous geological engineering applications including the characterization and tracking of subsidence, seismically induced crustal deformation, or in this case landslides.

Active landsliding in the San Francisco East Bay hills (Berkeley Hills) has been the object of many investigations over recent decades. Studies suggest a trend in landslide mobility is associated with regional climate and active tectonic conditions in addition to the local geologic setting (*Alan Kropp and Associates* 2002, *Hilley et al.* 2004, *Quigley et al.* 2010), though their mechanisms are still poorly understood.

The intent of this research is to help develop a method for the remote evaluation of general landslide hazards. We explore here the precipitation triggered seasonal deformation of the Blakemont landslide.

InSAR Time Series

A review of three InSAR time series analyses of the Blakemont landslide, from separate satellite acquisitions and over different time intervals from 1992-2011 shows remarkable consistency (*Hilley et al.* 2004, *Quigley et al.* 2010). In each case, surface deformation showed a clear correlation to precipitation, with similar mean downslope velocities (approx. 30 mm/year) and periods of acceleration during each wet season. These studies also suggest observable internal deformation with different sections mobilizing separately (*Quigley et al.* 2010, *Cohen-Waeber et al.* 2013).

In this study, the observed displacement trends were confirmed using TerraSAR-X data acquisitions from 2009-2014 and analyzed using the SqueeSAR™ algorithm by Tele-Rilevamento Europa (*Ferreti et al.,* 2011). Higher spatial resolution reveals that these slides are in fact moving as bodies of smaller coherent masses with variable phases and velocities. A shorter acquisition return period also reveals a clearly seasonal trend in the displacement time history of all data points (on or off landslides) with annual fluctuations following a general sinusoidal function. Figure 2.29.1 (top) illustrates the spatial variability in annual velocity of smaller coherent masses and (bottom) landslide acceleration with precipitation and seasonal sinusoidal fluctuations.

Seasonality Study of Ground Deformation

To characterize the observed seasonality at Blakemont landslide, a Linear Regression Analysis was performed. Temporal variability of the displacement time histories for all data points fit a general Sine wave function (Equation 29.1) well (Figure 2.29.2, top). Mapping the modeled seasonal amplitude across the study area (Figure 2.29.2, bottom), areas of steeper slope show higher amplitude, though it is difficult to distinguish the landslide (red outline) from the surrounding slopes.

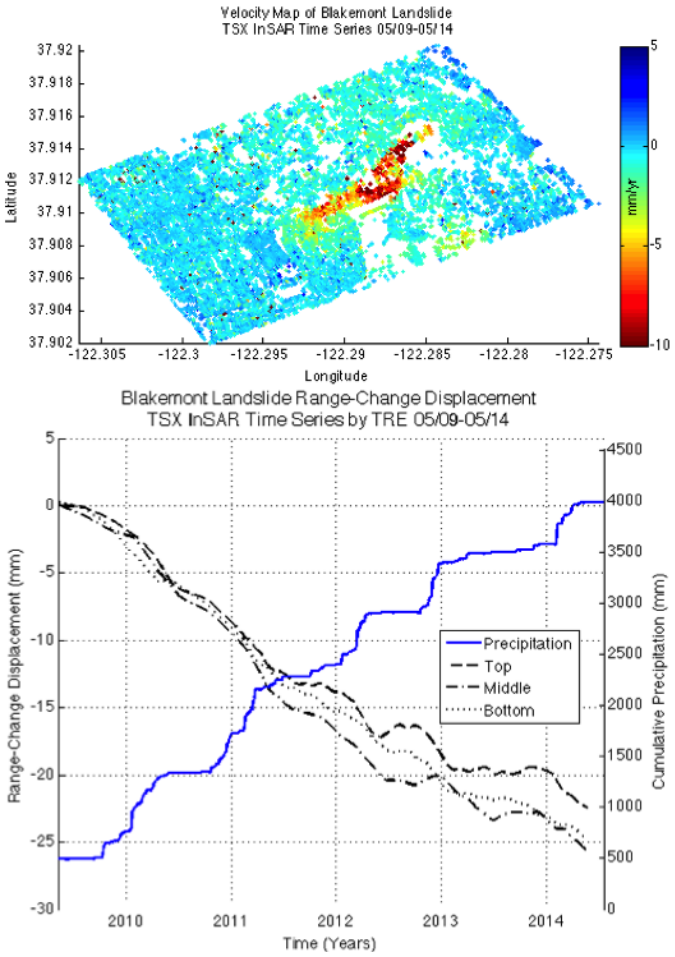

Figure 2.29.1: (Top) velocity map of Blakemont landslide illustrating spatial variability in annual velocity of smaller coherent masses and (bottom) displacement time history of the top, middle and bottom of Blakemont landslide illustrating acceleration with precipitation and seasonal sinusoidal fluctuations.

$$y(t) = A + Bt + Ct^2 + Dsin(2\pi t) + Ecos(2\pi t) \quad (29.1)$$

To isolate different temporal variability patterns of the recorded time histories, a Principal Component Analysis (PCA) was performed (*Bjornsson and Venegas,* 1997). PCA is a generalized eigenvalue problem in which linear combinations are formed from the measured variables to extract their principal

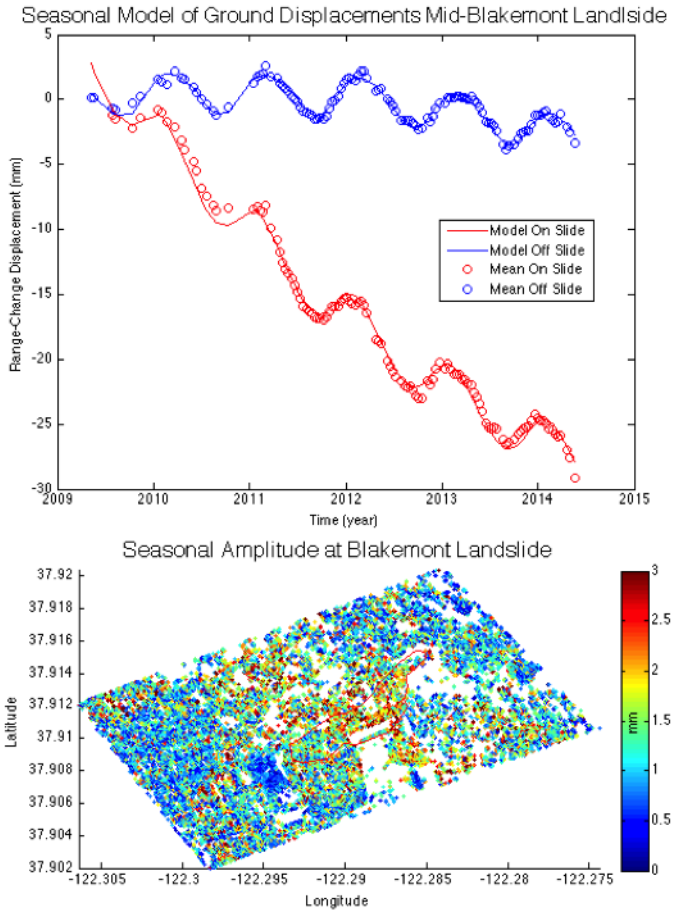

Figure 2.29.2. (Top) linear regression analysis of average displacement time histories for areas on and off Blakemont landslide, illustrating a close fit between the data and a sinusoidal model and (bottom) modeled seasonal amplitude mapped across the study area illustrates higher amplitude on steep slopes is difficult to distinguish from the landslide area outlined in red.

components. The first principal component is determined by maximizing the variance of the data set projected along orthogonal directions. Subsequent components are iteratively determined by removing the contribution of the previous component to the data.

The first three principal components from this analysis are illustrated in Figure 2.29.3, in order of importance. The first and strongest component (PC1) is shown to have an eigenvector time history with a consistent slope and the spatial distribution and contribution intensity of the data maps well within the Blakemont landslide area. This suggests continuous landslide motion unaffected by seasonal variations such a continuous creep. The second component (PC2) suggests seasonally driven landslide motion, mapping well within the landslide area though with clear seasonal fluctuations in the eigenvector time history. The third component (PC3) suggests seasonally driven distributed ground motion, with clear seasonal fluctuations while mapping more evenly across the study area.

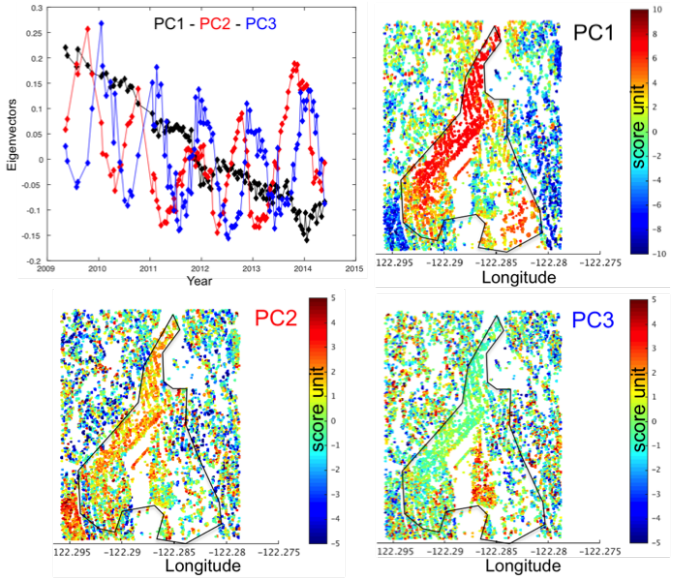

Figure 2.29.3. Principal Component Analysis results illustrating (upper left) the temporal fluctuations of the principal component eigenvectors and; the spatial distribution and contribution intensity of the data for (upper right) Principal Component 1, (lower left) Principal Component 2, (lower right) Principal Component 3.

Acknowledgements

We gratefully acknowledge our financial support from the Lawrence Berkeley National Laboratory, Earth Science Division Director's Fund.

References

Cohen-Waeber J. et al. (2013), GPS Instrumentation and Remote Sensing Study of Slow Moving Landslides in the E. San Francisco Bay Hills, CA. Proceedings of the 18th Int. Conf. on Soil Mech. and Geotech. Eng., Paris, France.

Ferretti A. et al. (2011), A New Algorithm for Processing Interferometric Data-Stacks: SqueeSAR. *IEEE Geoscience and Remote Sensing* 49(9), 3460-3470.

Giannico C. and Ferretti A. (2011), SqueeSAR™ Analysis Area: Berkeley. Processing Report. Tele-Rilevamento Europa, Milano, IT.

Bjornsson H. and Venegas S.A. (1997) A manual for EOF and SVD analyses of climate data. McGill University, CCGCR Report No. 97-1, Montreal, Quebec, 52 pp.

Hilley G.E. et al. (2004) Dynamics of Slow Moving Landslides From Permanent Scatterer Analysis. Science 304, 1952-1955.

Quigley K. C. et al. (2010), Seasonal Acceleration and Structure of Slow Moving Landslides in the Berkeley Hills. Proc. of the 3rd Conf. on Earthquake Hazards in the E. San Francisco Bay Area; edited by Keith Knudsen. CA Geol. Surv. Special Report 219, 169-178.

30 Geodetic Investigation of Compliant Fault Zones in the San Francisco Bay Area

Kathryn Materna, Roland Bürgmann, Ingrid Johanson

Introduction

The San Andreas Fault is the dominant fault strand in the complex plate boundary between the North American and Pacific plates. As a fault that has been active for millions of years, the San Andreas is thought to lie within a low-rigidity damage zone resulting from past earthquakes; this damage zone is often called a compliant fault zone (CFZ). An important question in the study of active faults such as the San Andreas is how these fault zones can be characterized using geodetic and seismic datasets. The properties of CFZ's have implications for fault strength, fault behavior, strong ground motions, and the long-term evolution of plate margins. In Northern California, the CFZ surrounding the San Andreas Fault has specific implications for seismic hazard in the Bay Area.

In this study, we investigate the elastic properties of the fault zone surrounding the San Andreas Fault at Black Mountain, California, a 2,800-foot peak in the Santa Cruz Mountains. This area contains a dense network of survey benchmarks within five kilometers of the fault, with a history of campaign GPS occupations dating back to 1996. Prior to the advent of GPS, this area was also measured for several decades using Electronic Distance Measurements (EDM). In this project, we conducted a field campaign to collect GPS measurements in early 2015. We utilized the EDM data and the recently updated GPS data, as well as additional seismic datasets, to place new constraints on the elastic properties of the compliant fault zone in this region.

We are primarily interested in characterizing four major properties of compliant fault zones that influence their patterns of deformation. These properties are: 1) the width of the CFZ; 2) the elastic modulus or rigidity of the CFZ (usually expressed as a fraction of the elastic modulus of the intact rock); 3) the slip rate on the fault; and 4) the locking depth of the fault. We aim to find a CFZ model that satisfies the geodetic and seismic observations from this area. We also aim to identify trade-offs between these parameters in the geodetic data, and use seismic data to gain insight where geodetic data is not sensitive.

CFZ vs. Homogeneous Half-Space Model

For an initial comparison, we fit the GPS velocities in Figure 2.30.1 with the deformation expected from a locked fault in a homogeneous elastic half-space (no compliant fault zone). The parameters that control the expected deformation in this case are only the locking depth and fault slip rate. In order to fit the velocity gradients in Figure 2.30.1 at a level better than the RMS error in the GPS data itself, we need to impose a shallow locking depth. Assuming slip rates of 15-20 mm/year, in agreement with geologic and geodetic estimates, we need a locking depth of 5-6 km to explain the deformation at Black Mountain.

However, in the NCEDC double-differenced earthquake catalog, we find seismicity at Black Mountain from 1984 to the present at up to 12 km depth. We reject the idea that a homogeneous half-space is realistically able to explain the deformation at Black Mountain because the required locking depth (5-6 km) is not consistent with seismicity in the region. This finding is consistent with other geodetic studies of the northern San Andreas Fault (*Chen and Freymueller,* 2002; *Jolivet et al.,* 2009).

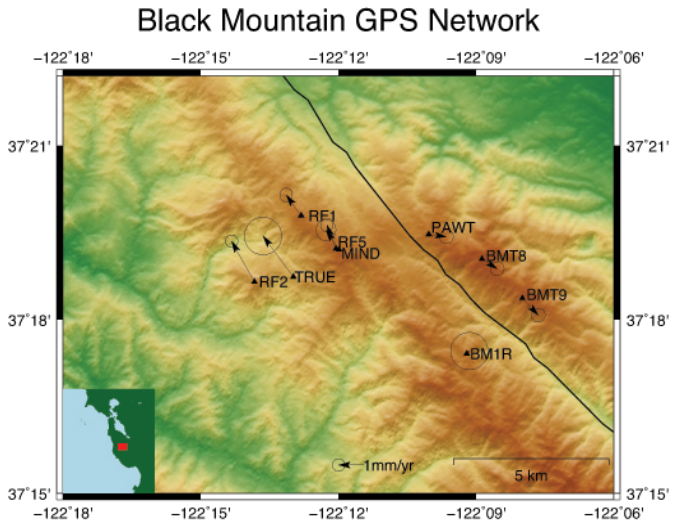

Figure 2.30.1. The GPS network at Black Mountain, in the Santa Cruz Mountains of Northern California. Each survey benchmark is plotted with its velocity vector, which has been generated from the data collected between 1996 and 2010. The error ellipses represent formal uncertainties. The San Andreas Fault is drawn in black in the center of the image.

We also explore a range of compliant fault zone models to better explain the GPS data and EDM data. The deformation expected across a compliant fault zone can be modeled explicitly in terms slip rate, locking depth, fault zone width, and fault zone elastic modulus (*Rybicki and Kasahara,* 1977). As shown in Figure 2.30.2, the effect of the CFZ on the deformation field is to concentrate strain in the region of reduced elastic modulus. Therefore, we are able to find CFZ models with deeper, more realistic locking depths that also reflect the high strain rate across the fault that we observe in the GPS measurements.

We search through the space of parameters for CFZ models that fit the GPS data at levels better than the error in the data itself. The resulting combinations of parameters for CFZ models are shown in Figure 2.30.3.

Preliminary Results

Our work shows that the best-fitting models of deformation at Black Mountain have a CFZ width of about 2 km and a rigidity of about 60%-90% of the rigidity of the intact rock. These GPS-derived estimates of CFZ properties improve upon previous estimates that were derived mostly from EDM. Pre-

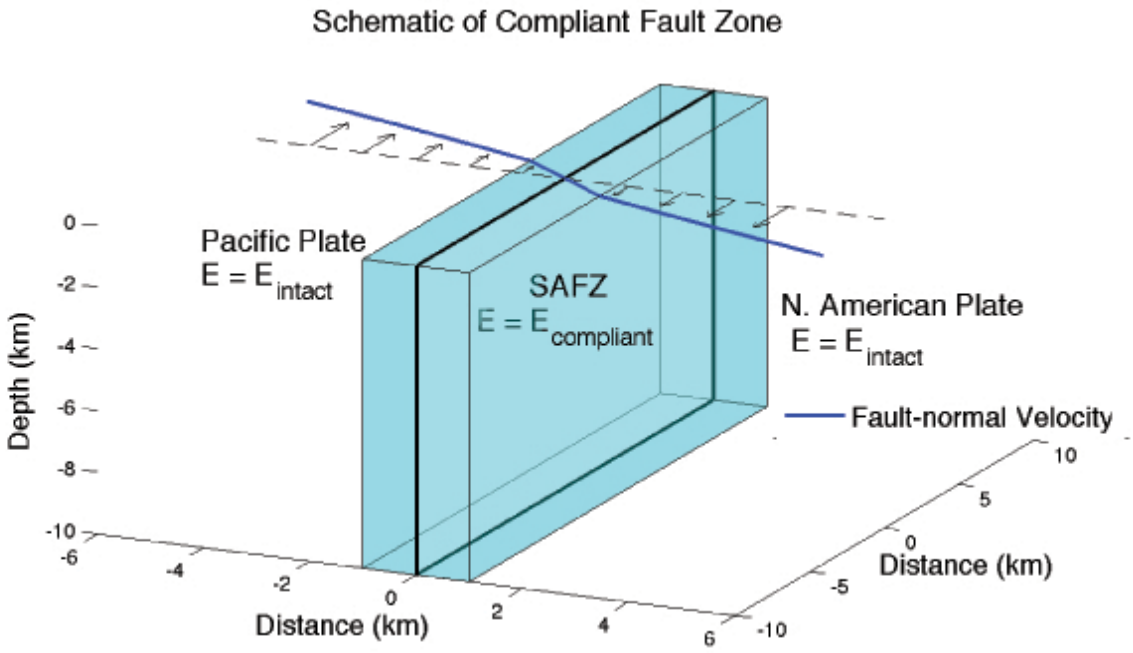

Figure 2.30.2: A schematic of a compliant fault zone. The CFZ shown here has a width of 2 km, a locking depth of 10 km, and an elastic modulus equal to one half the elastic modulus of the intact rock. The CFZ concentrates the strain from interseismic tectonic movement into the fault zone itself. The velocity gradient is highest in the fault zone..

vious results from Chen and Freymueller (2002) estimate that the rigidity in the fault zone at Black Mountain is 37%-81% of the rigidity of intact rock, and that the width of the fault zone is not well constrained. Our estimates of elastic modulus and fault zone width show that only CFZ's with widths of about 2 km are able to satisfactorily fit the data.

The results also show that a major trade-off exists between locking depth and plate velocity (plot E); as a result, different combinations of locking depth and plate velocity result in very similar models. That trade-off also explains the diffuse appearance of the models in the other plots (A, C, D, and F). These results show that with independent constraints from seismology, such as a 12 km locking depth, we can determine more accurate constraints on all parameters that describe the compliant fault zone structure. In the future, we hope to compare the elastic properties identified at Black Mountain to elastic properties on other sections of the San Andreas Fault. Such a comparison may yield new information about the development of fault zones as a function of space and time.

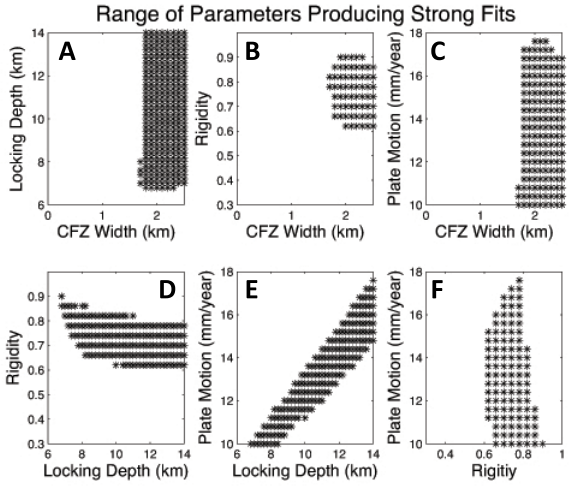

Figure 2.30.3. Black dots represent combinations of parameters that produced compliant fault zone models in strong agreement with the GPS data at Black Mountain, California.

Acknowledgements

The authors would like to thank the Mid-Peninsula Open Space District and the Santa Clara County Parks Department for help with permitting and fieldwork. We would also like to thank the graduate students who assisted in the field (Mong-Han Huang, Brent Delbridge, Alizee Dubois, Robert Martin-Short, and Chelsea Willett, from UC Berkeley; Leighton Watson, from Stanford University). This work is supported by the USGS NEHRP Grant G13AP00035.

References

Chen, Q., and J. Freymueller (2002), Geodetic evidence for a near-fault compliant zone along the San Andreas Fault in the San Francisco Bay Area: *Bulletin of the Seismological Society of America, 92, 656-671. DOI: 10.1785/0120010110.*

Jolivet, R., R. Bürgmann, and N. Houlie (2009), Geodetic exploration of the elastic properties across and within the northern San Andreas Fault zone, *Earth and Planetary Science Letters,* 288, 126-131. DOI: 10.1016/j.epsl.2009.09.014.

Rybicki, K., and K. Kasahara (1977), A strike-slip fault in a laterally inhomogeneous medium, *Tectonophysics,* 42, 127-138. DOI: 10.1016/0040-1951(77)90164-0.

31 Heterogeneity of Oceanic Upper Mantle Rheology on Viscoelastic Postseismic Deformation of 2012 M_w8.6 Indian Ocean Earthquake

Yan Hu, Roland Bürgmann

Introduction

Knowledge of the rheology structure of the oceanic upper mantle has been limited by the scarcity of observations of large earthquakes occurring in oceanic plates, until the largest recorded M_w8.6 strike-slip type earthquake that took place on April 11th, 2012 in the Indian Ocean. More than forty continuous Global Positioning System (GPS) in Sumatra, India, and the Indian Ocean recorded up to ~30 cm coseismic displacements and up to ~11 cm postseismic displacements in the first two years after the earthquake (Figure 2.31.1). The striking feature of the deformation associated with this event is that several stations close to the rupture area in Sumatra underwent subsidence during the earthquake but persistent postseismic uplift since the earthquake (right side of Figure 2.31.1). The high quality coseismic and postseismic crustal deformation delineated by the continuous GPS stations provides a unique opportunity for us to better understand the three dimensional (3D) rheology heterogeneity of the oceanic upper mantle.

In this work, we integrate the high-quality of the geodetic data in Sumatra and modeling experiences developed at other margins to investigate the effects of the oceanic upper mantle rheology on the viscoelastic postseismic deformation following the 2012 earthquake.

Finite Element Model

We use a 3D finite element model (FEM) that is able to incorporate the complex slab geometry and tectonic structure in the real Earth (*Hu et al.*, 2004). The model consists of a 50 km elastic upper plate, a 50 km elastic subducting plate, a viscoelastic continental mantle wedge, a viscoelastic oceanic upper mantle, and a viscoelastic asthenosphere beneath the oceanic lithosphere. We follow Hu et al. (2014) on the setup of rock properties and summarize the model parameters as follows. Shear moduli of the elastic lithosphere and viscoelastic upper mantle and asthenosphere are 48 GPa and 64 GPa, respectively. Poisson's ratio is assumed to be 0.25 in the entire model domain. Model boundaries are made hundreds of kilometers from the rupture area to eliminate the artifacts of boundary effects.

The bi-viscous Burgers rheology is assumed to represent the viscoelastic relaxation of the upper mantle and asthenosphere (*Bürgmann and Dresen*, 2008). Based on previous studies (*e.g., Pollitz et al.*, 2008; *Wang et al.*, 2012; *Hu et al.*, 2014), we assume that the transient Kelvin viscosity ηK is one order of magnitude lower than that of the steady-state Maxwell viscosity ηM. Following studies of other margins (*e.g.*, *Wang et al.*, 2012; *Hu et al.*, 2014) we assume that ηM of the mantle wedge is 1019 Pa s. Varying ηM of the mantle wedge by one order of magnitude does not significantly change the model-predicted surface deformation since the rupture area hundreds of kilometers away is on the ocean side. Viscosity of the oceanic upper mantle and viscosity and thickness of the asthenosphere are to be determined in this work.

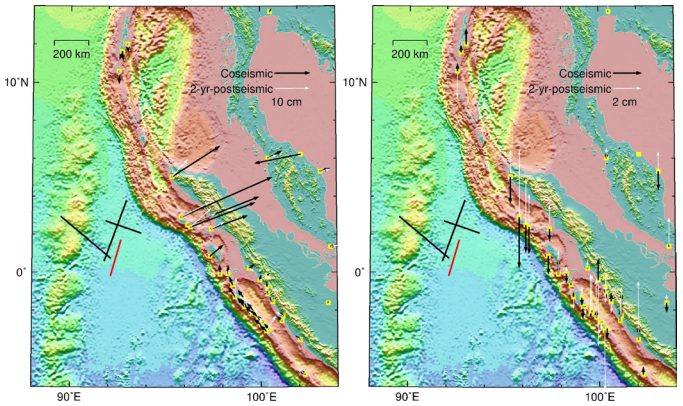

Figure 2.31.1: Coseismic (black arrows) displacements of the 2012 Indian Ocean earthquake and two-year cumulative postseismic displacements (white arrows). Thick black and thick red lines represent the rupture segments two hours after the Mw8.6 mainshock and Mw8.2 aftershock, respectively (*Wei et al.*, 2012). GPS displacements are processed from daily solutions of GPS time series obtained from Nevada Geodetic Laboratory (http://geodesy.unr.edu/index.php).

We vary the viscosity of the oceanic upper mantle and thickness and viscosity of the asthenosphere at ranges of 1019–1022 Pa s, 5–300 km, and 1017–1020 Pa s, respectively, and construct hundreds of test models. We then calculate the total misfit to GPS observations for each test model for time windows of six months, one year, 1.5 years and two years. The minimal misfit is the preferred finite element model of the 2012 earthquake.

Model Results

Our test models indicate that sensitivities of the properties of the oceanic upper mantle and asthenosphere are different for different components of surface deformation (Figure 2.31.2). Acceptable fit to both horizontal and vertical components (Figure 2.31.2c) requires that the viscosity of the oceanic upper mantle is ~5 × 1020–1022 Pa s, with thickness and viscosity of the asthenosphere to be ~10–60 km and ~3 × 1017–2 ×1018 Pa s, respectively. In a preferred model (PFM), determined values of the viscosity of the oceanic upper mantle, thickness and viscosity of the asthenosphere are 1021 Pa s, 30 km, and 5 × 1017 Pa s, respectively. ηM of the asthenosphere may be traded-off by the quadratic power of its thickness (black solid line in Figure 2.31.3). The PFM well reproduces the first-order pattern of the landward motion and uplift at GPS stations close to and North of the rupture area (Figure 2.31.4). The large misfit for the southern stations is probably due to the high noise-signal level in the GPS time series. The thin and weak asthenosphere determined in this work is consistent with other seismic studies. For example, Stern et al. (2015) reported a thin

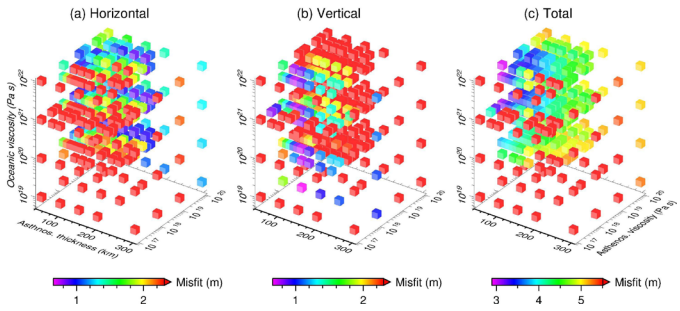

Figure 2.31.2: Systematic tests on the properties of the asthenosphere and oceanic upper mantle. (a) Misfit of horizontal components only. (b) Misfit of the vertical component only. (c) Misfit of horizontal and vertical components.

10 km lithosphere-asthenosphere-boundary layer at a viscosity ~1018 Pa s through studying high-quality seismic images in New Zealand.

Acknowledgements

We are thankful for the computing facility, Pacman, managed by Arctic Region Supercomputing Center (ARSC) at University of Alaska Fairbanks and thankful for the publicly available GPS time series by NGL. This work was funded by NSF award EAR-1246850 and benefitted from support by the Miller Institute for Basic Research in Science.

References

Bürgmann, R., and Dresen, G. (2008), Rheology of the lower crust and upper mantle: Evidence from rock mechanics, geodesy, and field observations, *Annu. Rev. Earth Planet. Sci., 36, 531–567, doi:10.1146/annurev.earth.36.031207.124326.*

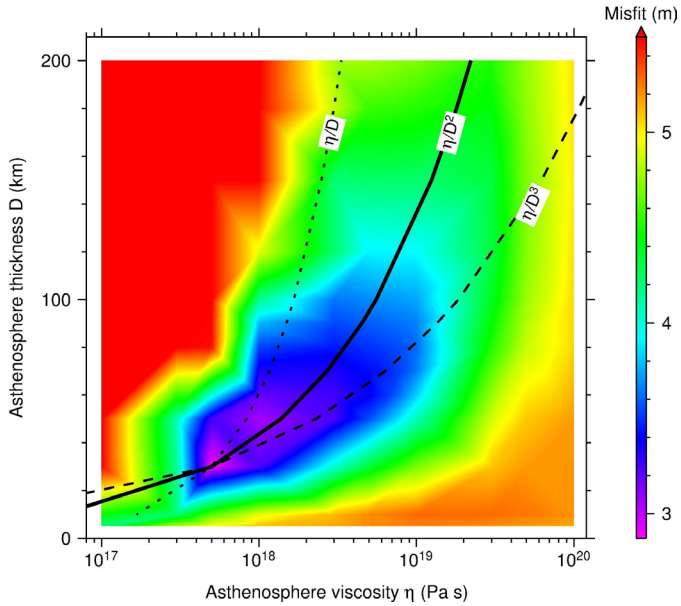

Figure 2.31.3: Trade-off between the thickness (D) and viscosity (η) of the asthenosphere. ηM of the oceanic upper mantle is fixed at 1021 Pa s. Dotted, dashed, and solid lines represent possible power relationships between D and η.

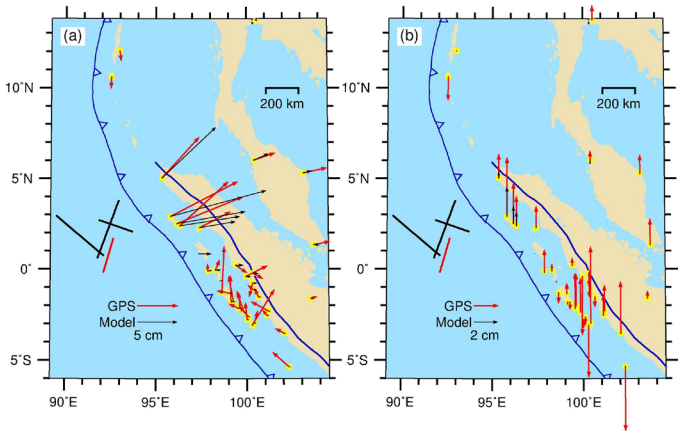

Figure 2.31.4: Comparison of two-year postseismic GPS observations (red arrows) with displacements predicted by PFM (black arrows). Yellow squares represent the location of GPS stations.

Hu, Y., *et al.* (2014), Contributions of poroelastic rebound and a weak volcanic arc to the postseismic deformation of the 2011 Tohoku earthquake, *Earth Planet Science,* 66, 106, doi :10.1186/1880-5981-66-106.

Hu, Y., *et al.* (2004), Three-dimensional viscoelastic finite element model for post-seismic deformation of the great 1960 Chile earthquake, *J. Geophys. Res.*, 109, B12403, doi:10.1029/2004JB003163.

Nevada Geodetic Laboratory, http://geodesy.unr.edu/index.php), accessed on 01/30/2015.

Pollitz, F.F., *et al.* (2008), Effect of 3-D viscoelastic structure on post-seismic relaxation from the 2004 M= 9.2 Sumatra earthquake, *Geophys. J. Int.*, *173*(1), 189-204, doi:10.1111/j.1365-246X.2007.03666.x.

Stern, T.A, *et al.* (2015), A seismic reflection image for the base of a tectonic plate, *Nature, 518, 85-88,doi:10.1038/nature14146.*

Wang, K., Hu, Y., He, J. (2012), Deformation cycles of subduction earthquakes in a viscoelastic Earth, *Nature*, 484, 327-332, doi:10.1038/nature11032.

Wei, S., Helmberger, D., Avouac, J.-P. (2013), Modeling the 2012 Wharton basin earthquakes off-Sumatra: Complete lithospheric failure, *J. Geophys. Res. Solid Earth*, 118, 3592–3609, doi:10.1002/jgrb.50267.

32 Seasonal Loading: The Resulting Deformation and Occurrence of Earthquakes in California

Christopher W. Johnson and Roland Bürgmann

Summary

Observations of periodic earthquake occurrence may be linked to stress changes on a fault due to varying hydrospheric surface loads (groundwater, surface water and snow), which exhibit seasonal periodicity (*Argus et al.*, 2014). In California, the accumulated winter snow pack in the Sierra Nevada, reservoirs, and groundwater water storage in the Central Valley follow an annual periodic cycle and each contribute to the resulting surface deformation, which can be observed using continuous GPS time series (*Amos et al.*, 2014; *Argus et al.*, 2014; *Borsa et al.*, 2014). Annual vertical and horizontal displacement amplitudes of GPS stations in the Sierra Nevada and California Coast Ranges produced by seasonal changes in water storage are on the order of 1 - 5 mm and 0.5 - 2 mm, respectively (*Amos et al.*, 2014). In the Central Valley and other sedimentary basins, the seasonally observed vertical surface displacements are controlled by groundwater level in the aquifer as a poroelastic response to changes in the head level. Simple 1D line load models used to estimate the seasonal stress cycles associated with hydrospheric loading on the San Andreas fault are on the order of 1 kPa (*Amos et al.*, 2014). These stress changes are small, but comparable in size to known stress perturbations that have been associated with changes in earthquake activity.

Knowledge of what governs the timing of earthquakes is essential to understanding the nature of earthquake cycles and determining time-dependent earthquake hazard, but the variability and controls of earthquake occurrences are not yet well established. If small static stress changes influence the timing of earthquakes, then one could expect that events will occur more rapidly during periods of greater external load increases. Studies investigating the occurrence of seismic events with respect to seasonal forcing suggest that stress perturbations <1 kPa are influencing regional faulting systems and seasonally modulating earthquake nucleation times (*Bettinelli et al.*, 2008; *Christiansen et al.*, 2007; *Gao et al.*, 2000; *Pollitz et al.*, 2013). Periodic signals that are observed in earthquake catalog time series suggest that periods of 4-, 6-, 120-, and 14.24-months are statistically significant in the regions of California (Figure 2.32.1). They also provide documentation for the modulation of earthquake populations at periods of natural loading cycles (*Dutilleul, in prep*). In California, the seasonal cycles of snow and water loads in the Sierra Nevada and Central Valley may drive periodic seismicity patterns, thus providing a physical connection to modulated earthquakes due to long-period stress changes. Studies of earthquake triggering by the short-period daily tides find a weak correlation of seismicity rates with tidal stresses, which are comparable in amplitude to the seasonal loads (*Vidale et al.*, 1998).

This study preforms a critical analysis of the sensitivity of earthquake occurrences to small external stress changes by testing the hypothesis of modulation by small periodic stresses focusing on annual stressing by hydrospheric surface loads. We develop models of annual surface load cycles constrained by GPS, GRACE gravity data, and hydrological models (*Amos et al.,* 2014*; Argus et al.,* 2014) to calculate the associated stress changes for different fault environments in California as shown in the focal mechanisms in Figure 2.32.2. We then evaluate the degree of correlation between the stress models and seismicity, taking into consideration the variable amplitude of stress cycles, the orientation of transient load stress with respect to the background stress field, and the geometry of active faults as is revealed by focal mechanisms.

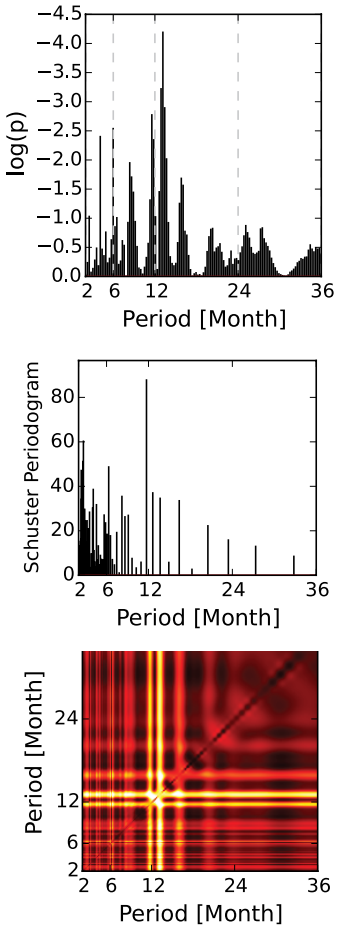

Figure 2.32.1: Three statistical tests for periodicity in earthquake catalog time series constructed from a subset of California earthquakes located within 100 km of Parkfield, CA (*Dutelleul, in prep*). The top panel shows the results of Schuster tests over a range of periods (*Ader and Avouac*, 2013; *Schuster*, 1897); i.e. a Schuster spectrum, the middle panel shows a Schuster periodogram (*Schuster*, 1898), and the lower panel is the result of a mutli-frequential periodogram analysis (*Dutilleul*, 2001). Each analysis indicates a statistically significant strong 12-month annual period with semi-annual periods of 4- and 6-months.

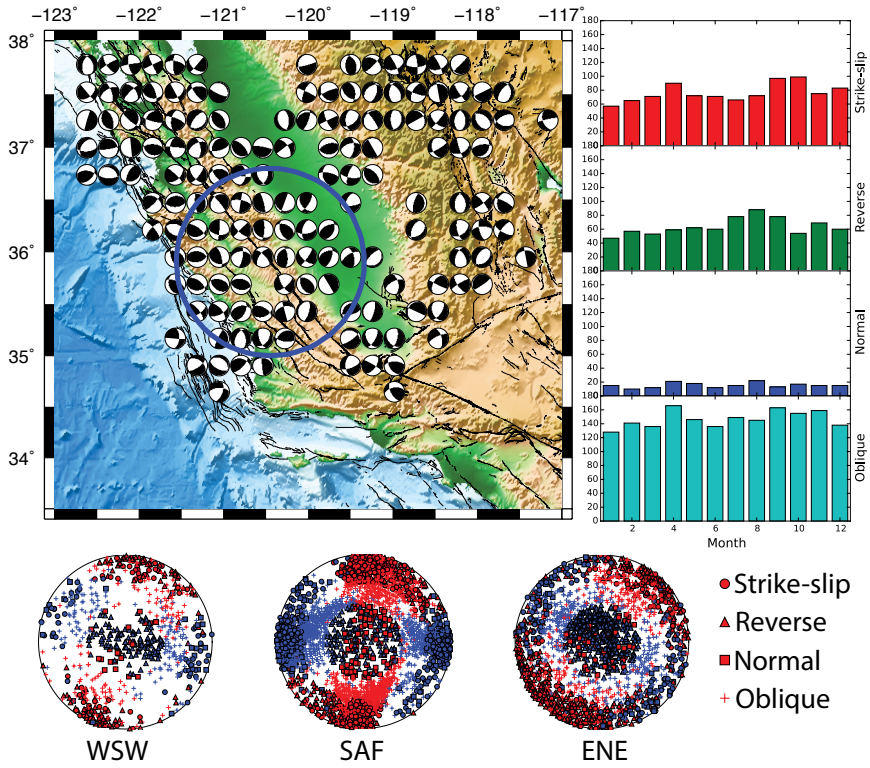

Figure 2.32.2: (Top left) Map of California with example focal mechanisms (www.ncedc.org) at a grid spacing of 20 km to visualize the differing tectonic stress regimes. The blue circle indicates the preliminary study area. Seismicity is analyzed for spatial and temporal changes with respect to seasonal loading. (Top Right) The monthly distribution of seismicity between 1988-2002 separated by fault type. The histograms indicate annual peaks in April and October for strike-slip and oblique events. The reverse events exhibit a phase shift in peak seismicity. The significance of the observed phase shift and peak periods of seismicity will be investigated using a regional surface-loading model to calculate seasonal stress perturbations. (Bottom) Stereonet diagrams of P (red) and T (blue) axes for each focal mechanism shown for three sub-areas within the circular area around Parkfield (WSW of SAF, within ± 5 km from SAF, and ENE of SAF). The symbols designate different fault types. The data will be thoroughly analyzed for changes in the distribution of P-axis orientations with respect to the modeled seasonal stress tensor variations.

Acknowledgements

C.W. Johnson is supported by NSF Graduate Research Fellowship Program fund number DGE 1106400.

References

Ader, T. J., and J.-P. Avouac (2013), Detecting periodicities and declustering in earthquake catalogs using the Schuster spectrum, application to Himalayan seismicity, *Earth and Planetary Science Letters*, 377-378, 97-105.

Amos, C. B., P. Audet, W. C. Hammond, R. Burgmann, I. A. Johanson, and G. Blewitt (2014), Uplift and seismicity driven by groundwater depletion in central California, *Nature*, 509(7501), 483-486.

Argus, D. F., Y. Fu, and F. W. Landerer (2014), Seasonal variation in total water storage in California inferred from GPS observations of vertical land motion, *Geophysical Research Letters*, 41(6), 1971-1980.

Bettinelli, P., J.-P. Avouac, M. Flouzat, L. Bollinger, G. Ramillien, S. Rajaure, and S. Sapkota (2008), Seasonal variations of seismicity and geodetic strain in the Himalaya induced by surface hydrology, *Earth and Planetary Science Letters*, 266(3-4), 332-344.

Borsa, A. A., D. C. Agnew, and D. R. Cayan (2014), Ongoing drought-induced uplift in the western United States, *Science*, 345(6204), 1587-1590.

Christiansen, L. B., S. Hurwitz, and S. E. Ingebritsen (2007), Annual modulation of seismicity along the San Andreas Fault near Parkfield, CA, *Geophysical Research Letters*, 34, L04306, doi:10.1029/2006GL028634.

Dutilleul, P. (2001), Multi-frequential periodogram analysis and the detection of periodic components in time series, *Communications in Statistics - Theory and Methods,* 30(6), 1063-1098.

Gao, S. S., P. G. Silver, A. T. Linde, and S. Sacks (2000), Annual modulation of triggered seismicity following the 1992 Landers earthquake in California, *Nature*, 406, 500-504.

Pollitz, F. F., A. Wech, H. Kao, and R. Bürgmann (2013), Annual modulation of non-volcanic tremor in northern Cascadia, *Journal of Geophysical Research: Solid Earth*, 118(5), 2445-2459.

Schuster, A. (1897), On lunar and solar periodicities of earthquakes, *Proceedings of the Royal Society of London*, 61, 455-465.

Schuster, A. (1898), On the investigation of hidden periodicities with application to a supposed 26-day period in meteorological phenomena, *Terrestrial Magnetism*, 3, 13-41.

Vidale, J. E., D. C. Agnew, M. J. S. Johnston, and D. H. Oppenheimer (1998), Absence of earthquake correlation with Earth tides: An indication of high preseismic fault stress rate, *Journal of Geophysical Research*, 103(B10), 24567.

Research Studies:
Seismic Sources

34 The Effects of 3D Heterogeneity on Source Inversion

Andrea Chiang, Douglas S. Dreger

Introduction

We have established in previous works (e.g. *Dreger et al.*, 2008; *Ford et al.*, 2009; *Ford et al.*, 2008; *Ford et al.*, 2010; *Ford et al.*, 2012; *Chiang et al.*, 2014) that the regional seismic moment tensor method is a robust and reliable technique to identify different seismic source types, even though the complexities in isotropic source processes are not often well understood. For nuclear explosion source-type identification problems, the uncertainties in a solution is just as important as the best fitting parameters. Developing a full understanding and proper characterization of the uncertainties is key to being able to assess populations of moment tensor results for explosions, collapses, earthquakes, geothermal and volcanic events. In regions with low seismicity or lack of high-resolution velocity models, the common and most-trusted approach to compute Green's functions for moment tensor inversion is through broadband waveform modeling to produce a 1D velocity model. Uncertainty in the velocity model is the greatest source of error in moment tensor inversions and its effects on the recovered source mechanism has never been fully investigated for explosions. In this study we would like to determine the effect of a 1D velocity model assumption as a function of data quality, passband, and sensor configuration through a synthetic study, as well as applications to western US events.

Data and Method

In the synthetic study, we produced waveforms with the effects of 3D velocity heterogeneity. The effects of the 1D velocity model assumption can then be interpreted via the difference between input and inverted solutions. We used the anelastic finite-difference code, SW4, developed at the Center of Applied Scientific Computing at Lawrence Livermore National Laboratory (LLNL) to simulate ground motion, and the Little Skull Mountain Mainshock station configuration (*Ford et al.*, 2009) for all of the simulations in this experiment to reflect current regional monitoring capabilities (Fig. 2.34.1). The 3D ambient noise surface wave tomography by *Moschetti et al.* (2010) is used to simulate synthetic data and a well-calibrated 1D western U.S. model by *Song et al.* (1996) was used to compute the 1D Green's functions. For each simulated data, we added random Gaussian white noise to the data by scaling the amplitude of the noise to 10% of the maximum amplitude of the data. We performed the moment tensor inversion between 10 s to 50 s, the typical passband used for regional moment tensor and analyzed two major source types:

1. Double-couple (DC) - earthquake - mechanism and,
2. Isotropic (ISO) - explosion

The double-couple scenario consists of a normal and oblique reverse mechanism at 4.53 km depth, and the isotropic scenario consists of an explosion at 500 m depth.

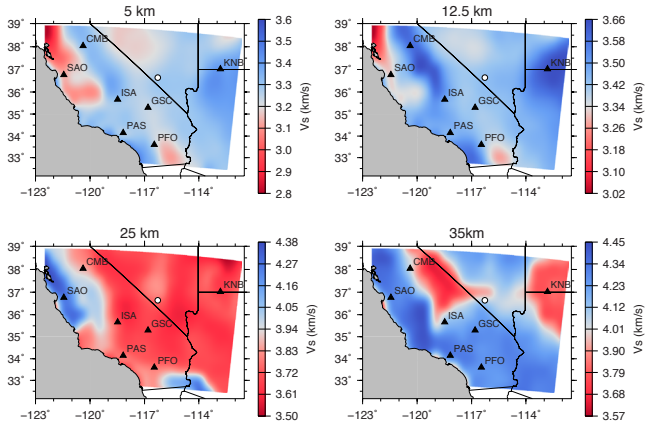

Figure 2.34.1: Event and station locations for the synthetic study. White circles are the events and black triangles are the stations. Background color represent shear wave velocity (V_s) at various crustal depths from the surface wave tomography model by *Moschetti et al.* (2010).

Synthetic Sandbox

For the DC synthetics, both deviatoric and full moment tensor inversions can recover the correct source mechanism, and the waveform fits are very similar for both inversion schemes (Fig. 2.34.2). Although the moment tensor results show up to 20% false ISO component in the full moment tensor inversion, the change in waveform fits is not statistically significant, with the additional degree of freedom in the inversion. Similarly, the Network Sensitivity Solutions (NSSs) show an earthquake-like distribution with the bullseye centered on a pure DC mechanism (Fig. 2.34.3). In terms of the source depth recoverability, we can estimate the correct depth and mechanism from the behavior of the waveform fits with respect to the source depth. For both DC cases, the moment tensor solutions are stable with respect to source depth, where the solutions with the best waveform fits (variance reduction (VR) > 60%) are between 5 and 7 km. The solutions with the maximum waveform fits are the correct mechanism and at depths very closely located to the correct source depth of 4.53 km. For the two double-couple cases, we can recover the correct DC mechanism using only regional waveforms and the 1D model assumption is also valid. The effects of 3D heterogeneity are negligible at these periods with a well-calibrated 1D model.

For the ISO case, the deviatoric moment tensor solutions are stable at shallow depths (1 km or less), but the isotropic component is not well constrained in the full moment tensor inversion, because the isotropic component is very sensitive to time shifts in the inversion. The recovered full moment tensor mechanism varies between a predominantly explosive mechanism and a predominantly compensated linear vector dipole (CLVD) mechanism, with the major vector dipole in compression. However, the NSS exhibits a typical explosion-like distribution and so we can eliminate the incorrect CLVD solutions by including additional first motion polarities (Fig. 2.34.3).

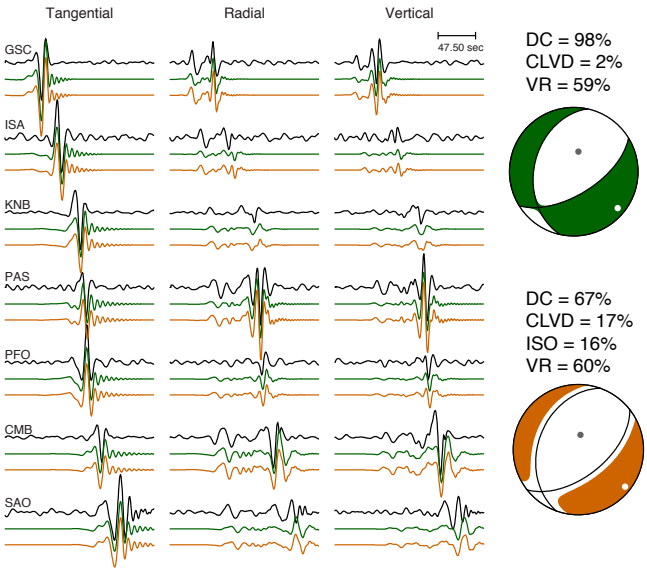

Figure 2.34.2: Full and deviatoric moment tensor solutions from waveform inversion. Displacement waveforms (black solid lines) and full moment tensor synthetics (red dashed lines) are filtered between 1.25 to 2 s period. P-wave up first motions (red dots) are plotted on top of the focal mechanisms.

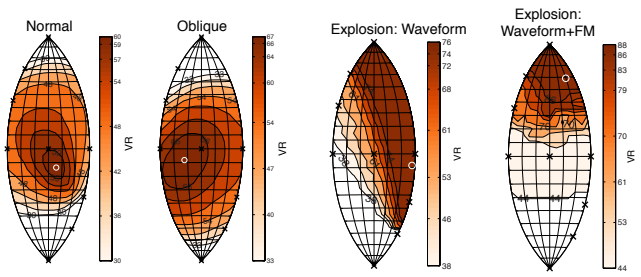

Figure 2.34.3: Network Sensitivity Solutions for the different source mechanisms. Contoured regions are color-coded by their variance reduction (VR), black crosses mark the positions of theoretical source mechanisms, and white circles are the best-fitting full moment tensor solution.

Discussions and Conclusions

In previous works, we have investigated errors in the moment tensor analysis in terms of noise, station configuration, uncertainties in velocity models, and free surface effects. However, all of the analyses were made under a 1D velocity model assumption. In this study we have shown that the 1D velocity model is a valid assumption at the intermediate- to long-period ranges, although at very shallow depths the combined effects of the theoretical trade-off and shallow structural complexities can impact the recovered source mechanism. But we also show that by combining first motion polarities and regional seismic waveforms, the predominately CLVD mechanisms can be eliminated. In addition, we computed 3D Green's functions via reciprocity to one of the explosions analyzed by *Ford et al.* (2009) and recovered a predominantly explosive mechanism (Fig. 2.34.4), that is similar to what *Ford et al.* (2009) obtained using 1D Green's functions.

We have expanded our source-type sensitivity matrix to evaluate major sources of errors due to the 1D velocity model assumption in the presence of noise, poor locations and non-ideal station configuration. By incorporating the different variables that can bias moment tensor inversions and presenting the results in the source-type space, it can help us improve our capabilities to perform near real-time moment tensor-based source discrimination analysis, and provide insight into estimating solution errors in regions where significant wave propagation effects exist, as well as areas where detailed Earth models are not readily available.

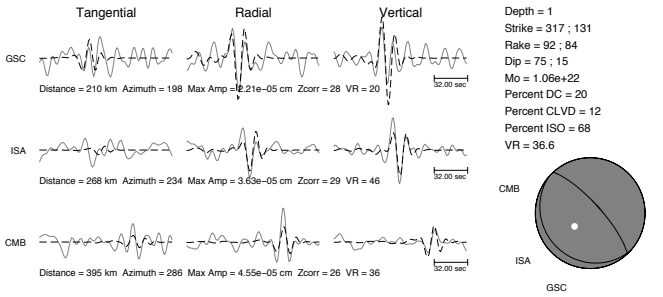

Figure 2.34.4: Full moment tensor solution and waveform fits for COSO.

Acknowledgements

We acknowledge funding from the Air Force Research Laboratory, contract FA9453-13-C-0271 that is supporting this research.

References

Chiang, A., Dreger, D. S., Ford, S. R., Walter, W. R., (2014), Source characterization of underground explosions from combined regional moment tensor and first motion analysis, *Bull. of the Seismol. Soc. Am.*, 104, doi:10.1785/0120130228.

Ford, S. R., Dreger, D. S., Walter, W. R., (2010), Network Sensitivity Solutions for regional moment-tensor inversions, *Bull. of the Seismol. Soc. Am.*, 100, 1962-1970, doi:10.1785/0120090140.

Ford, S. R., Walter, W. R., Dreger, D. S., (2012), Event discrimination using regional moment tensors, *Bull. of the Seismol. Soc. Am.*, 102, 867-872, doi:10.1785/0120110227.

Moschetti, M. P., Ritzwoller, M. H., Lin, F.-C., Yang, Y., (2010), Crustal shear wave velocity structure of the western United States inferred from ambient seismic noise and earthquake data, *J. Geophys. Res.*, 115, doi:10.1029/2010JB007448.

35 Ambient Seismic Noise Cross-Correlations in Northern California

Avinash Nayak, Taka'aki Taira, Douglas S. Dreger

Introduction

The cross-correlations of ambient seismic noise recorded at pairs of seismic sensors have been shown to converge over a period of time to the empirical Green's functions (GF) or the seismic medium's response at one receiver for a unit force applied at the other receiver. Using continuously recorded noise, GF thus obtained have been used for surface wave tomography and estimation of ground motions for earthquakes, as they incorporate attributes of seismic wave propagation in the real 3D earth. Other important applications include temporal monitoring of changes in the coda of noise-Green's functions (NGFs) obtained from noise cross-correlations to detect small changes in shear-wave velocity (*Brenguier et al.,* 2008) or changes in the positions of wavefield scatterers in the medium surrounding the seismic sensors. The use of ambient seismic noise as a seismic source overcomes the limitations in temporal and spatial coverage of earthquakes. Our current efforts employing seismic stations in Northern California include investigating the stability of NGF obtained using different processing approaches, comparison of NGF and synthetic GF computed using 1D velocity models, and monitoring and investigating temporal velocity changes at The Geysers geothermal field.

BDSN Stations

We cross-correlate noise recorded over a 60-day period by 3-component (E, N, Z) broadband sensors at five Berkeley Digital Seismic Network stations (BKS, CMB, HOPS, ORV, and SAO) to compute 9-component NGF (EE, EN… ZZ) in the frequency range of ~0.04-0.4 Hz at epicentral distances ~140-310 km. We use common factors for temporal and spectral normalization of all three components at a station. This preserves relative amplitudes between various components for a station pair and facilitates the rotation of horizontal components from Cartesian (E, N) to great circle path (R, T) coordinate systems after cross-correlation. Figure 2.35.1 shows a comparison of symmetric components of noise cross-correlations for two pairs of stations (BKS-HOPS and CMB-ORV) with synthetic GF computed using the frequency-wavenumber integration method (*Herrmann,* 2013*)* and two 1D velocity models (GIL7 and SOCAL, respectively). The path between BKS and HOPS traverses the Central Coast Ranges and the corresponding NGF are reproduced well by shallow layers of low-to-moderate shear wave velocities in the GIL7 model. For the ORV-CMB path, waves propagate through the granitic terrain of the Sierra Nevada, and NGF for this pair compare better to synthetics computed using the SOCAL model that consists of fewer layers in the shallow crust, higher velocities and a deeper Moho.

Convergence of daily noise-correlations towards stable values in the shortest possible time is important for temporary deployments and for good temporal resolution in monitoring temporal changes in NGF coda. We have tested various methods of temporal normalization – (1) running mean normalization, (2) clipping at ± 3 RMS, and (3) running mean normalization only applied above ± 3 RMS, to compare finite-duration stability and the final stack of ZZ NGF for BDSN stations. We find that methods that distort waveforms minimally (methods #2 and #3), lead to fastest convergence towards stable GF when used with overlapping windows (75%). Spectral normalization allows us to disregard amplitude response of the instrument while correcting for its phase response only during data pre-preprocessing. Finally, we find that while the surface waves in the final GF computed using different methods and window lengths are very similar to each other, there are minor differences (~ few %) in the coda of GF, which is a reflection of processing-generated noise relevant to studies on monitoring temporal changes in NGF coda.

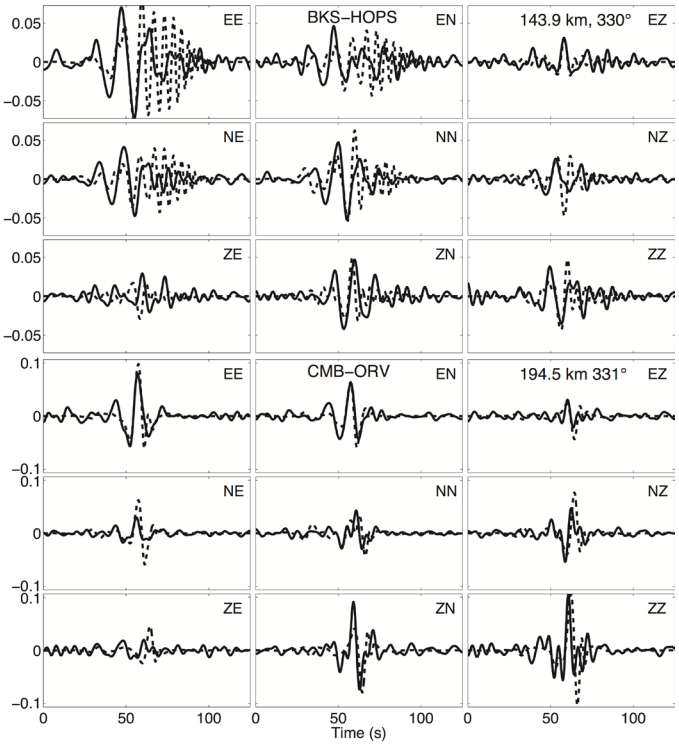

Figure 2.35.1: 9-component single force NGF (solid lines) and synthetic GF (dashed lines) for (a) BKS-HOPS and (b) ORV-CMB. Station names, interstation distance and azimuth are indicated at the top. First and second letters in upper right corner of each panel indicate the direction of a unit force applied at the first station and the component of displacement at the second station, respectively. The unit of the y-axis is displacement normalized by a common factor for all 9 components.

The Geysers

The Geysers (TG) in the Mayacamas Mountains is the world's largest geothermal field. It has witnessed significant increase in small magnitude (M_W 1.0-4.0) seismicity since the 1960s in response to steam production and water injection for reservoir recharge. Anomalous isotropic moments have also been detected

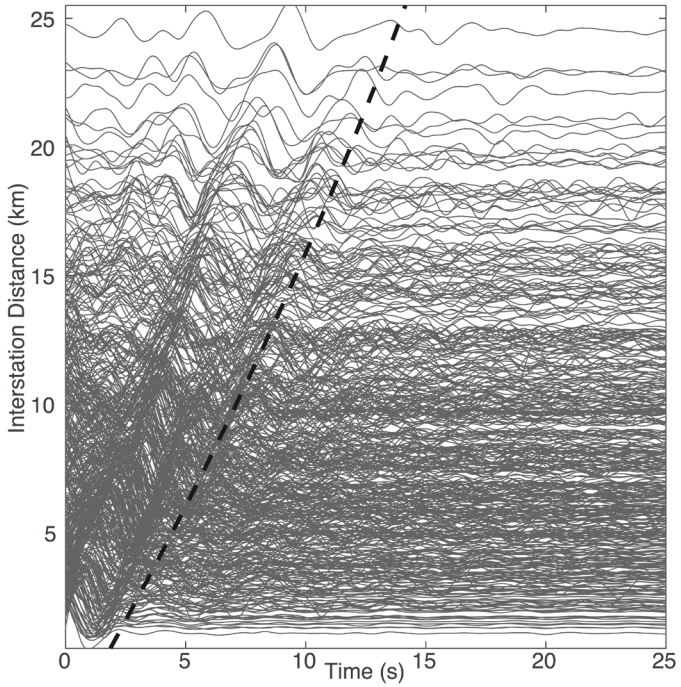

Figure 2.35.2: ZZ component NGF (~ 0.2-0.9 Hz) for 441 station pairs at The Geysers. Dashed line indicates the distance-dependent approximate coda wave onset time (envelope amplitude = 0.2 x peak).

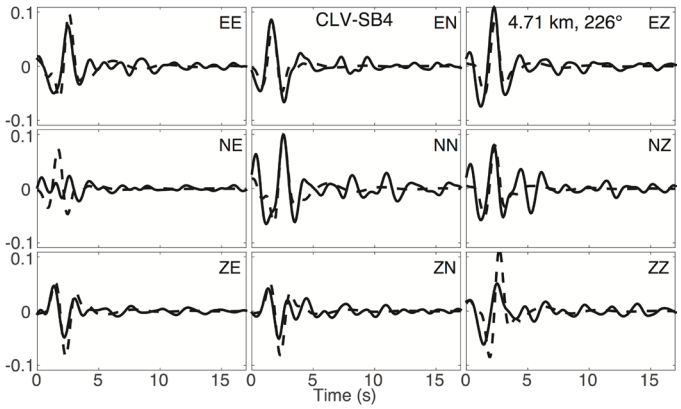

Figure 2.35.3: Same as Figure 2.35.1 but for pair CLV-SB4 (~0.2-0.9 Hz) at The Geysers.

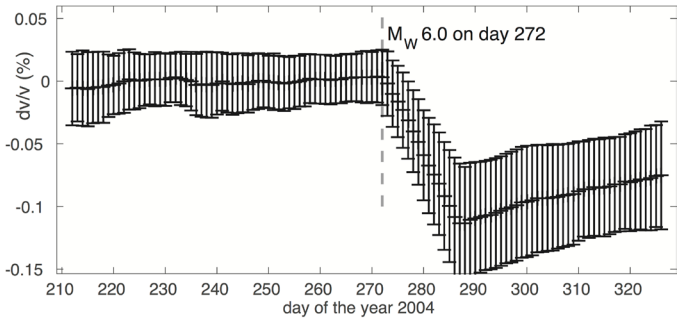

Figure 2.35.4: Velocity change (assumed to be homogeneous and zero before the event) in the source region of the 2004 Parkfield earthquake computed with 15-day stacks.

in full moment tensor solutions of many $M_W > 3.5$ earthquakes. A previous study (*Lai et al.,* in prep.) computed ZZ component NGF using two years (2012-2013) of data recorded continuously by the 35-station 4.5 Hz geophone network operated by Lawrence Berkeley National Laboratory at TG. In the southeastern section of TG, temporal changes in shear wave velocity estimated from NGF coda (~0.5-0.9 Hz) were observed to be related to the local injection volume. Specht et al. (2014) analyzed noise recorded by a network of temporary broadband stations and reported correlation between velocity changes and net steam production rates. We extend the analysis of Lai et al. (in prep.) to full 9-component noise cross-correlations and include additional stations present in and around TG. We use notch filters to suppress very narrowband spectral peaks observed in the data that are likely related to industrial noise. Figure 2.35.2 shows ZZ component NGF computed using noise recorded over a 100-day period in 2014. Figure 2.35.3 shows a comparison of NGF and synthetic GF (~ 0.2-0.9 Hz) computed using an average 1D velocity model of TG. In preparation for future work that involves investigating temporal velocity changes at TG, our methodology was validated by applying moving window (3.6 s at 50% overlap) cross-spectrum analysis to NGF at the borehole stations of the Parkfield High Resolution Network. In comparison to the 91 ZZ NGF and 30-day stacks employed by Brenguier et al. (2008) to estimate a ~0.06% velocity decrease accompanying the 28 Sept. 2004 Parkfield earthquake (M_W 6.0), we use 498 multi-component interstation NGF and obtain a stable time series indicating an average velocity decrease ~0.11% with only 15-day stacks (Figure 4).

Acknowledgements

This research is supported by U.S. National Science Foundation grant EAR-1053211. We would like to thank V.H. Lai and R. Gritto for helpful discussions.

References

Brenguier, F., Campillo, M., Hadziioannou, C., Shapiro, N.M., Nadeau, R.M., and E. Larose (2008), Postseismic relaxation along the San Andreas fault from continuous seismological observations: *Science, 321, 1478-1481, DOI: 10.1126/science.1160943.*

Herrmann, R. B. (2013) Computer programs in seismology: An evolving tool for instruction and research, Seism. Res. Lettr. 84, 1081-1088, doi:10.1785/0220110096

Lai, V.H., Taira, T., Dreger, D.S., and Huang, M.-H. (in prep.), Temporal variation in seismic velocity with fluid injection at the Geysers geothermal field, California.

Specht, S., Jousset, P., Zang, A., Gritto, R., and Bruhn, D. (2014), Velocity structure of The Geysers geothermal area (California) from ambient noise cross-correlation, Abstract S51A-4425, presented at AGU Fall Meeting, San Francisco, USA, 15-19 December 2014.

36 Analysis of Seismic Moment Tensor and Finite-Source Scaling During EGS Resource Development at The Geysers, CA

Douglas S. Dreger and O. Sierra Boyd

Introduction

Enhanced Geothermal Systems (EGS) resource development requires knowledge of subsurface physical parameters to quantify the evolution of fracture networks. We investigate seismicity in the vicinity of the EGS development at The Geysers Prati-32 injection well to assess in-situ stress magnitude and orientation, and kinematic fracture parameters including rupture size and propagation velocity. Thus far we have analyzed moment tensors of M>2 events and finite-source models of five events ranging in magnitude from M 3.7 to 4.5. The scaling relationship between rupture area and moment magnitude of these events resembles that of a published empirical relationship derived for events from M 4.5 to 8.3.

Source Analysis

We have investigated the source mechanisms of several earthquakes associated with the EGS stimulation project using the moment tensor method developed at UC Berkeley (*Minson and Dreger*, 2008). We are presently working through moment tensor solutions of M>2 events utilizing seismic waveforms. The stations are located at distances between three and six km from the source. The velocity data are instrument-corrected and filtered between 0.2 to 1.0 Hz.

Given a moment tensor solution, it is possible to test which of the two possible nodal (fault) planes is the causative plane. For small events related to the EGS stimulation project, it is necessary to consider higher frequencies and therefore the use of theoretical Green's functions based on simple plane layered velocity models is not adequate. Therefore, to derive empirical Green's functions, the waveforms of nearly collocated smaller events are utilized. Mori (1993) demonstrated that the waveform of a smaller earthquake could be spectrally deconvolved from the larger target earthquake yielding an estimate of the seismic moment rate function (MRF). Several MRFs can subsequently be inverted for fault slip, as well as to identify the causative rupture plane. Dreger et al. (2007) applied this approach at Parkfield, California and found that it is possible to obtain finite-source parameters for micro-earthquakes exhibiting rupture complexity, and kinematic parameters that are comparable to their larger counterparts.

Figure 2.36.1 shows the slip distribution of the M_w 3.7 event obtained by deconvolving the records of a nearby M_w 2.5 earthquake. The slip distribution is complex, with three or four asperities being well resolved. The average and peak slips are 4.3 and 26.6 cm, respectively. Using the method of Ripperger and Mai (2004), the slip distribution can be mapped into stress change. The average stress drop over the fault rupture is 11 MPa, with a peak stress drop of 68 MPa. These high stress drops result from the compact nature of the individual slip patches in the rupture model, and demonstrate that the field is under high stress.

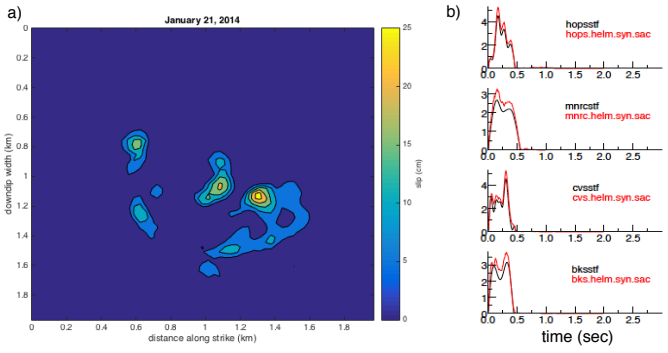

Figure 2.36.1: a) Slip distribution for the January 21, 2014 Mw 3.7 event. The hypocenter is indicated by the white ellipse. b) Observed moment rate functions (black) are compared to synthetics at the four stations: HOPS, MNRC, CVS, and BKS. The amplitudes are proportional to 7.5e19 dyne cm/s.

Thus far we have analyzed the finite-source models of five Geysers events ranging in magnitude from 3.7 to 4.5. One objective of our research is to estimate the coseismic fracture density of the EGS seismicity cloud. This is achieved by first determining moment tensor solutions to obtain focal mechanisms and robust magnitude estimates. Second, suitable target EGF event pairs are found to obtain MRF, which are subsequently inverted for fault slip and the orientation of the causative fault plane. Stress change maps using the method of Ripperger and Mai (2004) may then be determined. Once slip models are available for a number of events over a range of magnitude, the scaling relationship between rupture area and magnitude can be determined.

Figure 2.36.2 shows the scaling of rupture area as a function of magnitude for the five events that we have studied. The data are compared to the empirical area-magnitude scaling relationship of Wells and Coppersmith (1994), which is based on field and aftershock data for events from M 4.5 to 8.3, where the majority of events are in the M 6–7 range. Thus the comparison is very good, considering the substantial extrapolation to lower magnitudes. Nevertheless, the extrapolated relationship is consistent with the rupture area estimates obtained for the five Geysers earthquakes. It appears that four of the five events are collinear. The average stress drops of these events are between 6 and 17 MPa. The largest event (M_w 4.5), which occurred on January 12, 2014, had an average stress drop of 1.6 MPa. Judging from Figure 2.36.2, the relatively low stress drop M_w 4.5 event may be more consistent with the Wells and Coppersmith (1994) scaling relationship, although there are presently too few points to be able to reach reasonable conclusions. Our ongoing work will add additional area-magnitude data for smaller events, followed by corner frequency measurements for each event. We will compare the several other scaling relationships that have been published, as well as regress The Geysers data using both

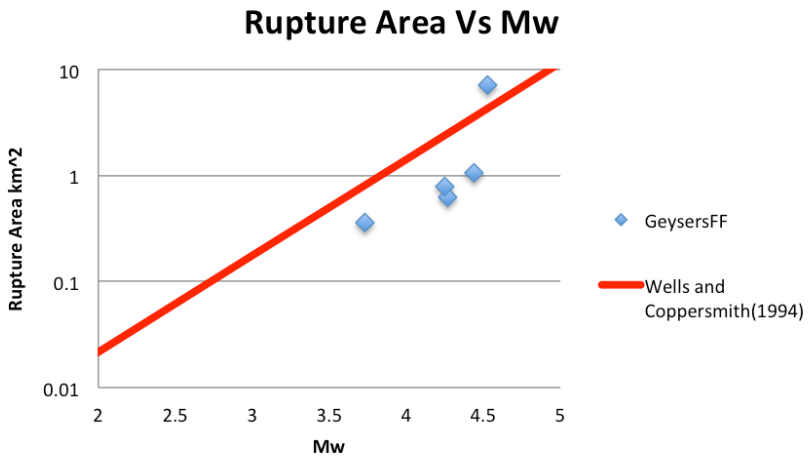

Figure 2.36.2: Relationship between finite-source rupture area and Mw. The diamonds represent the relationship between rupture area and magnitude M_w, as inferred from slip models from finite-source inversion. The red line is an extrapolation of the Wells and Coppersmith (1994) empirical relationship based on field observations of large earthquakes.

magnitude and corner frequency as independent variables. Our thinking is that The Geysers may require an independent scaling relationship, owing to the possibly high state of stress, as well as to the fact that the seismicity is occurring in a system in which pore fluids may have a strong influence on the effective stress. An advantage of finding a relationship between rupture area and both magnitude and corner frequency is that we can account for variations in stress drop for the numerous smaller events where we cannot obtain finite-source models. Using the calibrated scaling relationship and the locations of the events, we will then be able to map the coseismic fracture density of the seismicity cloud associated with the EGS injection.

Acknowledgements

This work is supported by the Assistant Secretary for Energy Efficiency and Renewable Energy, Office of Geothermal Technologies, of the U.S. Department of Energy under Contract No. DE-EE0006766.

References

Dreger, D., Nadeau, R., and Chung, A. (2007), Repeating earthquake finite-source models: Strong asperities revealed on the San Andreas Fault, Geophys. Res. Lett., 34, L23302, doi:10.1029/2007GL031353.

Minson, S. E. and Dreger, D. S. (2008), Stable inversions for complete moment tensor, *Geophys. J. Int.,* 174, 585-592, doi: 10.1111/j.1365-246X.2008.03797.x.

Mori, J. (1993), Fault plane determination for three small earthquakes along the San Jacinto fault, California: Search for cross faults, *J. Geophys. Res*., 98, 17,711–17,722.

Ripperger, J., and Mai, P. M. (2004), Fast computation of static stress changes on 2D faults from final slip distributions, *Geophys. Res. Lett.*, 31(18), L18610, doi:10.1029/2004GL020594.

Wells, D. L. and Coppersmith, K. J. (1994), New empirical relationships among magnitude, rupture length, rupture width, rupture area and surface displacement, *Bull. Seism. Soc. Am.*, 84, No. 4, 974-1002.

37 Resolving Stress Drop Variability with Finite-Source Inversions and its Implications for Earthquake Source Scaling of Repeating Earthquakes

Kathryn Wooddell and Douglas S. Dreger

Introduction

Repeating earthquakes occur in the vicinity of creeping sections along the Parkfield section of the San Andreas Fault (*Nadeau and McEvilly,* 1995) and the Anza section of the San Jacinto fault (*Taira,* 2013). Utilizing an empirical Green's function (eGF) approach, we conduct a comparative study of the slip distributions and derived source parameters for Parkfield and Anza events resulting from finite fault inversions of relative moment rate functions (RMRFs). Trends in fault dimension, average stress, and peak stress as a function of magnitude are examined to draw conclusions about source scaling for micro- and repeating-type earthquakes.

Data and Methods

The approach of Dreger et al. (2007) is used to compute RMRFs at each station for the 11 March 2013 M_w4.7 Anza repeater (33.502, -116.457) using a spectral domain deconvolution approach (*Clayton and Wiggins,* 1976) where the complex spectrum of the eGF is divided out of the complex spectrum of the target event. Spatial distributions of fault slip are derived from inversion of the RMRFs following Mori and Hartzell (1990), and the coseismic stress change is computed following the method of Ripperger and Mai (2004). Results are compared against the eGF Finite-Fault Inversion results of Dreger et al. (2011) for a dataset including Parkfield repeaters and non-repeaters ranging from M_w1.8 to 6.0.

The Parkfield dataset of Zechar and Nadeau (2012) is a catalog of repeating event clusters compiled from the Berkeley High Resolution Seismic Network (HRSN) and the San Andreas Fault Observatory At Depth (SAFOD) where every repeating event is assigned to a cluster containing earthquakes with a characteristic repeat time and nearly identical magnitudes and waveforms, implying nearly identical source mechanisms. Anza events are well recorded on the high quality Plate Boundary Observatory Borehole Seismic Network (PB). Catalogs of Anza repeating earthquakes have been compiled by Taira (2013).

Results

Slip distributions for the M_W4.7 Anza target event were obtained using three distinct eGF events located close in both space and time to the target event (Table 2.37.1). The preferred slip model for eGF8 is shown in Figure 2.37.1. The total slip area of the solution is 3.2 km^2. If only the area of slip greater than 10% of the peak slip is considered, the area is 1.6 km^2. Peak slip is 62.1 cm and the average over slips greater than 10% of the peak slip is 19.5 cm.

Final model parameters were selected based on sensitivity analyses on model smoothing parameter, rupture velocity, and rise time (Table 2.37.2). Variance reduction at each of the stations ranges from 83.8 to 97.9, leading to an overall variance reduction of 93.2 for our preferred solution. Our model suggests unilateral rupture and directivity in the northwest direction.

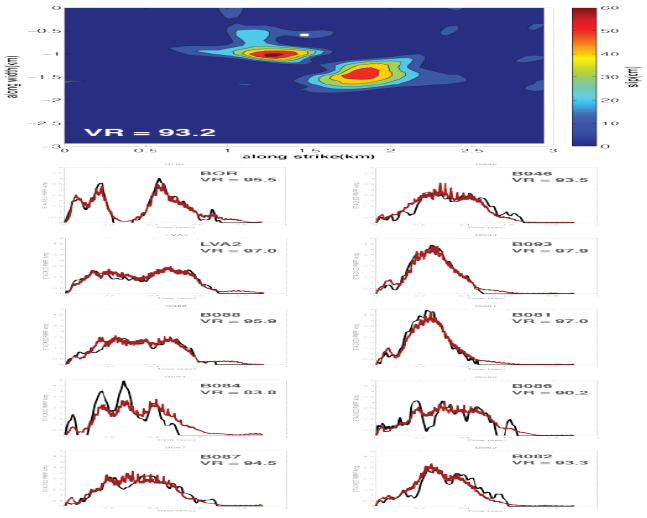

Figure 2.37.1: Preferred slip model for eGF8 using parameters in Table 2.37.2. The hypocenter is shown with a white square.

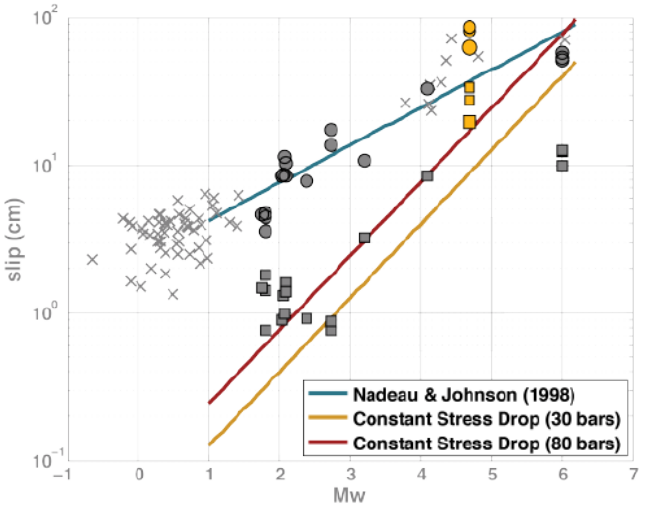

Figure 2.37.2: Slip scaling for peak slip (circles) and average slip (squares). Grey circles show the peak slip from the inversion of RMRFs using the eGF finite-fault inversion, and grey squares show the slip averaged over the primary asperity (Dreger et al., 2007). Grey X symbols are values for repeating events by Nadeau and Johnson (1998) using a tectonic loading model.

Conclusions

Solutions for the three target – eGF pair solutions are com-

EVENT	MAG	DATE	TIME	LATITUDE	LONGITUDE	DEPTH (km)	DIST FROM TARGET (km)
eGF2	2.58	3/11/13	16:36:12.65	33.504	-116.463	12.4	0.922
eGF3	2.21	3/11/13	16:51:09.96	33.503	-116.460	9.1	4.010
ANZA TARGET	4.7	3/11/13	16:56:06.04	33.502	-116.457	13.1	0.000
eGF8	2.73	3/11/13	19:50:07.43	33.505	-116.466	11.8	1.580

Table 2.37.1: Event Information for the Anza Target event and three potential eGF earthquakes.

PREFERRED MODEL PARAMETERS	
Grid size:	0.6 X 0.6
Smoothing:	200
Vs (km/s)	3.64
Vr (km/s)	3.276
Rise Time (s):	0.03

Table 2.37.2: Preferred model parameters

pared against the Nadeau and Johnson (1998) tectonic loading model, models for constant stress drop, and finite-fault inversion results of Dreger et al. (2011) (Figure 2.37.2). Peak slip results from this analysis are more consistent with the peak Parkfield slips and the Nadeau and Johnson tectonic loading model, while average slips are more consistent with the average Parkfield solutions and tend to suggest a constant stress drop model. The three target eGF – pair solutions demonstrate the uncertainty associated with using different eGFs to remove path effects. Preliminary results of Parkfield and Anza repeaters suggest that micro- and repeating earthquakes scale self similarly across all magnitudes, but with a high mean stress drop.

We interpret the repeating earthquakes at Parkfield and Anza as ruptures of single asperities. We hypothesize that stress on these high-strength asperities is released over a limited area leading to a population of earthquakes that, on average, exhibits high stress drop.

References

Clayton, R. and R. Wiggins (1976), Source shape estimation and deconvolution of teleseismic bodywaves, *Geophys. J. R. astr. Soc.*, 47, 151 - 177.

Dreger, D. et al. (2011), Finite-Source Parameters and Scaling of Repeating and Non-Repeating Earthquakes at Parkfield, *Annual Meeting of the Seismological Society of America*. April 13-15, Memphis, Tennissee.

Dreger, D. et al. (2007), Repeating earthquake finite source models: Strong asperities revealed on the San Andreas fault, *Geophysical Research Letters*, 34, L23302.

Mori J. and S. Hartzell (1990), Source Inversion of the 1988 Upland, California, Earthquake: Determination of a Fault Plane for a Small Event, *Bulletin of the Seismological Society of America*, 80, 507 - 518.

Nadeau, R. and T. McEvilly (1997), Seismological Studies at Parkfield V: Characteristic Microearthquake Sequences at Fault-Zone Drilling Targets, *Bulletin of the Seismological Society of America*, 87, 1463 - 1472.

Nadeau, R. and L. Johnson (1998), Seismological Studies at Parkfield VI: Moment Release Rates and Estimates of Source Parameters for Small Repeating Earthquakes, *Bulletin of the Seismological Society of America*, 88, 790 - 814.

Ripperger, J. and M. Mai (2004), Fast computation of static stress changes on 2D faults from final slip distributions, *Geophysical Research Letters*, 31, L18610.

Taira, Taka'aki (2013), Finite-Source Modeling and Stress Drop Estimates of Anza Microearthquakes: Implications for Fault Strength and Earthquake Nucleation, *2013 SCEC Proposal*.

Zechar, J. and R. Nadeau. (2012), Predictability of repeating earthquakes near Parkfield, California, *Geophysical Journal International*, 190, 457-462.

38 Local Magnitude Correction in California and Vicinity

Clay Miller, Peggy Hellweg, Bob Uhrhammer

Introduction

In an ideal world, every seismic station that records an earthquake would give the same magnitude for that event. In reality however, the magnitude reported by each station and even each component of each station varies for any given event. This can happen for many different reasons, most notably, the geology on which the station is located. A station on hard rock for example will generally have higher amplitude ground motions than a station situated on soft, loose soil. This variance in ground motion will, of course, create different peak amplitudes and so therefore magnitudes.

It is important to understand and calculate the variations in magnitude for consistent magnitude reporting across California and event size. The goal of this project is to determine a median magnitude correction for each component at stations in 10 networks in California and its vicinity.

Background

This work is a continuation of the work started in 2006 by Bob Uhrhammer (*Uhrhammer et. al*, 2011). In that work, *Uhrhammer et. al* looked at the horizontal components at numerous stations to try and determine magnitude adjustments (dM_L). This was done by taking seismic data, converting it to a Wood-Anderson (WA) synthesized response and filtering it from 0.5 to 10 Hz with a bandpass butterworth filter. Then taking the maximum amplitude of the new waveform. Magnitude can then be calculated as follows:

$$M_L = \log(A) - logA_0(r)$$

where A is the maximum WA trace amplitude, measured in mm, r is the hypocentral distance in km, and $\log A_0$ is the attenuation function.

The next step in the dM_L determination is, for each event, to compare the computed magnitudes for each component across all stations and components, then calculate the differences. So if there are three stations with three components (a total of nine computed M_Ls), an M_L is compared with the eight other M_Ls. This process is repeated for all components, then repeated for each event. The result is a large set of differential magnitudes, the median of which is used as the dM_L.

Method

The goal of this project is to continue the work done by Bob Uhrhammer to include vertical components and include more stations and components.

We gathered data from around the state for events in two magnitude ranges: M1.9 - 2.2 and M3.3 - 3.5. For each event, we query seismic databases to send us back data for an appropriate time range surrounding the event. This can lead to noisy data, or even data that has no event signal on it at all. In order to deal with bad data, we impose a certain selection criteria to weed out real event data from noise.

The first set of criteria is minimum amplitude and maximum period thresholds for each instrument type. Unfortunately, this does not eliminate all bad data. We then invoked a hypocentral distance criterion to ensure that data is not being collected too close or too far away from the event. We decided that for low magnitude events, the station had to be between 1 and 100 km from the source and for the larger magnitude events, the station had to be between 1 and 500 km.

The next step of the project is to compute the differential magnitudes for each component or each station. We computed this in a similar manner as *Uhrhammer et. al*, 2011. However, rather than taking the differential magnitudes between all components for an event, we only compare magnitudes between the component with the dM_L computed from the previous study and the component where the dM_L is unknown. Thus, for the component with a known dM_L, we took that component's raw magnitude, added the magnitude correction (dM_L) which gives us a fairly good magnitude against which we can compare other components. To ensure that only the best signal-to-noise ratio waveforms are being used in the dM_L calculations, we only use data from high magnitude events to compute the differential magnitudes. There are 666 known dM_Ls from the previous study, giving us ample stations to use in our comparisons.

Results

The previous method yields 1908 new dM_Ls at 811 unique stations. We need to verify that these new dM_Ls are a valid adjustment to a component's magnitude determination. To determine our dM_L quality, we look at a component's magnitude calculation before and after adding the dM_L. To simplify the results we looked at the differences between the catalog magnitude for an event, and each component's corrected magnitude and raw, uncorrected magnitude. Ideally, our dM_L corrections will adjust the raw magnitude and bring it very close to the catalog magnitude. Thus, we expect to see near 0 values when the catalog magnitude is subtracted from the corrected magnitudes.

Figure 2.38.1a shows a histogram of these values for horizontal components (denoted as uk) that does not have a dM_L computed in the previous study. As is shown in Figure 2.38.1a, the median magnitude difference for raw magnitudes of the horizontal components is 0.235. In other words, raw magnitudes are underestimated by 0.235. Physically, this is interpreted as the stations generally being on hard rock, so have decreased amplitudes and thus their reported magnitudes are not as large. When we add dM_L corrections, the median difference goes down to 0.0351. This number is very close to 0, assuring us that our dM_L values are adjusting a component's raw magnitude much closer to the catalog value.

Another great result is the reduction in standard deviation. Prior to the correction, the standard deviation was ~0.51 and

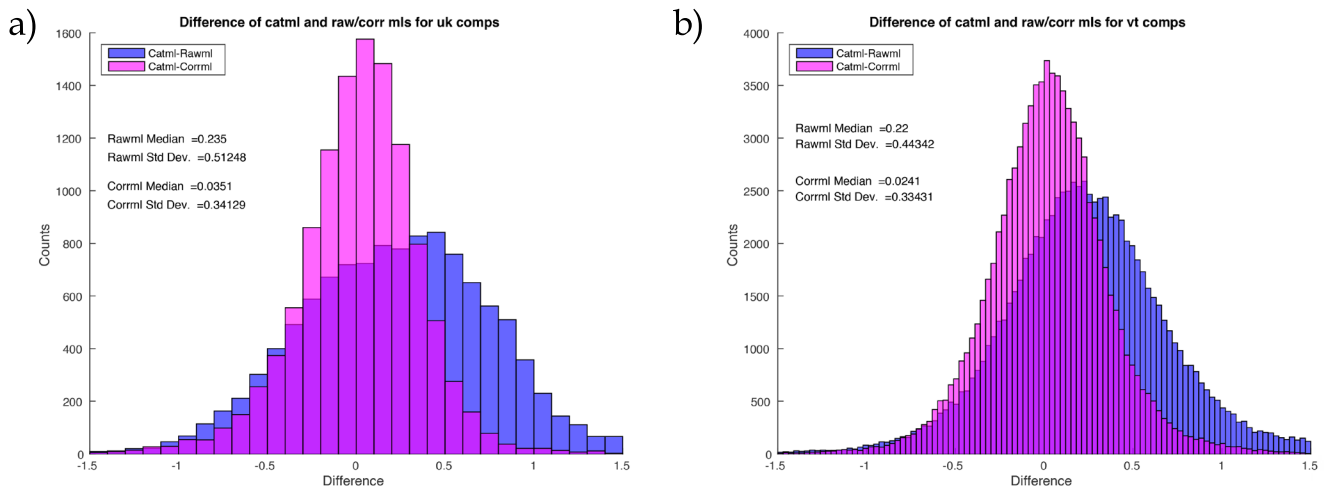

Figure 2.38.1: These figures show the differences between the catalog ml (Catml), the raw magnitude (Rawml, blue) and the corrected magnitude (Corrml, magenta) for horizontal components (plot a, here noted as uk) and vertical components (plot b, here noted as vt). This histogram shows the aggregate results for all components and all events.

after it is dropped to ~0.34. Both of these results mean that our magnitudes are not only shifting closer to the catalog magnitudes, but also are clumping together more.

We see similar results when we look at the histogram for vertical components (denoted as vt) in Figure 2.38.1b. Prior to magnitude corrections, the components reports a median magnitude that is lower by 0.22. After the corrections, the difference between the catalog magnitude and corrected magnitude is lowered to 0.0241. Additionally, the standard deviation drops from ~0.44 to ~0.33 with dM_L corrections.

Conclusions

Through the comparison of a station's components with a previously calculated magnitude adjustment, we can determine a unique magnitude adjustment for each component at stations throughout California. This will help magnitude reporting consistent across the state and instrument types.

Acknowledgements

We are thankful to Stephane Zuzlewski for help in creating instrument response files used in the analysis.

References

Uhrhammer et. al, (2011), California Integrated Seismic Network (CISN) Local Magnitude Determination in California and vicinity, *Bulletin of the Seismological Society of America*, 101, 2685-2693, doi: 10.1785/0120100106.

Research Studies:
Enhancements to Observational Systems

40 GPS and Earthquake and Tsunami Hazards

Diego Melgar

Geodesy for Hazards

High-rate GPS is increasingly playing an important role in the way we respond to large earthquakes. The modern way to conceptualize the role of GPS in seismology is as a long-period displacement strong motion sensor. Although this is noisier than traditional inertial sensors, it is suitable for the study of medium to large earthquakes. This was demonstrated by the 2014 M_w6.0 Napa, California earthquake which was recorded by many stations of the Bay Area Regional Deformation network (BARD), which is operated by the BSL, as well as by other regional networks. Research into this event, published in Melgar et al. (2015a) showed that this magnitude level represents the lower threshold of earthquake size for which GPS can play an important role. There, we showed that GPS can contribute to the rapid estimation of the basic characteristics of the source and aid in the elaboration of rapid products such as moment tensors and static and kinematic slip inversions.

The importance of GPS was further demonstrated during the 2015 M_w7.8 Gorkha, Nepal earthquake. For this event there was only a single seismic station in the immediate vicinity of the source and eight high-rate GPS stations. In *Galetzka et al.* (2015), we showed how GPS, with the assistance of other space geodetic technique such as InSAR, is crucial for the characterization of kinematic properties of the event. Had GPS not been available, we would have had little information on the ground motion characteristics of the event.

Reliable Magnitudes for Large Events

An interesting and impactful contribution of GPS displacement seismograms is their application to the rapid computation of magnitudes for large events. It has long been known that as events get larger, systems that rely only on inertial seismometers become "saturated." This has the effect of magnitudes being systematically underestimated for events larger than roughly M_w7. Through a systematic analysis of large events that have been recorded by regional GPS networks around the world, we were able to show in Melgar et al. (2015b) that saturation does not become an issue if GPS waveforms are included in the magnitude calculation. This is illustrated in Figure 2.40.1. Here we show the measurements of peak ground displacement (PGD) for 10 large events. The plot shows that, broadly speaking, as an event gets larger, the values of PGD at a given distance from the source will also be larger. This simple observation can be leveraged for rapid magnitude calculation.

We perform a regression on the PGD observations and find that magnitude is related to PGD and source distance R by the logarithmic law shown in the title of Figure 2.40.1. Once this equation is known and as a large earthquake unfolds, we can estimate magnitudes from rapid measurements of PGD at near-source GPS sites.

An example of this is shown in Figure 2.40.2 for two large events that produced significant tsunamis, the

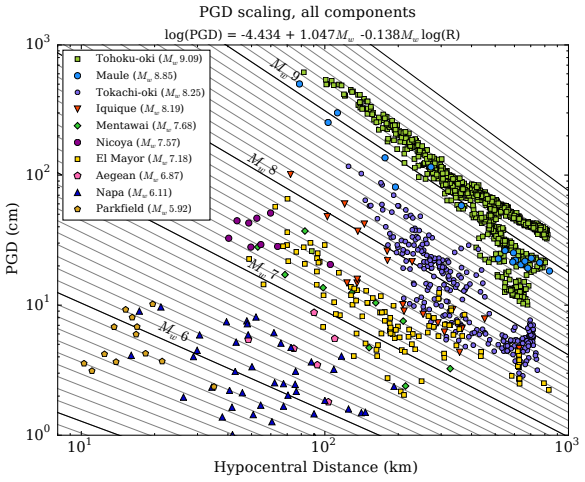

Figure 2.40.1: Peak ground displacement (PGD) measurements for 10 large events recorded around the world. Plot clearly shows that larger event have larger values of PGD, this can be used for rapid magnitude determination.

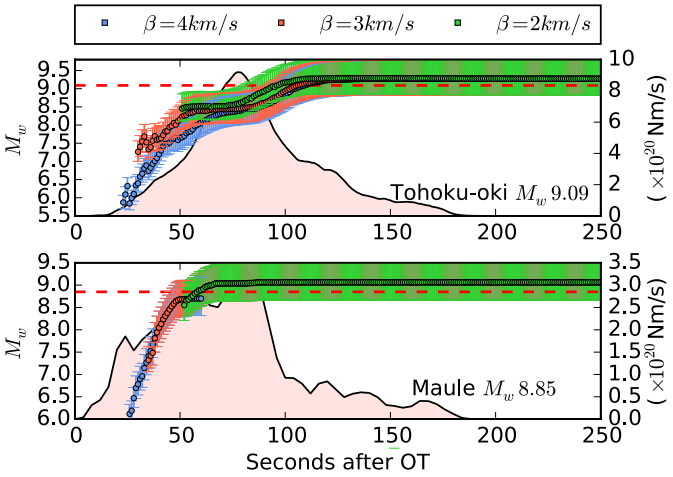

Figure 2.40.2. Rapid magnitude calculation using the scaling law from Figure 2.40.1. Plotted are magnitude calculations using 3 travel time masks at 2, 3 and 4 km s^{-1}. Error bars are determined using uncertainties of the regression coefficients. Red dashed line is the "true" magnitude from the slip inversion for that event. Shaded pink regions are the source time functions for the kinematic slip inversions.

2010 M_w8.8 Maule, Chile and 2011 M_w9.0 Tohoku-oki, Japan earthquakes. The results are striking. For both events saturation was a problem in the real-time operational setting. Had GPS been available, the magnitude would have been correctly calculated and the level of tsunami warning better determined. This result is also important because it shows that the method can be used for both very dense and very sparse networks with good results. In the 2011 M_w9.0 Tohoku-oki, Japan case, over 800 GPS stations contribute to the magnitude estimate while in the 2010 M_w8.8 Maule, Chile case, only 6 GPS sites were used for the magnitude calculation.

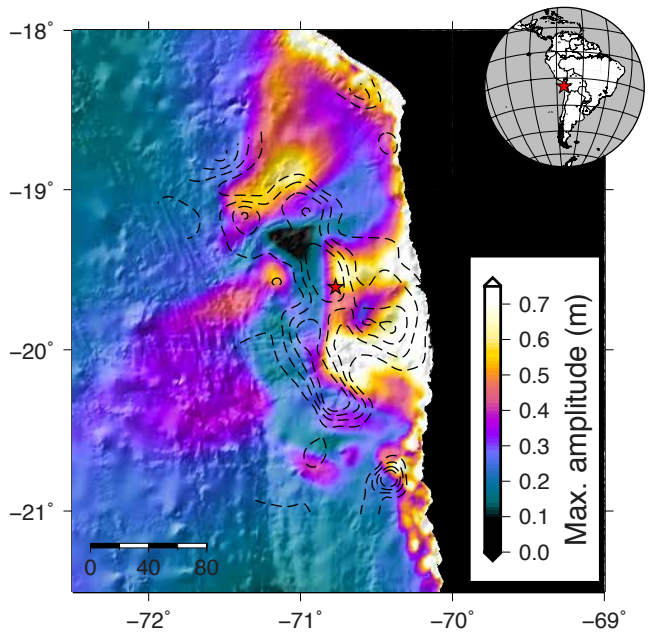

Figure 2.40.3. Rapid model of expected tsunami intensity for the 2014 M_w8.1 Iquique earthquake off the coast of northern Chile. This model results from slip inversion (dashed contours) produced from the joint inversion of high-rate GPS, strong motion and tide gauge data.

Plots like Figure 2.40.2 for events as small as M_w5.9 are shown in Melgar et al. (2015b). It shows the reliability of the GPS-PGD approach to magnitude calculation for events between M_w5.9 - 9.0.

Tsunami Intensity Forecasts

Currently only Japan has a tsunami warning system capable of issuing warnings in the shore immediately in response to large earthquakes. However, a strict reliance on seismic instruments led to an under-prediction of the tsunami intensity in the first tens of minutes after the 2011 M_w9.0 Tohoku-oki event.

It has long been argued that source inversions, whatever their level of complexity, can be utilized to guide near source warnings, however, the issue of how to couple a source product to a tsunami propagation model remained unresolved. The Tohoku-oki event allowed us to test this warning paradigm. In Melgar and Bock (2015), we demonstrated that earthquake slip inversions, particularly if they include on-shore GPS and offshore tsunami wave measurements, can be coupled to hydrodynamic propagation codes and provide reliable forecasts of the expected tsunami intensity well in advance of it reaching the coast.

Building on this success, we have continued this line of research. We are particularly interested in testing the performance of this warning paradigm, where rapid knowledge of the earthquake source guides tsunami warnings. We have benefited from a fruitful collaboration with colleagues at the Centro Sismológico Nacional in Chile, who have provided us access to GPS, seismic and tsunami data for the 2010 M_w8.8 Maule, Chile and 2014 Iquique tsunamis, in order to further test these methods.

Figure 2.40.3 shows the expected tsunami amplitude from a slip inversion of the 2014 M_w8.1 Iquique earthquake, which includes onshore GPS and strong motion data, as well as tide gauge information. The results show that if seismic, geodetic and oceanographic information is available in real-time, it is reasonable to expect detailed maps of the expected tsunami amplitude in advance of its arrival to the near-source coastline.

The results for the larger 2010 M_w8.8 Maule, Chile event, which also produced a substantial tsunami, are equally encouraging. We are in the process of assessing the reliability of these rapid tsunami models by comparing them to post-event survey measurements, which serve as a ground truth and can then be used to determine the predictive power of our model.

We are also evaluating ways to speed up the tsunami propagation computation, which is the slowest, computationally, link in the process chain. We expect fairly complex models of tsunami propagation are feasible with modest computational resources.

Overall, the results of the rapid tsunami models for the 3 large events, M_w8.1 Iquique, M_w8.8 Maule and M_w9.0 Tohoku-oki argue that a new paradigm in tsunami warning is possible for near-source regions. We posit that rapid models of the earthquake source can reliably guide warning for coastal communities immediately adjacent to large earthquakes.

As there already exist multiple monitoring groups that produce rapid earthquake source products in the west coast of the U.S., we plan to soon begin a detailed scenario study of the feasibility of this warning technique for the Cascadia subduction zone. The Cascadia mega-thrust has a documented history of large ruptures and tsunamis. We believe that these warning techniques can be adopted by using current geophysical infrastructure without any need to expand the current monitoring networks, in order to provide timely warnings in the event of a large tsunami.

Acknowledgements

This research was funded by the Gordon and Betty Moore Foundation through grant GBMF3024 to UC Berkeley.

References

Galetzka, J., Melgar, D., Genrich, J.F., et al., (2015), Slip pulse and resonance of Kathmandu basin during the 2015 M_w 7.8 Gorkha earthquake, Nepal Imaged with Space Geodesy, *Science*, in review.

Melgar, D., & Bock, Y. (2015). Kinematic earthquake source inversion and tsunami runup prediction with regional geophysical data. *Journal of Geophysical Research: Solid Earth*, 120, 3324–3349. doi: 10.1002/2014JB011832.

Melgar, D., Geng, J., Crowell, B. W., Haase, J. S., Bock, Y., Hammond, W. C., & Allen, R. M. (2015a). Seismogeodesy of the 2014 M_w6.1 Napa earthquake, California: Rapid response and modeling of fast rupture on a dipping strike-slip fault. *Journal of Geophysical Research: Solid Earth* 120, doi: 10.1002/2015JB011921.

Melgar, D., Crowell, B. W., Geng, J., Allen, R. M., Bock, Y., Riquelme, S., Hill, E.M., Protti, M. & Ganas, A. (2015b). Earthquake magnitude calculation without saturation from the scaling of peak ground displacement. *Geophysical Research Letters*, in press.

41 Implementing ElarmS Earthquake Early Warning Algorithms for the National Seismic Network in Israel.

Ran Novitsky Nof and Richard Allen

Introduction

Israel is located in proximity to the Dead Sea Transform (DST)—a tectonically active plate boundary fault system. The DST is considered to potentially produce earthquakes with maximal magnitudes of M7.5–M7.8 (*Hamiel et al.*, 2009). Based on paleoseismic, historic, and instrumental records (*Levi et al.*, 2010), recurrence times are on the order of 100 and 1000 years for an M6 and M7 earthquake, respectively. The recent most destructive earthquake along the DST was the 1927 ML 6.2 (*Shapira et al.*, 1993). Given the growth in population during the past century and the expected return time of such an earthquake, the increased seismic risk for Israel has led the Israeli government to establish a short term Earthquake Early Warning System (EEWS) for Israel.

Following recommendations of an international committee (*Allen et al.*, 2012), the proposed system would include an upgrade to the current Israeli Seismic Network (ISN), adding ~100 new stations, or strong motion accelerometers and broadband velocity instruments along the major fault line of the DST and its Carmel fault branch (*Pinsky*, 2015). The data collected is to be processed by an EEW algorithm to deliver rapid alerts for potentially damaging earthquakes.

The prime objective of the current research is to implement and validate the Berkeley Seismological Lab (BSL) EEWS ElarmS, for the Israeli Seismological Network (ISN). ElarmS is highly customized to California and its various real-time networks. This localized customization includes many parameterizations and models, such as the relationship equations of the main magnitude proxy of maximal displacement (Pd), the fixed events depth at 8 km, a velocity model for the California region, *etc.*

The main challenge of this research is to identify, verify, and finally adjust the various localization dependent parameters for the Israel region. These goals are achieved by running the ElarmS system using data from the Israeli network in different modes: (1) Real-time (RT) data: processing the current ISN data collected at the Geophysical Institute of Israel (GII) continuously; (2) Historical Playbacks: processing achieved data and historic records collected at the GII; (3) Simulations playback: processing simulated data playbacks for various earthquake scenarios.

Below, we present an initial analysis of a short period of RT processing and historical data playback.

Real-Time Performance

ElarmS has been successfully set up at the GII on a testing server, since November 2014. However, due to code changes and adjustments, RT results are analyzed only between April 30, 2015 and May 4, 2015. Therefore, we note that the presented analysis is limited and partial. As this is ongoing research, more analysis of the RT performance will be performed periodically in the future.

ISN Latencies, Delays, and Alert Times

Latencies are defined here as the difference between the time of the last measurement sample in a waveform packet and the arrival time of this packet to the acquisition system buffer. At BSL, the telemetry latency of most of the networks is less than 2 s, except for the UCSD Anza network of which the median latency is 4.6 s. Most of the packet sizes are of 1 s (*Kuyuk and Allen*, 2014).

ISN latencies are mostly below 4 s (2.9 s mean). Longer latencies are introduced with additional stations acquired from the Jordanian Network (8.4 s mean) and Geophone Network (5.4 s mean). However, despite the reasonable latencies, packet spans are within a range of 1 s to 9 s (6 s mean) for the ISN stations, leading to a potential alert delay of ~10 s.

During the period analyzed, no false alerts were issued. Typically for ISN, an ElarmS alert is issued at around 800 milliseconds after the arrival of the last packet containing the needed trigger to declare an event (minimum of four triggers are needed). For the period analyzed, alert times are in the range of 10 s to 1 min, with an average of 30 s, depending on hypocentral distance and trigger latency. Alert times are expected to decrease as data packets and latencies will be reduced in the future as the ISN will be upgraded.

Historical Data Playbacks

Based on 60,000 years of prehistoric-paleoseismic, historic, and instrumental record (*Hamiel et al.,* 2009) along the DST, recurrence times of earthquakes with M>4.5 and M>5 are five years and 15 years, respectively. Thus, using historical data is essential for evaluating the ElarmS algorithm in Israel. For California, ElarmS performance analysis is usually done by assessment of the RT processing performance due to higher seismicity.

The ability to run historical data in real-time or accelerated time has been made available within ElarmS under this research. We note that playbacks can only be used to evaluate ElarmS performance under different scenarios and may not be used for reproducing the exact chain of processing as in RT.

Playback Results

Data of 39 events from the GII catalog were processed in playback mode. The dataset includes events, categorized as earthquakes by GII analysts, with a magnitude range of M_d>3.0, occurring from February 2012 to May 2015, and in geographical boundaries of 29 to 34.5 deg latitude and 33 to 37 deg longitude. ElarmS was set with similar parameters as used by BSL and was only adjusted with the different stations parameters.

Of the 39 events, 36 triggered and an alert was issued by

ElarmS; two missed events were triggered, but did not issue an alert due to low estimation of magnitude (M<2); one missed event did not trigger (only three stations triggered). Two false events were also generated with an alert issued based on S-wave triggers. Since only short time windows of data spanning catalog events were used, false event triggering is not fully tested yet.

While ElarmS updates event solutions continuously as new data arrives, improving the solution accuracy, here, only the first ElarmS alert is considered since the initial alert is expected to have the most impact on the earthquake mitigation actions taken. Magnitude estimations show underestimation for most of the events with no apparent correlation with signal to noise ratio. Misfit is in the range of ±1 with a mean underestimation of 0.74 magnitude units and a standard deviation of 0.47, similar to standard deviations from Californian results (K*uyuk and Allen*, 2014). While the median location error is 15 km, 25% exceed 50 km, mostly outside of the network. Similarly, the median origin time error is 1.5 seconds, with 25% of the solutions exceeding five seconds.

In light of these results and the small amount of events tested here, a further investigation of the magnitude and location misfits is required to understand its origin to better adjust ElarmS for the Israeli EEWS.

Conclusions

The initial analysis shown in this study, highlights the importance of low latencies and the advantage of small data packets. An effort should be made to minimize arrival times of data to the processing center in any future planning of the Israeli seismic network.

As observed by the current research, ElarmS is compatible with the current ISN and additional external stations. However, more research is needed in order to optimize ElarmS to the Israeli region and seismic network. The underestimation of the magnitudes from the historical data might be a result of one or more misadjusted parameters such as velocity model, instrument gains, or Pd to magnitude relations. Current historical playback results are biased towards low magnitudes. Additional historical data should be obtained and processed for more complete magnitude coverage. A better estimation of the Pd to magnitude parameters should be performed with unbiased data. In addition, longer periods of noise should be processed to better estimate the ElarmS false event conditions and rate. For example, a known problem of the algorithm is S-wave picking (*Hanson*, pers. comm.) leading to false events detections occasionally. Currently an effort is made at BSL for finding a more robust triggering method.

Acknowledgements

This research is supported by the Geological Survey of Israel, at the Earth and Marine Sciences Research Administration, the Ministry of Energy and Water Resources. Data was supplied by the Seismological Division at the Geophysical Institute of Israel.

References

Allen, R. M., Baer, G., Clinton, J., Hamiel, Y., Hofstetter, R., Pinsky, V., Ziv, A., Zollo, A. (2012), Earthquake early warning for Israel: Recommended implementation strategy, *Report GSI/26/2012, Geological Survey of Israel*, Jerusalem.

Hamiel, Y., Amit, R., Begin, Z.B., Marco, S., Katz, O., Salamon, A., Zilberman, E., Porat, N., (2009), The seismicity along the Dead Sea Fault during the Last 60,000 years, *Bulletin of the Seismological Society of America*, 99, 2020–2026, doi:10.1785/0120080218.

Kuyuk, H.S. and Allen, R. M. (2014), Designing a Network-Based Earthquake Early Warning Algorithm for California: ElarmS-2 *Bulletin of the Seismological Society of America*, 104, 162-173, doi:10.1785/0120130146.

Levi, T., Tavron, B., Katz, O., Amit, R., Segal, D., Hamiel, Y., Bar-Lavi, Y., Romach, S., Salamon, A. (2010), Earthquake loss estimation in Israel using the new HAZUS-MH software: preliminary implementation, *Report GSI /11/2010, Geological Survey of Israel*, Jerusalem.

Pinsky, V. (2015), Modeling warning times for the Israel's earthquake early warning system, *Journal of Seismology*, 19(1), 121–139, doi:10.1007/s10950-014-9454-z.

Shapira, A., Avni, R. and Nur, A. (1993), A new estimate for the epicenter of the Jericho earthquake of 11 July 1927, *Israel Journal of Earth Sciences*, 42, 93–96.

42 San Andreas Fault Seismo-Electromagnetic Monitoring System

Jonathan M. G. Glen, Simon L. Klemperer, Darcy K. McPhee, Lilianna E. Christman, Chen Bin

Introduction

The U.S. Geological Survey (USGS), Stanford University, and the Berkeley Seismological Laboratory (BSL) are collaborating on an effort to establish and maintain a network of local and remote-reference, high-precision ground-based electromagnetic (EM) monitoring stations in northern California to determine the validity of pre-seismic, co-seismic and post-seismic ULF (ultra-low frequency; 0.01-10 Hz) EM signals. Each site in the network (Figure 2.42.1) has three orthogonal magnetometers (sensitive to 0.001 Hz), and duplicate sets of two orthogonal horizontal electric dipoles (100 m separation). We are recording at a 40 Hz sample rate, and all our stations are collocated with existing broadband seismic recorders, to allow us to identify vibration-induced signals and separate them from true telluric signals. All data are telemetered to UC Berkeley, and there made publicly accessible through the Berkeley Digital Seismic Network (BDSN) and the Northern California Earthquake Data Center (NCEDC).

In addition, one of our sites (JRSC, see Figure 2.42.1) includes a G-881 cesium magnetometer system, installed and maintained by our collaborators at Geometrics Inc., that records absolute total magnetic field with a sensitivity of 0.5 nT peak-to-peak at 0.1 s sample rate, and absolute accuracy better than 3 nT. This magnetometer is being logged through an entirely separate recording system to provide an independent and redundant measurement to complement our three-axis coils. These data are available from ftp://geom.geometrics.com/pub/mag/JasperData/ as a daily archive.

This project has involved numerous Stanford undergraduates and IRIS interns, each of whom has presented their work at national meetings. In addition, we recently hosted a post-doctoral candidate from China to work on data processing. In the past, our effort has focused on improvement of station design, development of instrumentation, development of software for data processing and analysis (*Kappler at al.*, 2013), and the design of a web-accessible interface (http://ulfem-data.stanford.edu/) for near real-time, data viewing and access. Currently, our focus has shifted to data analysis, and we describe two research projects carried out in 2014-2015 below.

Comparison of Two ULF EM Systems at JRSC

Two independent ULF EM networks now operate in the greater San Francisco Bay Area, those managed by USGS-Stanford-BSL and by Quakefinder, Inc. A comparison of systems from each network will help validate data and studies such as those presented below (see "Assessment of a claimed ULF EM earthquake precursor" section). A study was conducted at Jasper Ridge Biological Preserve (Stanford University) where systems from each network were co-located and collected continuous magnetic field data for six weeks. The systems were set up ~50 m from each other and away from obvious noise sources, such as buildings and power lines. The JRSC system was comprised of Schlumberger BF-4 induction coils (0.001-1000 Hz), recording at 40 Hz, digitized on a Quanterra Q330 and powered by an isolated battery system charged by line power. The Quakefinder system was comprised of Zonge ANT-4 induction coils (0.001-1000 Hz), as well as QFido3 sensors, that have a lower preamplifier gain. Quakefinder data recorded at 50 Hz and were digitized using a Symmetric Research Inc. digitizer and powered by batteries charged by solar panels. Each system measured the east and north component of the magnetic field.

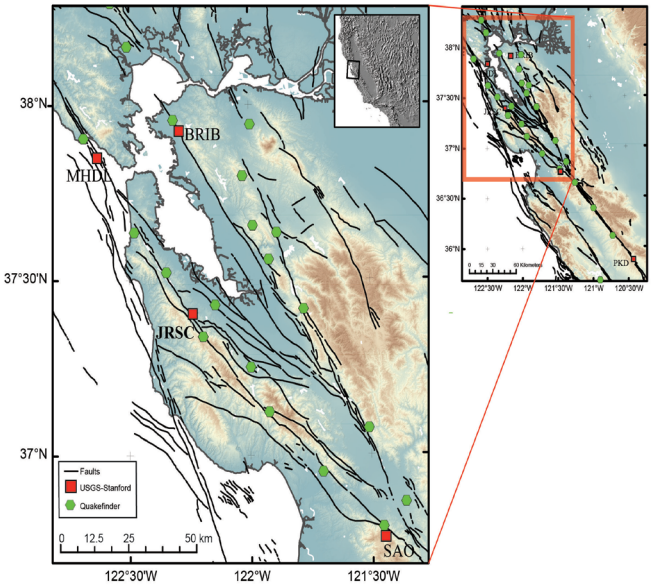

Figure 2.42.1 ULFEM arrays managed by USGS-Stanford (red squares) and Quakefinder (green circles).

The study showed that both ULF EM systems have similar response functions and comparable noise and drift characteristics, however the QFido3 sensors were less sensitive than the BF-4 and ANT-4 sensors. In rare instances, signals were observed on one system but absent on the other, indicating either system noise or extremely local site phenomena. We also observed signals present on a single sensor that were absent on other sensors, even within the same system. We are presently engaged in an effort to characterize these signals and isolate their source. Preliminary results of this study were presented at the 2014 Fall AGU meeting (*Chen et al.*, 2014). A more in depth analysis is currently being developed for publication.

Assessment of a Claimed ULF EM Earthquake Precursor

Anomalous ULF EM pulses occurring before the M5.4 2007 and M4.0 2010 Alum Rock earthquakes have been claimed by Bleier et al. (2009) and Dunson et al. (2011), respectively; they report an increase in the number of pulses days to weeks prior to the earthquake. We re-examined the ULF magnetic data studied by Bleier et al. (2009) and Dunson et al. (2011), record-

ed at a QuakeFinder site located 9 km from the earthquake hypocenter, as well as data from JRSC (Figure 2.42.1), a nearby Stanford-USGS-BSL site located 42 km from the hypocenter, to analyze the characteristics of the pulses and asses their origin.

In this study, we developed and used pulse definitions and pulse-counting algorithms analogous to those of Bleier et al. (2009), and although we corroborate the increase in pulse counts before the 2007 Alum Rock earthquake at the QuakeFinder station, we find that the majority of pulses do not match temporally, indicating the pulses are not from solar-driven ionospheric/magnetospheric disturbances or from atmospheric lightning. Furthermore, our assessment of the temporal distribution of pulse counts throughout the day shows pulse counts increase during peak human activity hours, strongly suggesting these pulses result from local cultural noise and are not tectonic in origin. A manuscript outlining these results is currently in review.

Acknowledgements

We are grateful for funding and support from NASA Grant #05-ESI/05-0071, U.S. Geological Survey, Berkeley Seismological Laboratory, Stanford School of Earth Sciences, Quakefinder, Inc., IRIS Internship Program, NSF-Earthscope, China Scholarship Council's State Scholarship Fund, and Stanford University's SURGE Internship program.

References

Bleier, T., Dunson, C., Maniscalco, M., Bryant, N., Bambery, R. & Freund, F., 2009, Investigation of ULF magnetic pulsations, air conductivity changes, and infrared signatures associated with the 30 October Alum Rock M5.4 earthquake, Nat. Hazards Earth Syst. Sci., 9, 585–603, doi:10.5194/nhess-9-585-2009.

Chen, B., Glen, J.M.G., Klemperer, S.L., Christman, L., Bleirer, T., Dunson, J.C., DeKlotz, M. , 2014, Progress in evaluating potential EM earthquake precursors: comparison of independent ultralow-frequency electromagnetic (ULFEM) systems, Abstract NH31B-3863 presented at 2014 Fall Meeting, AGU, San Francisco, Calif., 15-19 Dec.

Dunson, J. C., Bleier, T. E., Roth, S., Heraud, J., Alvarez, C. H. & Lira, A., 2011, The pulse azimuth effect as seen in induction coil magnetometers located in California and Peru 2007--2010, and its possible association with earthquakes, Natural Hazards & Earth System Sciences, 11, 2085-2105.

Kappler, K.N., McPhee, D.K., Glen, J.M., and Klemperer, S.L., 2013, ULFEM time-series-analysis package: U.S. Geological Survey Open-File Report 2013-1285, 326 p. (http://dx.doi.org/10.3133/ofr20131285)

43 ShakeAlert: A Unified Earthquake Early Warning System for the West Coast

Margaret Hellweg, Richard Allen, Egill Hauksson (Caltech), Thomas Heaton (Caltech), John Vidale (UW), Paul Bodin (UW), Jennifer Strauss, and the ShakeAlert Team

Introduction

Earthquake Early Warning (EEW) is a method of rapidly identifying an earthquake in progress and transmitting alerts to nearby population centers before damaging ground shaking arrives. The first few seconds of the initial P-wave arrivals at one or more stations are used to detect the event, predict magnitude and peak shaking intensities. Detections from several stations are combined to locate the event. A warning of imminent shaking can be used to activate automatic safety measures, such as slowing trains, isolating sensitive equipment, or opening elevator doors. Warnings can also be sent directly to the public via cell phone, computer, television, or radio.

With support from the United States Geological Survey (USGS), the Gordon and Betty Moore Foundation, the California Integrated Seismic Network (CISN) and the Pacific Northwest Seismic Network (PNSN), we now move into Phase III of the ShakeAlert project. This transitions the focus from creating an end-to-end demonstration system for real time EEW in just California, to the development of a production prototype for a West Coast EEW alert. This collaborative effort involves the Berkeley Seismological Laboratory (BSL), the California Institute of Technology (Caltech), the University of Washington, and the Swiss Institute of Technology Zürich (ETH). Phase III of the Shake Alert development will be a blueprint for future public alerts.

Project Status

The ShakeAlert system combines the best aspects of the three methods from the proof-of-concept project; Caltech's OnSite algorithm, BSL's ElarmS algorithm and ETH's Virtual Seismologist.

Caltech's OnSite algorithm uses P-wave data from the single station nearest to the epicenter to provide rapid estimates of likely ground shaking. The BSL's ElarmS algorithm and ETH's Virtual Seismologist uses data from several stations around an event epicenter to produce a sometimes slower but more reliable estimate of magnitude and location. Occasionally, the ElarmS will be the first to send out an alert, due to constant improvements to the algorithm made possible by the regular monitoring of Ivan Henson's system performance tools.

The combination of these methods produces an algorithm, which has the speed of a single-station method, but is augmented by the confirmation and updated adjustments as additional station data becomes available.

When an identified event exceeds a defined combination of magnitude, ground shaking intensity, and statistical likelihood, information is broadcast to system users. Currently, during this demonstration phase, only project participants and beta users receive event information. Recipients include the state's emergency operations center at the California Office of Emergency Services (CalOES), Bay Area Rapid Transit (BART), Google Inc., PG&E, several Bay Area cities and counties, and many others. A schematic diagram of the end-to-end system can be found at: http://www.cisn.org/eew/EEWProject.html.

CEEWS

UC Berkeley and ShakeAlert partners are collaborating with CalOES to fulfill the recent California legislation that calls for the development of a state-wide EEW system called CEEWS. BSL researchers and staff (Peggy Hellweg, Doug Neuhauser, and Jennifer Strauss) stood on several of the committees this past year — including standards, models, and education and training committees — and provided findings and recommendations toward the best practices for such a system Many of the committees have met on a semi-monthly basis via phone in an effort to quickly come to a consensus between all stakeholders in this public and private partnership.

Initially, findings and recommendations were set to be approved by February 2015 and used as a basis for an implementation plan for the project as it moves forward. Stakeholders met in Sacramento in February 2015 however, a conseus to commit towards an implementation strategy was not reached. CalOES would like to revisit a few aspects including funding, as the state general funds is not allowed to be used to support the effort. Currently, CalOES is speaking with various stakeholders and analyzing various other funding strategies and paths. The deadline for fundings to be finalized is January 2016. We are hopeful that significant progress on this state-wide effort is on the near horizon. The process, however, is for the moment on hold.

Production Prototype

CEEWS process may currently be on hold, but the West Coast ShakeAlert system is continuing to take major steps forward. ShakeAlert is now transitioning from the current development system into a full-fledged production prototype (see Figure 2.43.1). Doug Neuhauser has been instrumental in the development of the overall system architecture. This includes the establishment of standard hardware platform requirements, standard operating systems, common libraries and other directory structures. Stephen Thompson attended 'Puppet school' with other ShakeAlert developers, in order to learn about the Puppet configuration management solution that the production system intends to implement.

A standard operating environment was defined (Linux) and six new computers were installed (NC, BK, CI) to create the production system. Current beta testers will be ported over to this system upon completion, thus freeing up the current demonstrational system for further algorithm development. Maintaining system architecture, common libraries, and operating environments ensures system reliability and robustness. Installation of redundant processing threads within and among Advanced National Seismic System (ANSS) regions will also serve to limit single points of failure. Going one step further, the production system group is also establishing a protocol for the synchroniza-

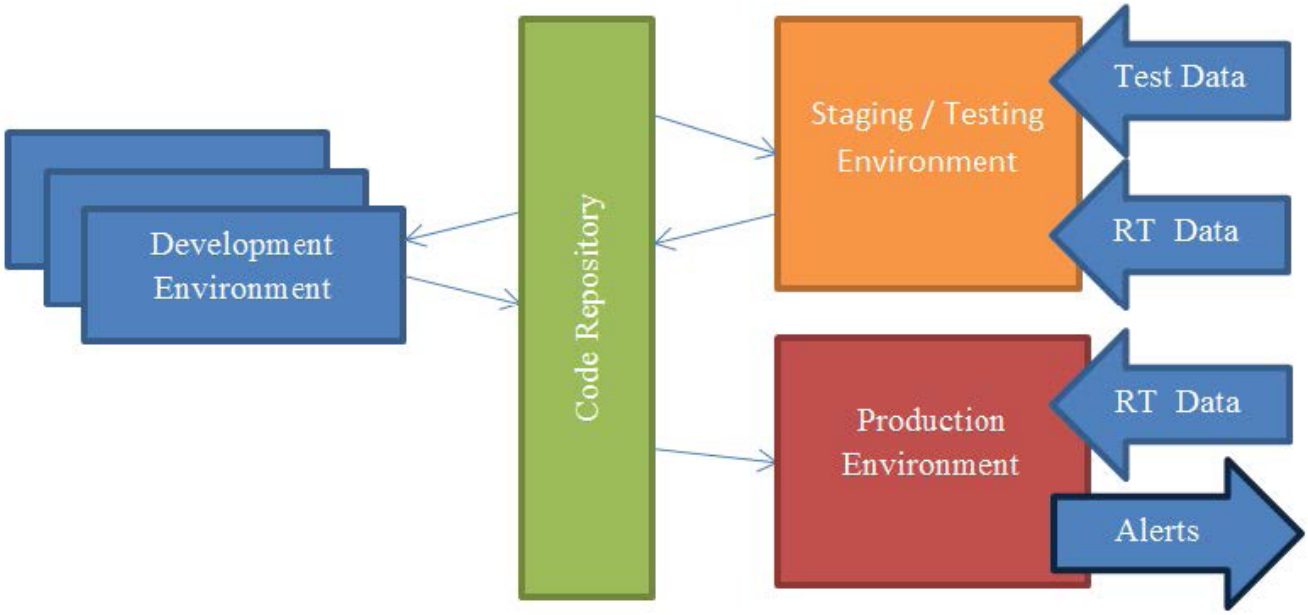

Figure 2.43.1. Schematic diagram showing the interaction between development, staging, and production computer environments. All code and configurations reside in a code management repository. All new and changed code and configurations are tested with real-time data streams and play-back of synthetic streams.

tion of multiple decision module servers to coordinate and thus, eliminate single points of failure; while at the same time maintaining consistent warning messages for users. System Testing & Certification Testing processes are also being defined and test data being gathered.

Perspectives

This year we will be continuing Phase III of the EEW project in collaboration with our partners at Caltech and U Washington, with funding from the USGS and the Gordon and Betty Moore Foundation. We look forward to continuing to maintain, operate, and improve the system as it transitions from a demonstration product to a working prototype. Phase III will highlight the increased importance of the EEW users and their interactions with the system.

Acknowledgements

This project is supported at UC Berkeley by USGS Cooperative Agreement G09AC00259, at Caltech by Agreement G09AC00258, at USC/SCEC by Agreement G09AC00255, and at ETH Zürich by Agreement G09AC00256. Funding from the Gordon and Betty Moore Foundation is under project number GALA 3024.

References

Given, D.D., Cochran, E.S., Heaton, T., Hauksson, E., Allen, R., Hellweg, P., Vidale, J., and Bodin, P., (2014). Technical implementation plan for the ShakeAlert production system—An Earthquake Early Warning system for the West Coast of the United States: *U.S. Geological Survey Open-File Report 2014–1097*, 25 p. http://dx.doi.org/10.3133/ofr20141097.

44 MyShake Prototype System

Qingkai Kong, Richard Allen, Louis Schreier, Young-Woo Kwon

Introduction

We built an end-to-end seismic system – MyShake – that harnesses personal smartphones sensors to collect data for analyzing and detecting earthquakes. The system has an android application running at the users' end, that monitors shakings. A backend server is used to both manage the phones and also to store data that is uploaded from the phones. We then rolled out the first version of the application to a group of volunteers and collected human activity data for 4 months, which is used to train a new ANN (Artificial Neural Network) algorithm, enabling the distinguishing of earthquakes from everyday human activities. We are also implementing a network detection algorithm that is running on our server to detect and locate earthquakes based on triggers uploaded by multiple phones.

MyShake Prototype System

The first version of MyShake was rolled out to ~75 phones in November 2014 (Figure 2.44.1), most of the time, we have approximately half of the phones running our application.

MyShake is mainly used to collect accelerometer data from daily activities. It first requires that the phone remains stationary for 30 minutes. Then a simple STA/LTA algorithm (*Allen*, 1978) is ran to detect any movements. When a trigger is detected, the trigger information, including the location and time of the trigger, is immediately sent to our back-end servers. A total of five minutes of data is stored locally on the phone, one minute before the trigger event and four minutes after. Waveform data is only uploaded when the phone is plugged into a power supply and is connected to a wifi network. This is to minimize power and data-plan usage. MyShake also uploads state-of-health (SOH) information every 2 hours and is able to receive updates and triggers from our back-end servers.

Our back-end server does not only function as a repository to store uploaded data, but also as a management tool. All parameters of MyShake on the phone (e.g. triggering algorithm configurations) can be modified remotely from our back-end servers. It can also provide basic information of active phones' spatial distribution on a map and record triggers.

Using this first version of MyShake, we collected four months of human activity data from volunteers for further analysis (Figure 2.44.2). During this period, 17600 triggers (all due to human activities) are uploaded to our server.

New ANN design

We have re-designed our algorithm based on the new data that we have acquired, including:

1. Human activities data collected from the first version of MyShake
2. Shake table tests data
3. Seismic data from traditional seismic networks in Japan, modified to reproduce smartphone-quality records

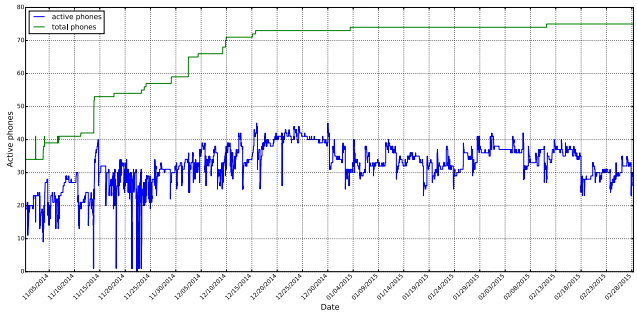

Figure 2.44.1: Number of phones that downloaded MyShake and are registered with our network (green curve), and the number of active phones running MyShake (blue curve). Server restarts are why the number of active phones dropped to zero during the first month.

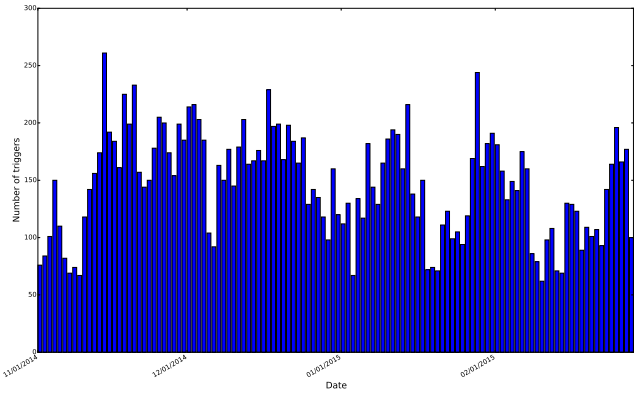

Figure 2.44.2: Number of phone triggers with waveforms uploaded to the server, a total of 17600 triggers.

A brief summary of our re-design process is outlined below:

1. Calculate all features in a 2 s sliding window,
2. Cluster human activities data so that we have a balanced number of earthquake cases and human activities cases,
3. Feature selection (*Kuhn et al.,* 2013),
4. Re-train the ANN algorithm with newly acquired data,
5. Test the performance of the ANN detector on new data (ones not used in the re-training).

We tested a total of 18 characteristics, identifying the 3 best features: one related to the amplitude, and the other two are measures of frequency and energy. Results of the new ANN algorithm is shown in Table 2.44.1.

Network Detection

The ANN algorithm described above will run on individual phones to check for movements due to earthquakes. When an earthquake is detected, two types of data is sent to our back-end servers, as is mentioned in previous sections; 1) the trigger time and the location, and 2) the three-components waveform data from the minute before the trigger event and four minutes after. As trigger information is easier to upload rapidly, it is what we use for real-time processing.

a)

Earthquake	Within 10 km	Within 20 km	Within 30 km
M7 1989 Loma Prieta	100% (2/2)	100% (4/4)	100% (11/11)
M6.7 1994 Northridge	100% (4/4)	100% (19/19)	100% (29/29)
M6 2004 Parkfield	95% (19/20)	90% (35/39)	86% (36/42)
M6 2014 Napa	100% (2/2)	75% (6/8)	42% (10/24)
M5.1 2014 La Habra	100% (13/13)	42% (22/52)	25% (30/120)

b)

Date	Non-earthquake	Earthquake
2015/02/01-2015/02/28	93% (3562/3823)	7% (261/3823)

Table 2.44.1: a) Performance of ANN when tested with earthquake data within various distances from epicenter. Percentage of records that are correctly classified as earthquakes is shown, along with the number of records samples in parentheses. b) Performance of ANN when tested with earthquake and non-earthquake (human activities) data. Percentage correctly identified as non-earthquakes and falsely identified as earthquakes is shown.

As the ANN algorithm can give false alerts (7% based on the test data shown in Table 2.44.1), we need a network detection algorithm that would be able to confirm the earthquake and determine the location and origin time of the earthquake. Our first-generation network detector is based on earthquake early warning methodologies (*Kuyuk et al.*, 2014). It requires a greater than 60 % of operating phones to be triggered within a 10 km radius in order for an event to be declared. The origin time of the event is assumed to be that of the first phone triggered. Triggers from phones located beyond the 10 km radius must fall within a defined space-time region (Figure 2.44.3) in order for it to be associated with the event. Table 2.44.2 shows our tests of the algorithm on two CA earthquakes.

Conclusions

We show here our end-to-end smartphone seismic detection system. The roll-out of MyShake-type seismic networks in earthquake-prone regions could improve warning systems around the world. And thus enabling the timely evacuation of low-rise buildings, increase public awareness of earthquake hazards, which could lead to better preparedness, and also provide the critical data needed to study earthquake processes, and thus build for their consequences.

Earthquake	Alert time (s)	Location error (km)	Origin time error (s)
M5.0 2014 La Habra	5	3.76	2
M6.0 2004 Parkfield	4	1.55	2

Table 2.44.2: Simulated network detection performance for US earthquakes. We pick two CA earthquakes with the most available station data: M5.0 2014 La Habra earthquake and M6.0 2004 Parkfield earthquake. In these simulations, we assume zero latency due to processing and network transmission.

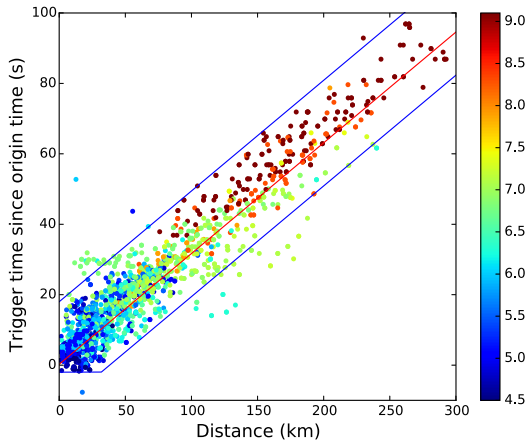

Figure 2.44.3: ANN trigger times versus epicentral distance from earthquake data from California and Japan. Regional network data is modified to simulate phone-quality data. Our classifier is applied to the data to determine when a trigger occurs. Red line is the line-of-best-fit and has a moveout velocity of 3.2 km s^{-1}. Most triggers are generated by S-waves. Blue outline is the time-space window used for the association of triggers with an event by the network detector.

Acknowledgements

This project is funded by Deutsche Telekom. We thank Deutsche Telekom for funding, providing smartphones and technical support. We thank SenseOS for providing us the first server support. We also thank Pacific Earthquake Engineering Research Center (PEER) for providing us shake table tests.

References

Allen R., (1978), Automatic earthquake recognition and timing from single traces, *Bulletin of the Seismological Society of America*, v. 68, p. 1521–1532.

Kuhn M., Kjell J., (2013), Applied Predictive Modeling, *Springer*, New York, NY, ISBN-13: 978-1461468486

Kuyuk, H.S., Allen R.M., (2014), Designing a Network-Based Earthquake Early Warning Algorithm for California: ElarmS-2, *Bulletin of the Seismological Society of America*, 104, 162-173, doi: 10.1785/0120130146.

45 TremorScope: Imaging the Deep Workings of the San Andreas Fault

Roland Bürgmann, Richard Allen, Douglas Dreger, Robert Nadeau, Barbara Romanowicz, Taka'aki Taira, Margaret Hellweg

Introduction

Until recently, active fault zones were thought to deform via seismic slip during earthquakes in the upper, brittle portion of the crust, and by steady, aseismic shear below. However, since 2000, this view has been shaken by seismological observations of seismic tremor deep in the roots of active fault zones. First recognized on subduction zones in Japan and the Pacific Northwest, tremor has also been found to be very active on the section of the San Andreas to the southeast of one of the most densely monitored fault segments in the world, near Parkfield (*Nadeau and Dolenc*, 2005). This deep (~20 - 30 km) zone of activity is located right below the nucleation zone of the great 1857 Fort Tejon earthquake. Thus, learning more about the temporally and spatially complex faulting processes in this zone may help us better understand the conditions that lead to such large ruptures.

The Project Plan and Implementation

The tremor source region is southeast of existing seismic networks around Parkfield, along the San Andreas Fault. We are adding eight seismic stations, the TremorScope (TS) network, in this area to complement existing instrumentation. Since the landowner at one planned station had leased acreage near our site for oil exploration, we sought an alternative and found a site near the San Andreas Fault, near the intersection of Bitterwater Road and Bitterwater Valley Road (Figure 2.45.1). Drilling at all four sites, TRAM, TRAY, TCAS and TSCS was completed in early April 2014.

TSCS is 750 ft deep and from a depth of 350 ft onward, is in solid rock. The other three boreholes are 1000 ft deep and mostly in softer material. All exhibit very little drift. The boreholes are cased with Schedule 21 PVC, with an inner diameter of 6 ". We hope this proves to have less electrical noise than a steel casing would, as well as provides more protection from lightning strikes and lower resonances.

Since the completion of the boreholes, we have been attempting to install the borehole equipment. Huts have been installed over the boreholes to offer a mounting surface for solar panels which will power the stations, but also to provide protection for the equipment from the sun and cattle (Figure 2.45.2). The borehole sites will have an accelerometer installed at the surface in the hut to record large nearby earthquakes, such as the 1857 Fort Tejon earthquake.

During the first installation effort, we discovered that all the boreholes were blocked at much shallower depths than originally drilled. We have been working with the driller since then to remediate the boreholes so they can be used. So far, equipment has only been deployed at TCAS (Figure 2.45.2), where data is being recorded from the surface accelerometer and borehole geophones. We are working with the driller to complete remediation at the remaining boreholes and plan to install equipment at those sites in late Summer and early Fall 2015. TS data are used in real-time earthquake monitoring (see Operational Section 4.7), as well as for tremor studies (http://seismo.berkeley.edu/research/recent_tremor.html). Data from the four surface stations and TCAS are now being archived and analyzed. In addition to contributing to investigations of tremors, the TS stations also improve our ability to characterize seismicity in the region.

Perspectives

Data from the TremorScope project is improving earthquake monitoring in the region south of Parkfield. Insights from the project will also contribute to the understanding of tremor and slip in other regions of the world where such phenomena have been observed, but are not nearly as accessible. Should a great San Andreas earthquake occur during this experiment, the network will also provide unprecedented and exciting insights into the seismic rupture process.

Acknowledgements

This work is funded by grant 2754 from the Gordon and Betty Moore Foundation.

References

Nadeau, R., and D. Dolenc (2005), Nonvolcanic tremors deep beneath the San Andreas fault, *Science*, 307, 389, doi:10.1126/science.1107142.

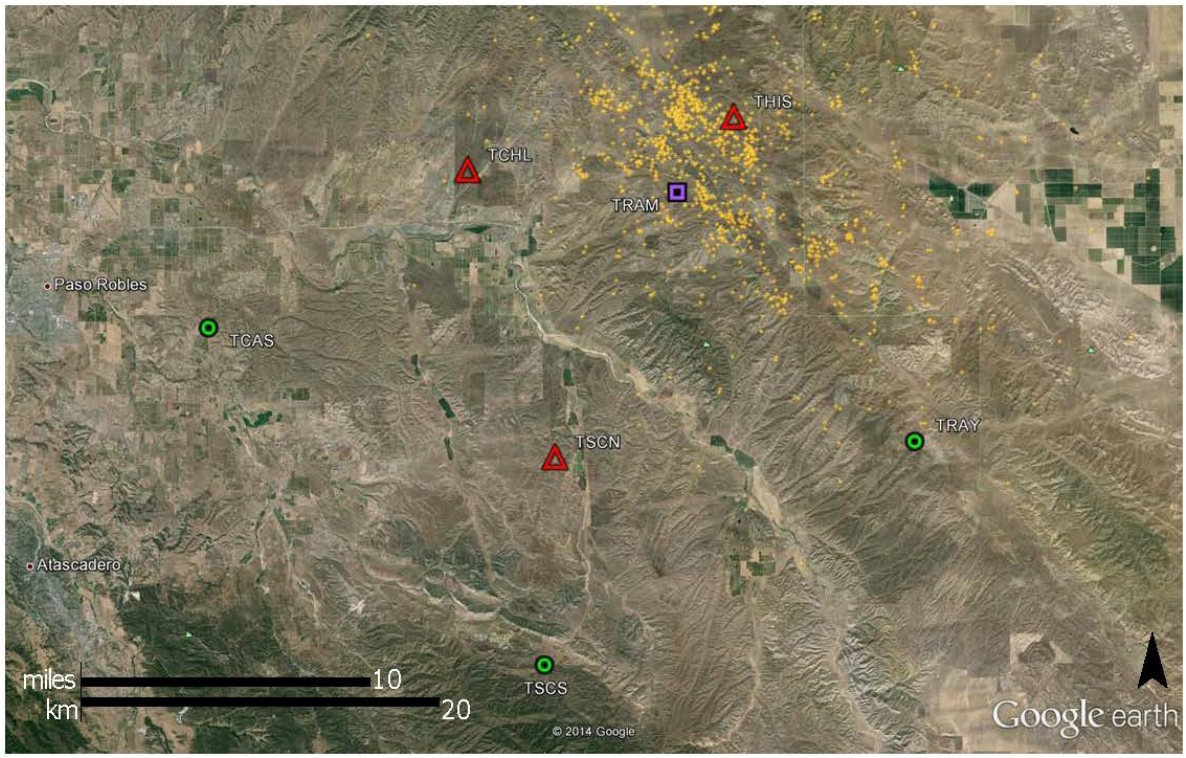

Figure 2.45.1: Google Earth image showing the locations of the TremorScope stations. Circles and triangles indicate borehole and surface sites, respectively. Suare marks TRAM, the site with both surface and borehole deployments.

Figure 2.45.2: Installing borehole sensors at TCAS